2019

Interfacial Behavior in Polymer Derived Ceramics and Salt Water Purification Via 2D MOS2

Hao Li
University of Central Florida

INTERFACIAL BEHAVIOR IN POLYMER DERIVED CERAMICS AND SALT WATER PURIFICATION VIA 2D MOS_2

by

HAO LI
B.Eng. Sichuan University, 2011
M.Sc. Loughborough University, 2012

A dissertation submitted in partial fulfillment of the requirements
for the degree of Doctor of Philosophy
in the Department of Materials Science and Engineering
in the College of Engineering and Computer Science
at the University of Central Florida
Orlando, Florida

Fall Term
2019

Major Professor: Linan An

ABSTRACT

In the present dissertation, the behavior of the internal potential barrier in a polymer-derived amorphous SiAlCN ceramic was studied by measuring its complex impedance spectra at various dc bias as well as different testing and annealing temperatures. The complex impedance spectra of the polymer-derived a-SiAlCN were measured under various dc bias voltages in a temperature range between 50 and 150 °C, as well as different annealing temperatures (1100-1400 ℃). All spectra, regardless of temperature and bias, consist of two semi-circular arcs, corresponding to the free-carbon phase and the interface, respectively. The impedance of the free-carbon phase is independent of the bias, while that of the interface decreased significantly with increasing dc bias. It is shown that the change of the interfacial capacitance with the bias can be explained using the double Schottky barrier model. The charge-carrier concentration and potential barrier height were estimated by comparing the experimental data and the model. The results revealed that increasing testing temperature led to an increased charge-carrier concentration and a reduced barrier height, both following Arrhenius dependence, whereas the increase in annealing temperature resulted in increased charge-carrier concentration and barrier height. The phenomena were explained in terms of the unique bi-phasic microstructures of the material. The research findings reveal valuable microstructural information of temperature-dependent properties of polymer derived ceramics, and should contribute towards more precise understanding and control of the electrical as well as dielectric properties of polymer derived ceramics.

Furthermore, the desalination performances and underlying mechanisms of two-dimensional CVD-grown MoS_2 layers membranes have been experimentally assessed. Based on a successful large-area few-layer 2D materials growth, transfer and integration method, the 2D

MoS_2 layers membranes showed preserved chemical and microstructural integrity after integration. The few-layer 2D MoS_2 layers demonstrated superior desalination capability towards various types of seawater salt solutions approaching theoretically-predicted values. Such performances are attributed to the dimensional and geometrical effect, as well as the electrostatic interaction of the inherently-present CVD-induced atomic vacancies for governing both water permeation and ionic sieving at the solution/2D-layer interfaces.

ACKNOWLEDGMENTS

This dissertation would not have been possible without the professional and insightful guidance of my advisors Prof. Linan An and Prof. YeonWoong Jung. Their kind and patient support throughout my entire graduate career is gratefully appreciated. I would also like to dedicate special thanks to my committee members: Professors Lei Zhai, Xiaofeng Feng and Xiaoming Yu, for their in-depth input, efforts, advice and service.

I would also like to take this opportunity to give candid thanks to the many collaborators, colleagues, staff members and friends during my studies at UCF, including: Dr. Raj Vaidyanathan, Dr. Kevin Coffey, Dr. Dan Zhou, Dr. Mikhael Soliman, Dr. Kurt Lin, Dr. Yu Bai, Dr. Laurene Tetard, Mr. Renan Gongora, Dr. Ran Zhao, Mr. Kirk Scammon, Mr. Ernie Gemeinhart, Ms. Pamela Ross, Ms. Sandy Griggs, Ms. Joy Kittredge, and Mr. Yandong Li, all for their kind helps, advice, friendship and sincere support. Special thanks also go to Dr. Tae-Jun Ko and Dr. Baisheng Ma, for their kind and professional help and collaborations during our research endeavours. The advanced materials analysis and characterisation facilities at the NanoScience Technology Center, Materials Characterization Facility, and Advanced Materials Processing and Analysis Center are also acknowledged along with the professional research support staff members.

This dissertation is also dedicated to my parents and extended family members in China, for their sincere love, care, and support throughout my life. They have my deepest appreciations for all the time. I would also like to gratefully acknowledge the loving help and support of my fellow church members throughout my years in Florida.

This dissertation is especially dedicated to my beloved wife Dr. Yi Ding, for her constant encouragement, sincere support and love. She has been of invaluable help and inspiration throughout my research, studies and life in North America every single day. I am perpetually and immensely indebted to her and her companionship, and she truly has my very sincerest and wholehearted appreciations and thankfulness at every moment for ever and ever.

All in all, I give thanks to the Lord my God, for His Providence, salvation and loving care. I am in no way deserve any of it. Thanks be to God, for His indescribable gift. Glory to be God in the Highest. Gloria in Excelsis Deo.

TABLE OF CONTENTS

LIST OF FIGURES

LIST OF TABLES

LIST OF ABBREVIATIONS

AC	Alternating Current
AFM	Atomic Force Microscopy
ASB	Aluminum Tri-Sec-Butoxide
CVD	Chemical Vapor Deposition
DC	Direct Current
MD	Molecular Dynamics
MEMS	Micro-Electro-Mechanical Systems
PDC	Polymer Derived Ceramic
TEM	Transmission Electron Microscopy
XRD	X-Ray Diffraction

CHAPTER 1: INTRODUCTION

The roles of interfaces of nanomaterials have significant contributions towards the properties, performances and applications of various categories of materials, either conventional or novel. The interfacial characteristics could stem from the responses of the intrinsically-present intra-phase interfaces upon external stimuli (e.g., electric field and magnetic field), or they may also arise from the interactions between the surfaces of materials with outside matters (e.g., solutions, oxygen, and irradiation).

Polymer derived ceramics (PDCs) are a novel class of amorphous materials synthesized through the controlled thermal decomposition of polymeric precursors.[1] PDCs exhibit unique microstructural features and desirable electrical/thermal/mechanical properties with promising applications compared to conventional ceramic materials prepared via powder metallurgy route.[2] Prominent PDCs properties include: superior thermal stability, excellent oxidation/corrosion resistance and high temperature multi-functionalities. In addition, the direct polymer-to-ceramic processing route makes PDCs particularly feasible for fabricating ceramic (micro)-components with complex structures/shapes.[3]

Reliable and accurate real-time pressure/temperature monitoring under high temperature and harsh environments (e.g., gas turbines, nuclear reactors, and high-speed vehicles) has been on high demand for device damage prevention as well as structural performance improvement. Surviving under harsh environments (e.g., pressurized, oxidative, radiative and corrosive) demands materials that satisfy both structural stability and functionality/properties reliability, which most currently available materials fall far short of.

Recent research and development efforts have explored several types of materials for harsh-environments sensing applications. Most notably among them are semiconducting silicon and silicon carbide due to proven controllable electric properties and well-developed micro-fabrication capabilities. However, applications of Si-based sensors are significantly restricted to a very limited operational temperature range due to severe material degradation,[4] not to mention when the environment involves corrosive atmospheres as well.

In the first part of this dissertation, we studied the microstructure, properties and impedance behaviors of polymer-derived SiAlCN ceramics, with a special attention on the internal potential barrier characteristics of this nano-domained two-phase material.

In a further attempt of investigating the interface/surface interactions in nanomaterials, this dissertation has also studied the interfacial interactions between the surfaces/interiors of two-dimensional (2D) MoS_2 layers upon contact with seawater solutions, with an overall goal of the development of viable 2D layers-based desalination membranes. The availability of freshwater resources has decreased with increasing potable, agricultural, and industrial water demands around the globe for the past decades.[5] This global challenge, along with the adversely accelerating climate change, has been calling for immediate solutions for meeting the demands. Apart from the conservation of existing water resources, increasing the freshwater supply is deemed as a more sustainable and direct solution.[6] Since seawater is readily accessible and abundant, various thermal and physical desalination technologies have been utilised worldwide to produce drinking water by removing dissolved salts and other minerals from saline water. While multi-stage flash (MSF), multi-effect distillation (MED), and reverse osmosis (RO) are the most widely used desalination technologies, RO membrane is gaining market share at a faster pace.[7,8] RO is a high-pressure membrane process that utilizes a semi-permeable

polymeric membrane to retain salts and low-molecular-weight solutes while allowing the passage of water via diffusion. Despite the operational simplicity, RO membranes suffer from several technical limitations including low conversion efficiency, membrane fouling, and energy demand to pressurize the feedwater.[9,10] Accordingly, developing high-performance membrane materials with improved water recovery without compromising the solute rejection remains a compelling demand.

A potentially promising solution stands with engineering the structure of traditional materials into tailored porosity or exploring a new type of intrinsically porous nanomaterials-based membranes. Recently developed two-dimensional (2D) materials present unprecedented opportunities for water desalination and molecular sieving technologies owing to their structural uniqueness.[11-13] Their extremely small thickness (i.e., a few Å for 2D monolayers) projects superior water permeation rates benefiting from small diffusion lengths for molecular transports while their high mechanical flexibility renders advantages for membrane integrations. Moreover, 2D materials produced by chemical synthetic routes possess high-density "intrinsic" structural imperfections (e.g., near atomic vacancies) whose physical dimensions are comparable to those of salt ions and water molecules.[14] In this endeavor, a variety of 2D materials have been explored including graphene,[15-18] dichalcogenides,[19-22] and graphene oxides,[23-26] along with substantive efforts for the structural engineering of traditional membrane materials such as zeolites,[27-30] and metal-organic frameworks [31-34]. Amongst them, 2D molybdenum disulfide (MoS_2) layers have recently gained significant interests for a wide range of water and environmental technologies. They not only share the intrinsic structural advantages inherent to other 2D materials but also present additional suitability such as excellent chemical stability and non-toxicity.[35-37] Furthermore, a variety of structural variations such as point defects, grain boundaries, and van der Waals (vdW) gaps have been ubiquitously

observed in 2D MoS_2 layers grown via chemical vapor deposition (CVD) process.[38-40] Such "intrinsically" present structural imperfections of very high concentration (e.g., areal density of ~10^{13} cm^{-2} for sulfur vacancies[41]) offer 2D MoS_2 layers high promise as an efficient membrane material for water desalination applications. Despite the theoretically-projected promise of 2D MoS_2 layers, their experimental utilization for membrane-based desalination technologies has been rarely approached. A few experimental studies have explored MoS_2 laminar membranes of very large thickness (typically, ~1-10 μm) constituting mechanically stacked individual 2D flakes.[14] These laminar 2D MoS_2 membranes of large thickness have exhibited significantly limited desalination efficiencies, failing in meriting the structural uniqueness and performance advantages projected with near atom-thick membranes. Scarcity of experimental studies on the 2D MoS_2 layers-based membranes of near atomic thickness for water desalination is attributed to technical difficulties associated with integrating 2D layers preserving their structural integrity. Particularly, it has been challenging to produce large-scale (> cm^2) "continuous" 2D MoS_2 layers of ~1-10 nm thickness and their seamless integration onto porous substrates, hindering their applications to desalination technologies.

In the latter part of the dissertation, we investigate the experimental realization of high-efficiency water desalination enabled by ultra-thin 2D MoS_2 layers-based membranes. We demonstrate the integration of centimeter-scale CVD-grown 2D MoS_2 layers of only ~7 nm thickness onto porous polymeric substrates and studied their desalination performances. This new type of near atom thick-membranes exhibits an excellent combination of high water permeability approaching theoretically predicated values and superior ionic sieving performance for various seawater salts. Fundamental mechanisms responsible for the observed high desalination efficiency are also discussed, with a special focus on the roles of interfaces.

CHAPTER 2: LITERATURE REVIEW

2.1 Polymer-Derived Ceramics (PDCs)

2.1.1 Introduction to Polymer Derived Ceramics

Polymer derived ceramics (PDCs) are a novel class of amorphous materials synthesised through the controlled thermal decomposition of polymeric precursors.[1] As compared to the conventional polycrystalline ceramics, PDCs possess unique complex microstructures that comprised of a silicon-based amorphous matrix phase and a nano-domained "free-carbon" phase that contains graphitic sp^2 carbon. Silicon-based PDCs have been obtained via the pyrolysis of organo-silicon polymers as a direct synthesis route as early as the 1960s.[2] Pioneering work by Fritz and Raabe[42] and by Yajima *et al.*[43] on the synthesis of SiC ceramic fibers from thermolysis of polycarbosilanes made prominent scientific progress towards application potential of PDCs.

The PDCs processing route has drawn growing attention as an additive-free method which also yields materials with fine-tuned chemical composition as well as well-defined nano-structures.[44] The sophisticated microstructures of PDCs would experience significant transformations under very high temperatures with a characteristic persistence of the nano-domains, which gives rise to the exceptional resistance to crystallisation.[45] Characterisation techniques for investigating PDCs microstructures include NMR, XRD, SAXS, FTIR, and Raman spectroscopy, which give integral information, as well as TEM, SEM and EELS that provide information about local properties at the nano-scale. In addition to experimental studies, there have also been many theoretical investigations aiming to explain the transformations of nano-clustered carbons during thermal decomposition as well as the crystallisation behaviour of PDCs.[2]

The unique yet diverse electrical and thermo-mechanical properties of PDCs such as high-temperature semiconducting behaviour[46], anomalously high piezoresistivity[47], profound doping effects[48], as well as excellent resistance towards high-temperature decomposition and creep[49] have enabled PDCs to become promising candidates for potential applications in ceramic fibres[50], ceramic matrix composites[51], energy storage[52], porous components[53], and high-temperature micro-sensors[54].

Through the PDCs direct polymer-to-ceramic processing route, products such as ceramic fibres and layered composite materials have been made, which the conventional powder-based technology cannot feasibly yield due to the presence of additives. Traditional polymer-forming techniques such as polymer infiltration pyrolysis (PIP), injection molding, coating from solvent, extrusion, or resin transfer molding (RTM) can also be utilised to process pre-ceramic polymers, and the formed objects then undergo further conversions to ceramic components by appropriate heat-treatment. [2]

The processing procedures of PDCs comprised of the following fundamental steps (as shown in Figure 1 as a basic flow-chart):

(a). Chemical synthesis of starting ingredients which produces polymeric precursor;

(b). Cross-linking of polymeric precursor gives infusible pre-ceramic network;

(c). Pyrolysis of the pre-ceramic network under high temperature yields amorphous ceramics.

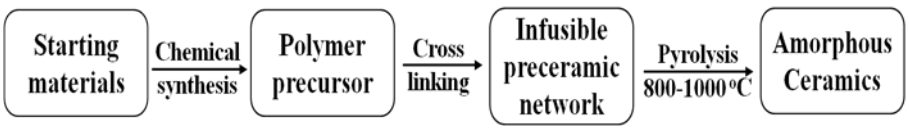

Figure 1 The processing procedure of PDCs.

2.1.2 Polymeric Precursors

As the starting materials for PDCs, pre-ceramic polymeric precursors have attracted extensive attentions, and many review articles [55-57] are dedicated to topics related to precursors synthesis. The importance of their key roles in heavily influencing the properties of PDCs stems from the fact that the chemical composition, the number of phases, the phase distribution and the microstructure of PDCs depend upon the molecular structures of polymeric precursors. Extensive research efforts have been devoted to the investigations of tailing various molecular structures to achieve optimum macroscopic chemical and physical properties of PDCs.[2]

Birot *et al.*[55] had proposed some key properties that effective polymeric precursors should possess in order to satisfy subsequent thermal decomposition processes:

(a). Sufficiently high molecular weight in order to avoid volatilisation of low molecular components;

(b). Suitable rheological properties (viscoelasticity) and solubility for the shaping process;

(c). Latent reactivity (presence of functional groups) in order to gain thermosetting or curing properties;

(d). Polymeric structures with cages or rings to reduce the volatilisation of the fragments due to backbone cleavage;

(e). Low level of organic groups which lead to increased ceramic yield and decrease undesired/excessive "free-carbon" contents.

Since its inception, silicon-based polymeric precursors for PDCs have long drawn wide attention. Suitable organo-silicon PDCs precursors have a generalised molecular structure as illustrated in Figure 2. Design and tailoring of the polymeric precursors on a molecular level

mainly focuses on two aspects: a). the (X) group on the backbone, and b). the substituents groups attached to Si (i.e., R^1 and R^2). Different classes of the Si-based polymers contain different (X) group. Examples as shown in Figure 3 include: poly(organosilanes) with X=Si, poly(borosilanes) with X=B, poly(carbosilazanes) with X=C, and poly(organosilylcarbodiimides) with X=[N=C=N]. Functional side groups of R^1 and R^2 also play important roles in adjusting the solubility of the polymer, the electronic, optical, and rheological properties as well as the chemical and thermal stability of PDCs. Furthermore, the R^x groups determine the carbon content in the final PDCs products. [2]

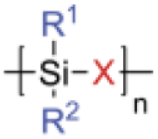

Figure 2 Generalized representation of the molecular structure of pre-ceramic organo-silicon PDCs precursors.[2]

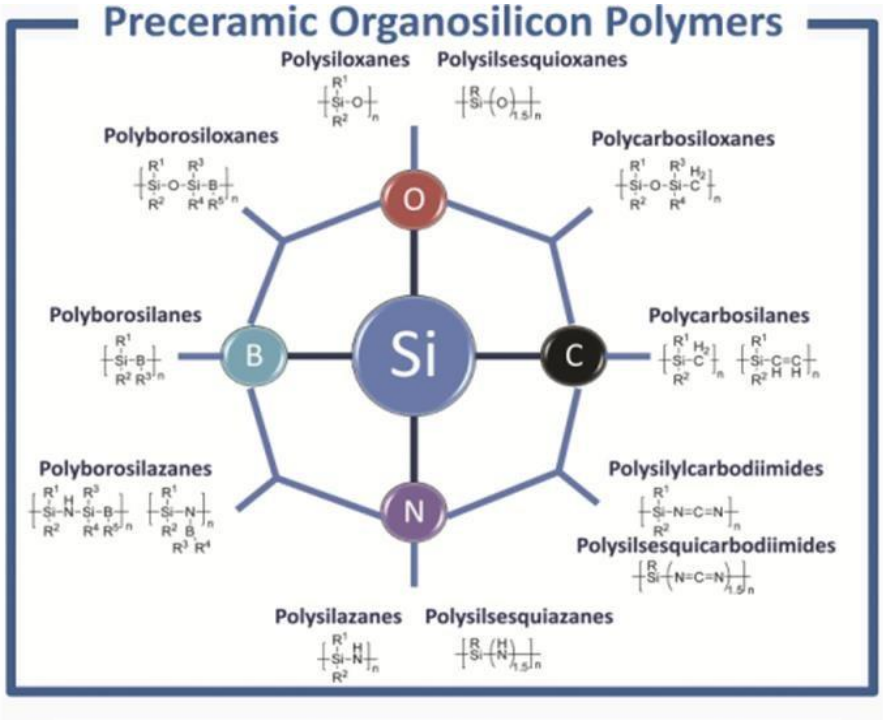

Figure 3 Main types of Si-based polymer precursors for PDCs.[2]

Besides from the above-illustrated Si-B, Si-C, Si-N and Si-O based polymer backbones, another promising elemental candidate is aluminium, because Al-containing materials (e.g., AlN and Al_2O_3) show desired properties such as high strength and excellent resistance to thermal shock and oxidation.[58] Research has shown that polysilazane-derived ceramic with a Si/Al/O/N system has a suppressed grain growth.[59] High-strength alkali-resistant Si/Al/C/O-fibers have been produced from polyaluminocarbosilane.[60]

2.1.3 Processing of Pre-ceramic Polymers

2.1.3.1 Shaping

Since the PDCs precursors essentially remain polymeric materials during the shaping conditions/temperatures, extensive varieties of more cost-effective and industrial-friendly forming techniques can be applied than the traditional powder-/paste-based routes. Moreover,

this approach has important technological advantages in many aspects, for example: has no drying issues which has enabled bulk-fabrication; does not require long processing times for gelation and drying; no involvement of flammable solvents; can be processed in the molten state; avoids tool wear problems and brittle fracture upon finishing of the component.[2,61]

The shaping techniques as reported in literature have been diverse: some are unique (e.g., formation of nanostructures directly by pyrolysis)[62]; some explore polymer-processing routes (e.g., injection moulding)[63]; while many are applicable to ceramic materials in general (i.e., casting/solidification, deformation, machining/material removal, joining, and solid free-forming).[2,64]

2.1.3.2 Crosslinking

Since cross-linking is an essential part of the PDCs fabrication processes, a typical precursor falls into one the three categories: 1). a cross-linkable liquid; 2). a meltable and curable solid; 3). an unmeltable but soluble solid.[2] In addition, the shaped pre-ceramic polymers should be able to undergo a thermosetting transformation while keeping the shape unchanged during the subsequent polymer-to-ceramic conversion. Functional groups (e.g., the X group being –H or –OH) introduced to the pre-ceramic polymers can achieve a spontaneous thermosetting typically below 200 ℃. It is also possible to further lower the cross-linking temperature via catalysing agents, which can also reduce oligomers evapouration hence fewer bubbles and higher ceramic yield.[65,66] Successful laser curing has also been reported for rapid prototyping processes in fabricating complex-shaped components.[67]

Various other curing methods may also be applied after-shaping. One commonly used method is oxidative curing, which would of course introduces undesired high level of oxide, thus results in ceramics with a lowered high-temperature stability.[68,69] Another means involve γ-radiation

or e-beam curing which can yield virtually oxygen-free ceramics, however the limited penetration depth means they are mostly suitable for producing fibres.[70] Incorporation of photosensitive functional groups onto the backbone of pre-ceramic polymers can produce UV-curable precursors, which has found desirable applications in fabricating MEMS and fibres.[71-74]

The demands of bulk / batched productions of PDC has brought forth the introduction of various types of fillers to be incorporated with pre-ceramic polymers. Fillers serving different purposes have been employed, examples include: polymers, metals, ceramics in various formats (e.g., powders, platelets, nanotubes, and nanofibres).[2] Effects of fillers vary in broad ranges depending on the desired production outcomes. Inert fillers (e.g., SiC powders) help minimise the number of pore-sized defects; whereas functional fillers (e.g., $MoSi_2$ [75] and FeSi [76]) have been used as electrical conductivity and magnetic functionality modifiers. Of the previously mentioned examples of fillers, metallic ones mainly contribute as to react away the gaseous byproducts during heat-treatment processes [77]; in contrast though, the polymeric fillers aim to produce micro-pores of desired sizes [78].

2.1.3.3 Conversion from polymer precursor to ceramics

After obtaining shaped and cross-linked precursors, the final step towards PDCs products is polymer-to-ceramic transformation. Typical thermal decomposition (at approximately 1000 ℃) of basic organo-silicon polymers $–[SiR^1R^2–X]_n–$ leads to amorphous SiC, $Si_xC_yO_z$, and $Si_xC_yN_z$ PDCs (as illustrated in Figure 4). The polymer-to-ceramic conversion process results in the decomposition or elimination of methyl, phenyl, vinyl groups as well as Si–H, Si–OH, or Si–NH_x groups. There have been many conversion methods applied, both thermal and non-thermal,[2] yet amongst them, oven pyrolysis still remains the most extensively used coupled

with flowing inert gas continuously removing undesired decomposition residuals.[79] One of the most routinely used conventional technique is thermal decompositions at relatively medium temperatures, followed by annealing stages at even higher temperatures. Another route explored is via photolithography, during which liquid phased mixture of pre-polymeric materials are exposed under ultra violet irradiations for a relative brief period of time. At this stage, the crosslinking processes are initiated and carried to complete, yielding pre-ceramics in solid phase with fewer residues. The resultant product then would undergo similar pyrolysis as well as annealing processes as mentioned above. The latter approach (the UV route) normally would result in fully-dense PDCs samples and shorter products turn-around times.

Various other newly-developed / implemented techniques have also been utilised to yield PDC components of complex shapes. One prominent example is 3-dimentional printing which have found applications in producing microfluidic channels via lithography [80] as well as parts with ordered porosity based on a powdered route [81]. Another promising technique for micro / nano-fabrication of PDCs is focused ion beam (FIB) for micro electro mechanical systems (MEMS) applications as demonstrated by Tian *et al.*, which have been shown to yield PDCs products of more precise shape controls while retaining the superior properties of PDCs.[82] Additive manufacturing techniques, with the help of 3-D printing and stereolithography, have also been explored to develop ceramics with greater geometrical flexibility while improving material strength and density which hold promise for potential applications in wider fields such as protective thermal shields and electronic device packaging.[83]

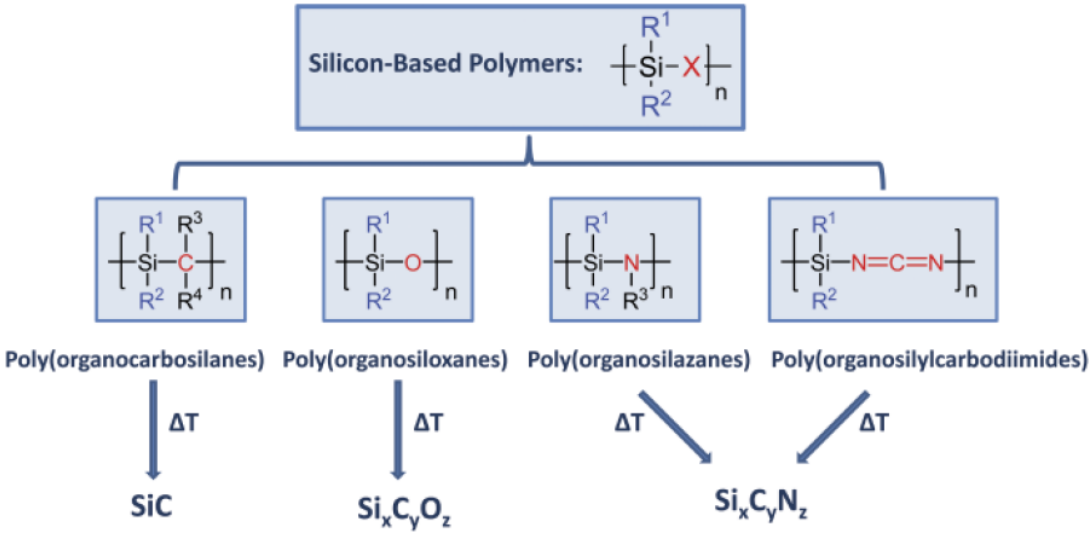

Figure 4 Typical thermal decomposition of basic organo-silicon polymers.[2]

Among the other polymer-to-ceramic conversion methods, chemical vapour deposition[84] and plasma spraying[85] have been used to produce ceramic coatings with the pre-ceramic polymers deposited directly on different substrates. Ceramic coatings has also been prepared via laser pyrolysis, which has the capability for selective writing.[86] In terms of non-thermal process, ion irradiation has been used to produce nanowires[87] as well as luminescent ceramic coatings/layers with high hardness.[88-90]

2.1.4 Microstructure of PDCs

PDCs possess sophisticated microstructures and would experience significant transformations under very high temperatures (>1000 ℃) with a characteristic persistence of the nano-domains, which gives rise to the exceptional resistance to crystallisation.[45] At elevated temperatures, local crystallisation initiates in the amorphous bulk, followed by chemical bonding re-distribution leading to phase separation, and finally results in nucleation and growth of nano-crystals. It has been reported that SiCN contains nano-domains of approximately 1–3 nm in

size,[91-93] with the type, composition and shape of nano-domains identified via small-angle X-ray and neutron scattering (SAXS).[94] A schematic illustration of the possible microstructure of Si-C-N based PDCs is given in Figure 5.

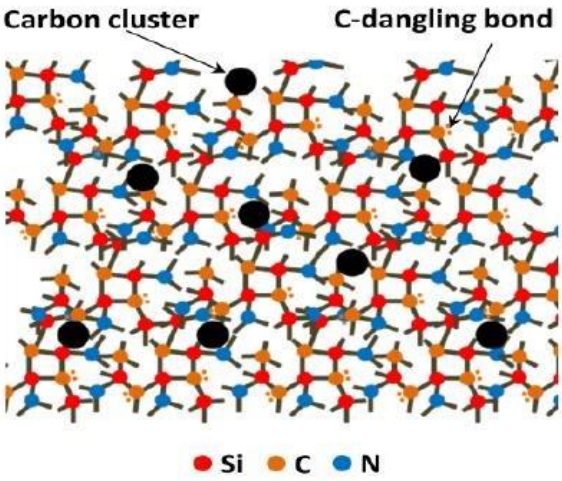

Figure 5 Schematic illustration of the possible microstructure of Si-C-N based PDCs.

For the amorphous-to-partially-crystalline transformation process, PDCs materials typically experience the following three main phases of microstructural changes: a). phase separation in the bulk of the material during annealing; b). graphitization process gives rise of the "free carbon" phase with the presence of carbon-dangling bonds; c). localised nano-crystals emerge under elevated temperatures.[2]

Characterisation techniques for investigating PDCs microstructures include NMR, XRD, SAXS, FTIR, and Raman spectroscopy which give integral information, as well as TEM, SEM and EELS that provide information about local properties at the nano-scale.[2] Various and extensive experimental characterisation efforts have been devoted to study the microstructure or microstructural evolutions of PDCs. Raman spectroscopy reveal that beside the possible presence of "free carbon", graphene sheets of relatively long-range order could exit. Raman

spectra also act as a powerful technique to conduct quantitative investigations on the evolutionary history / concentration changes of these "free carbons", which would significantly influence the electrical conduction mechanism (i.e., amorphous semiconducting behaviour for PDCs with low free carbon concentrations, whereas high free carbon concentrations yield a tunneling percolation mechanism[95]).[96]

Free carbons are generally present in many PDC systems. Depending on temperatures, their distributions are different. At elevated temperatures (e.g., > 1000 ℃), carbon takes the form of locally enriched regions of turbostratic graphite, whereas at lower temperatures, they normally show a homogeneous dispersion within the amorphous matrix. Although not thoroughly understood about the nature of free carbons, several reports have attributed PDCs oxidation / corrosion / crystallisation resistance to the presence of and its distribution characteristics of them. Transmission electron microscopy (TEM) have been extensively used to study the nature of the free carbons, which confirmed the presence of nano-sized carbons in turbostratic / graphitic forms.[2] TEM results also revealed how that the concentration of polymeric precursors as well as annealing histories could affect the ordering of carbons clusters. [97] Investigative efforts have devoted on the nano-domain-like distributions of Si-based carbon and carbon-rich clusters. One of the most valuable tools is small-angle X-ray scattering (SAXS), which proved the presence of short-range order. Together with the other auxiliary techniques such as Raman spectroscopy as well as X-ray diffraction (XRD), SAXS characterisations have confirmed to presence of nano-domains within polymer derived SiCN samples, with the increase in the nano-domain volume fraction lead to the increase in the inter-granular surface area thus the reactivity of the PDCs.[94] Experimental techniques, however, have limitations on the investigations of PDCs because of the amorphous nature of the materials. To compliment this, computational / theoretical modelling efforts have also emphasised on the microstructural changes in PDCs

systems. The microstructural evolutions of PDCs during processing / annealing as well as when under external influences (e.g., stress, temperature) can reveal both how to better tailor the properties of PDCs for targeted needs and how to understand the fundamental mechanisms of its characteristic behaviours (e.g., electronic, magnetic, optical, and chemical aspects).

As discussed above, the versatility of the potential applications of polymer derived ceramics stems from the possibility to tailor the backbone elements of the polymeric precursors (as well as a variety selections of fillers of many types), which ultimately comes from the less-sophisticated chemical synthesis processes.

Most commonly studied PDC categories are ternary ceramics as well as quaternary ones (i.e., polymeric backbones containing three or four types of main elements). Of all these PDCs, those derived from silicon (Si) containing polymeric precursors are the most promising and are the most extensively investigated.

Besides the foundational Si atom on the polymeric backbone, molecular structural differences also would influence the properties of the final PDCs products. Stoichiometric factors dictate there would be three groups attached to the Si atom (other than the Si-Si bonds themselves). These three attached groups can be classified into two main categories: organic groups of R^1 and R^2 as well as a functional group of X (as show below in Figure 6). The choice of different organic groups of R would mainly influence the rheology as well as solubility which would certainly affect the selection of processing techniques in subsequent steps.[98] In addition, the PDCs yield is also dependent on the amount of carbon atomic contents of the R organic groups, with higher yields correspond to increased carbons. Moreover, the functional X group is chiefly responsible for the microstructures of the resultant PDCs, where the presence of free carbons become a hindrance for diffusions thus lead to the increased resistance towards

crystallization.[99] A synergistic effect of the selection of the R and X group (as well as the Si/X ratios) will ultimately determine the properties of PDCs on the stability, electronic, and optical aspects. Mera *et. al*.[100] have reported nanoscale characterizations of PDC SiCN and SiCO in terms of microstructures and energetics. They found that the results are consistent with the nano-domained models as proposed by Saha *et al*.[101], which essentially comprised of a continuous yet inefficiently packed Si-based matrix phase, as well as entrapped within some carbon-rich clusters of varying degree of order. The illustrative depictions of Si-O-C as well as Si-C-N PDC systems are given in Figure 7 and Figure 8 respectively. The mixed bonds (Si-C and Si-O bonds) sandwiched between the Si-O-C and carbon-rich domains (as shown in Figure 7) are attributed to the high thermodynamic stability according to calorimetric results. Additionally, carbon contents in SiCN PDCs significantly affect the microstructure in terms of the nano-domain dimension and distributions. At lower carbon contents, polymer derived SiCN ceramics are constituted of Si_3N_4 and free carbon (mainly in sp^2) nano-domains (which are inherently amorphous), with the inter-domain regions consist of mixed bonds (Si-N and Si-C bonds) which is likely stabilised due to the H atoms. Whereas for higher carbon contents. SiCN PDCs witness free carbon nano-domains of larger sizes, which are semi-continuously inter-connected within the matrix (depicted below in Figure 8). One noteworthy feature of PDCs is that the annealing temperatures would cause further microstructural changes in terms of the loss H as well as lowered amount of mixed bonds (refer to Figure 9).

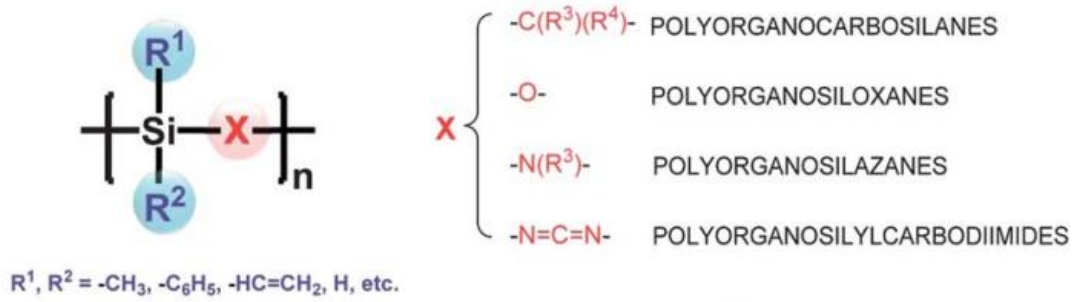

Figure 6 A generalized formula of Si-containing polymeric PDC precursors.[100]

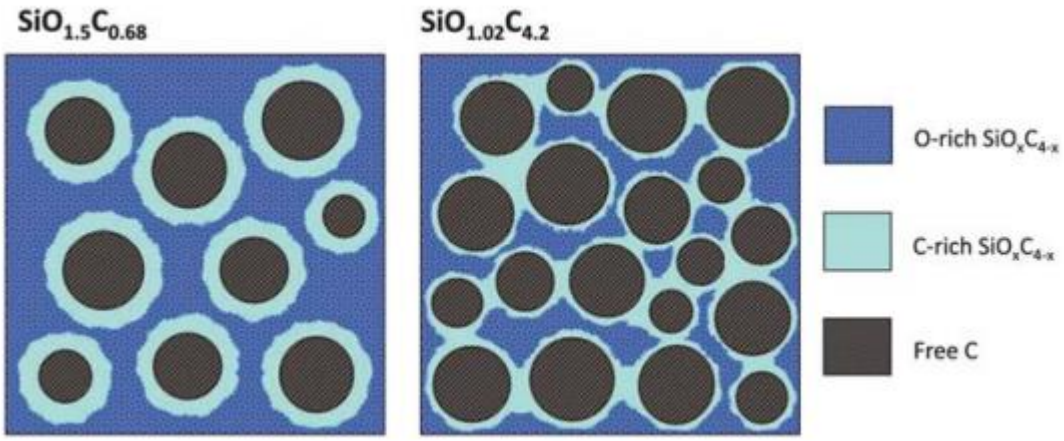

Figure 7 Nano-scale structural model of low carbon (left) and high carbon (right) containing SiOC ceramics at 1100 ℃.[100]

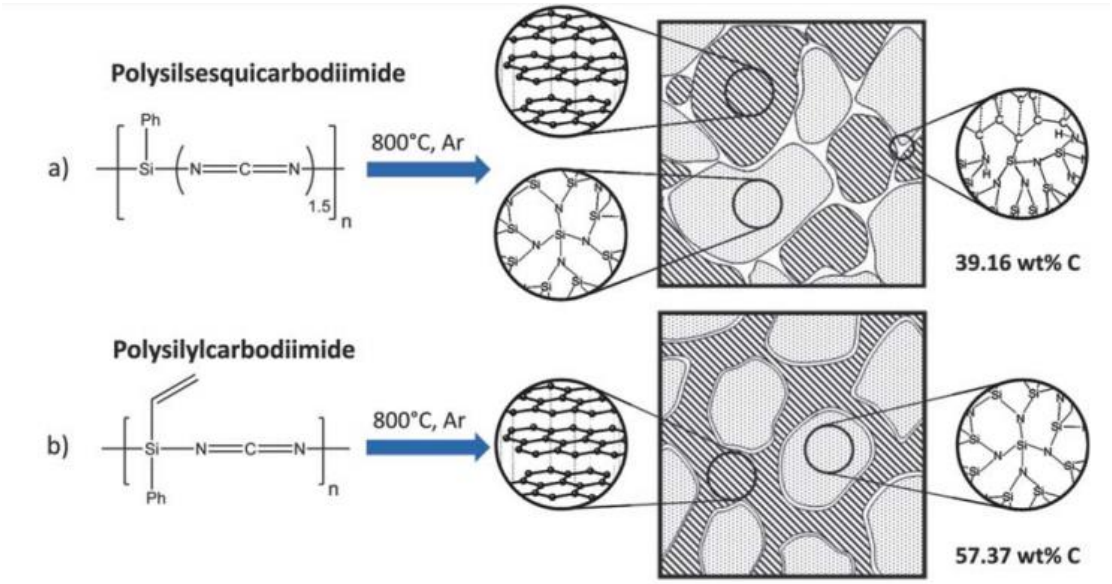

Figure 8 Carbon-rich precursor system comprised of Si_3N_4 clusters embedded within a continuous amorphous / turbostratic carbon matrix. [100]

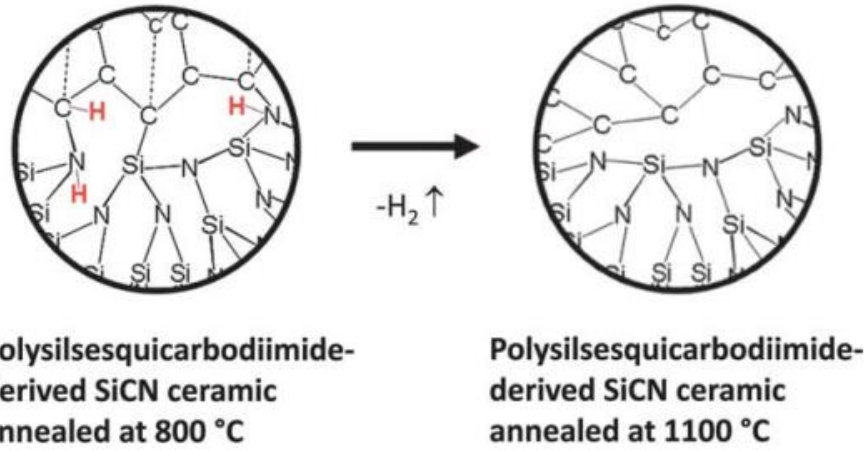

Figure 9 Mixed bonding in the interfacial region between Si_3N_4 and carbon nano-domains in a samples synthesized at 800 ℃ and (right) loss of hydrogen and of mixed bonding post 1100 ℃ pyrolysis.[100]

Microstructural changes in PDCs under external stress / strains have also been reported, both for SiOC [102] as well as SiCN [47]. Both teams observed piezoresistive effect for respective PDCs samples with the latter team ascribed this phenomenon to the unique self-assembled nano-

domain microstructures discussed above following a tunneling-percolation model. Whilst the former team studying polymer derived SiOC discovered similar mechanism due to percolation effects owing to the segregated (electrically conductive) carbon clusters within the Si-based matrix. Specifically in terms of the origin of piezoresistivity, a tunneling-percolation network within the Si-based matrix stem from the conducting graphene sheets, with the tunneling process (which PDCs resistivity is dependent of) become ultra-sensitive to the distance between the graphene sheets. Such model therefore connects the piezoresistivity to the distance changes between graphene sheets due to external pressure.

In addition to the influence of external pressure on microstructural changes in PDCs, temperature could also influence the microstructures of PDCs especially causing changes in free carbons thus further determine the electrical properties.[103] The pyrolysis temperatures could cause the ratio of sp^2/sp^3 carbon to increase thus lead to a rise in electrical conductivity owing to various mechanisms: a band-tail hopping conduction mechanism for SiAlCN [104], a caused by the conductivity increase in the carbon phase for SiBCN [105], as well as C-O bonds re-arrangement in the free carbon phase (for SiOCN) [106].

2.1.5 Properties of PDCs

2.1.5.1 Thermal Properties

Polymer-derived ceramics exhibit excellent thermal properties under high temperatures including: a). resistance to thermal decomposition and crystallisation up to 1800 ℃ (Figure 10 and Figure 11 respectively) [49]; b). good thermal shock resistance (Figure 12) [107]; and c). superior oxidation resistance and corrosion resistance.[108]

Riedel *et al.*[49] have reported a polymer-derived SiBCN ceramic that can withstand thermal degradation up to ~2000 ℃, much higher than that of SiCN and Si_3N_4. The composition of SiBCN annealed at 2000 ℃ almost remains the same as the as-synthesised specimen, indicating its excellent high-temperature stability.

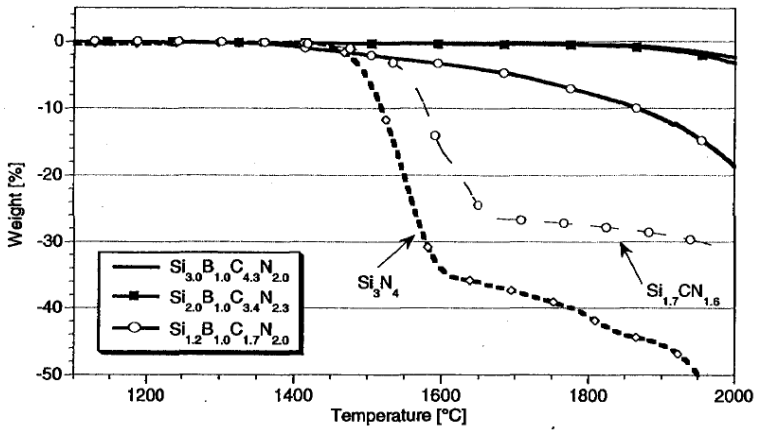

Figure 10 Thermal gravimetric analysis of polymer-derived SiCN, SiBCN and commercially available Si3N4.[49]

As shown in Figure 11 of the XRD results, SiBCN remains amorphous up to 1700 ℃, and when annealing temperature reaches 2100 ℃, β-SiC is found as the only crystalline phase, showing excellent resistance to crystallisation.[49]

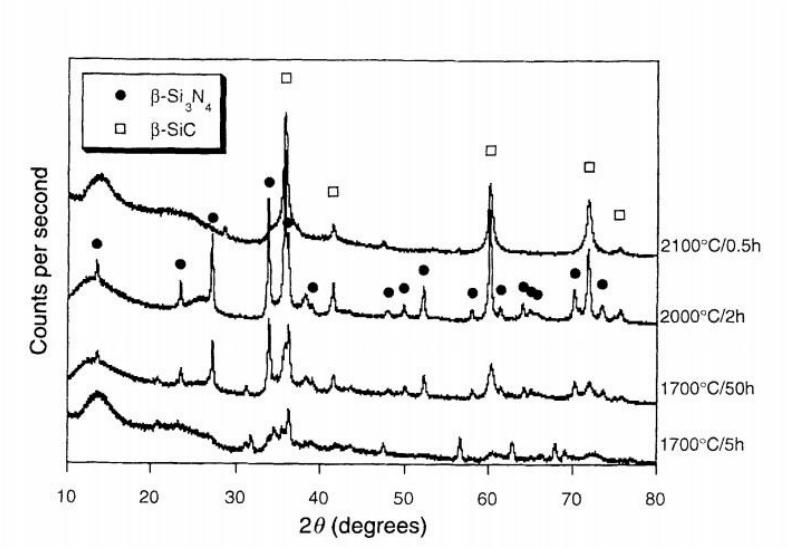

Figure 11 The XRD results of SiBCN annealed at different temperatures.[49]

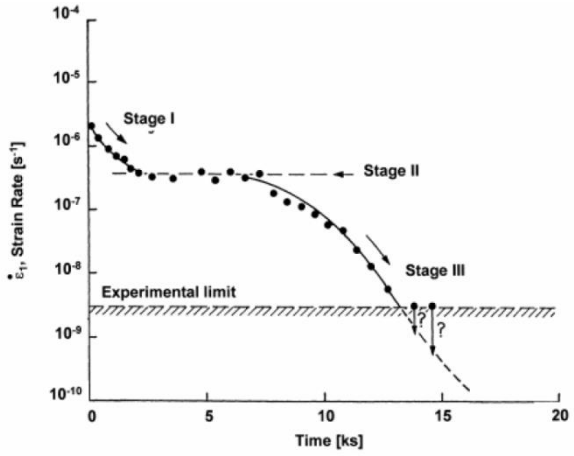

Figure 12 Typical creep observed in polymer-derived SiCN and SiBCN materials.[108]

Polymer-derived SiAlCN ceramics have been reported to exhibit superior oxidation and hot-corrosion resistance than that of SiCN (as shown in Figure 13).[109-111] Comparison of SiAlCN and SiCN surfaces underwent hot-corrosion in NaCl saturated solution shows virtually no cracks on SiAlCN (Figure 14). Due to the excellent oxidation/corrosion resistance of SiAlCN ceramics, they are promising candidates for high-temperature and harsh-environment applications.

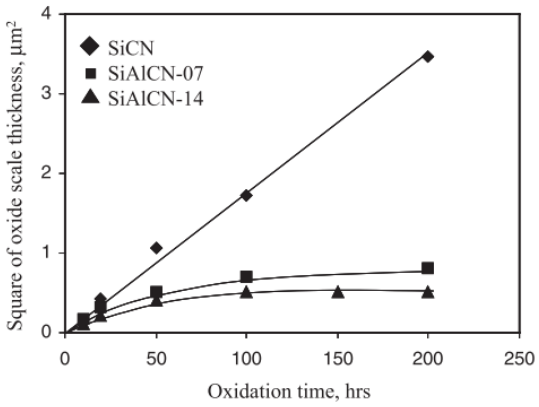

Figure 13 A plot of the square of the oxide scale thickness as a function of annealing time for both SiCN and SiAlCN at 1200°C in dry air.[58]

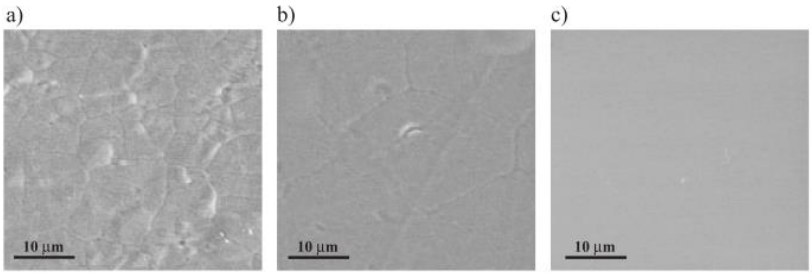

Figure 14 SEM micrographs of the surfaces of (a) SiCN, (b) SiAlCN-07 and (c) SiAlCN-14. The specimens first immersed in de-ionized water saturated with NaCl at 100°C, and then annealed at 1200°C for 50h in air.[58]

2.1.5.2 Mechanical Properties

Apart from PDCs fibres, the Si–C–O, and the Si–C–N systems have attracted detailed investigations in terms of bulk mechanical properties of PDCs. For both systems, mechanical properties have been measured at different pyrolysis temperatures, with the summarised reported results presented below in Table 1.[2] In addition to the excellent room-temperature mechanical properties, it is expected that such superior mechanical behaviours can be retained at high temperatures due to the absence of grain boundary phases.

Table 1 Summary of the Mechanical and Thermal Properties Measured on Bulk Samples of the Si–C–N and Si–C–O Systems. [2]

System	Bulk density, ρ (g/cm^3)	Elastic modulus, E (GPa)	Vickers hardness, HV (GPa)	Fracture strength. σ_F (MPa)	Poisson's ratio, (n)	Fracture toughness, K_{IC} (MPa · m$^{1/2}$)	Thermal expansion, α ($\times 10^6$ °C^{-1})
SiCN (Ceraset)	1.85-2.16	82-140	8.3-11.3	<1100	0.21-0.24	0.56-1.3	
SiCN (NVP200)	2.32	110-130	11-15	<118	–		–
SiCN (VT50)	1.95	105	6.1	88-146		2.1	3.08-3.96
SiCN (HVNG/HPS)	2.6	109-118	7.9-12.8	80-235			
Si(O)C (AHPCS)	2.3-2.9		9.13			1.4-1.67	
SiCO (sol-gel)	1.7-2.28	57-113	4.7-9.3	70-900		0.57-0.77	3.21
SiOC (MK)	2.23	101	6.4		0.11		
SiOC (SR350)	2.35	97.9	8.5	133-612		1.8	3.14

In general, the elastic moduli of PDCs systems of S-C-N and S-C-O is lower than that of the crystalline silicon carbides or silicon nitrides, due to the less densely packed systems of networks, which also lead to low densities.[2] For the conventional thermal pyrolysis routes of producing PDCs, higher annealing temperatures typically result in increased elastic modulus

as well as density because of the loss of H atoms in C-H bonds leading to more closely connected networks. Similar trends are observed for the hardness values of PDCs, where higher pyrolysis temperatures normally yield increased hardness, since more carbon atoms migrated into the silica networks, thus impose more restrictions on dislocations.[112] Extraordinary creep resistance is another interesting feature of (Si-based) PDCs, which have typical viscosities of three orders of magnitudes better than vitreous silica.[108]

2.1.5.3 Electrical Properties

Electronic behaviours of amorphous PDCs have gained extensive attentions because: a). they provide a unique model system for studying the structure-properties-performance relationships of complex amorphous covalent materials, and b). they could find the promising applications in harsh-environment sensing as well as MEMS.[54,113]

2.1.5.3.1 DC Conductivity

Haluschka *et al.*[103] have shown that the electrical properties of amorphous Si–C–N ceramics are in the range between the electrical properties of semi-conducting SiC and that of insulating Si_3N_4. Their results revealed that the DC conductivity is influenced by the conditions of the final heat treatment, namely the annealing time and temperature. Haluschka *et al.* identified three distinctive regimes: a) due to the loss of residual hydrogen and an increased sp^2-/sp^3-ratio of the carbon atoms, the conductivity of the amorphous SiCN matrix would experience a rise up to three orders of magnitude (up to 1300 ℃); b) due to the formation of SiC and the loss of nitrogen of the remaining amorphous a-SiC(N) matrix, the material had a pronounced conductivity increase (between 1300 and 1600 ℃); and c) lastly the nano-crystalline SiC particles were responsible for the conductivity increase by formation of percolation paths throughout the sample (above 1600 ℃).

2.1.5.3.2 AC-conductivity

Studies on AC (alternative current) behaviour (as shown below in Figure 15) of a PDC material (SiCN) show that at low frequencies the AC conductivity remains stable (attributed mainly to the long-range transport of charge carriers through the matrix-to-free-carbon path), while at high-frequency regime it rises with frequency (proposed to be caused by interfacial polarisation due to charge carrier relaxation within the free-carbon phase).[114]

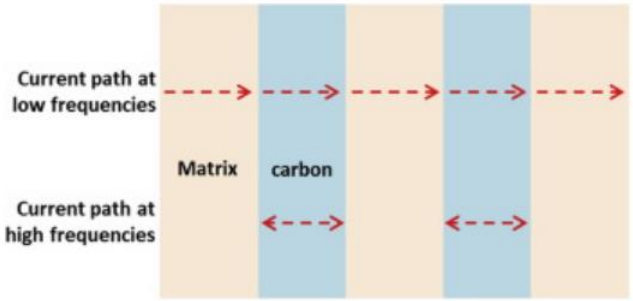

Figure 15 Schematic showing the conduction mechanisms in the a-SiCN at low and high frequency regions.[114]

2.1.5.4 Impedance

Complex impedance behaviors of polymer-derived amorphous SiCO and SiAlCO are reported.[115,116] Equivalent circuit models have been applied and showed fitting correspondence with the measured data. The conduction of current in both materials is found to pass through the matrix and free carbon phases in series, with the conductivity of both phase increases with increasing synthesis temperature, whereas the matrix has a significantly shorter relaxation time than that of the free carbon. The relaxation process of polymer-derived SiAlCO is found to move to higher frequency with increasing pyrolysis temperature.

Despite the investigative efforts made as discussed above, little attention has been focused on the interfacial areas sandwiched between the matrix and carbon phases. The role and effect of the interfaces deserve more in-depth investigations as the electrical behaviors may experience great influence from the interfaces between two phases with vastly different conductivities. [117] However, this has started to attract research efforts with some recent reports investigating mainly Si-C-N PDCs systems.

Strong interfacial charge polarisation has been reported to present, leading to giant relative permittivity. [118] The interfacial polarisation underwent relaxation processes (from -50 to 300 ℃), following a 3D random hopping mechanism, depend on the capacitance and resistance of the interfacial areas. [119] Employing complex impedance spectroscopy with superimposed direct current (dc) bias, Li *et al*. have applied a double Schottky barrier model to help determine the room temperature interfacial characteristics. The authors have revealed that the capacitance and resistance appeared to be independent of dc bias, whereas that of the interface is suppressed with increased dc bias voltage, with such effect attributed to bias influence on potential barrier height and barrier region width.[120]

Due to intense research interests on PDC as a promising candidate particularly for high-temperature sensing applications, it would provide more in-depth revelations to further study the interracial behaviours under elevated temperatures, and impedance spectroscopy with superimposed dc current bias on ac current remains a powerful pathway towards this aim.

2.1.5.5 Contacts between Metallic-Conducting Phase and Semi-Conducting Phase

Due to the bi-phasic nature of most Si-based PDCs, the interface sandwiched between the two phase becomes an accumulation venue for charge carriers when PDCs are under external AC current. The interface is therefore a highly conductive region, which may be treated as

possessing metallic-conducting characteristics. Furthermore, comparative to the highly-conductive interfacial phase, the free carbon phase as well as the ceramics matrix phase have semi-conducting behaviours. Therefore, the contact between the (highly-conductive) interface phase and the semi-conducting phase (either the free carbon phase or the ceramics matrix phase) have similar electrical conductive characteristics of the metal-semiconductor contacts. Here in the following contents, we will review the fundamental theories of the Schottky contact, which shows the non-linear, rectifying current voltage characteristics.[121]

For the energy band structures of either the interfaces or the (*n*-type) semi-conducting phase, their respective work functions are inherently different. With the work function of the interfaces being the minimum energy required to eject one electron (i.e., interfacial Fermi energy of $E_{F_{Inter}}$), whilst that of the semi-conducting phase has a work function of E_{F_C} (energy needed to "kick" an electron from the Fermi level at the conduction band). For discussion convenience purposes, we consider the contact between an *n*-type semi-conducting phase and the highly-conductive interfacial phase so that the Fermi level of the former phase is larger than that of the latter (i.e., $E_{F_{Inter}} < E_{F_C}$). Because of such energy level difference, when the interfaces phase makes contact with the semi-conducting phase (i.e., when the bi-phasic PDCs is placed under AC electric field forming the interfacial phase filled with accumulated charge carriers), the energy levels tend to align to reach thermodynamic equilibrium via the migration of charge carriers from the (high-energy level) conduction band to the (low energy level) interfacial regions. As the electrons depart from the semi-conducting phase, they also leave behind certain donor atoms with positive charges. Such process creates a region depleted of electrons (i.e., depletion zone). When thermodynamic equilibrium is achieved after contact has been fully established, the Fermi energy levels reach an aligned value in addition to the

formation of the depletion region. Therefore, the process results in a curved energy band in the semi-conducting phase. Such curved energy band acts as a potential barrier, impeding the flow of electrons from the semi-conducting phase to the interfaces.

Under complete thermodynamic equilibrium and without any external electric field, electrical neutrality dictates that the current flow from the semi-conducting phase to the interfaces is exactly matched by the flow of the reverse direction. However, when the AC electric field is biased due to a DC voltage, the current flows of the two directions becomes different. Under a forward DC bias (*V*), the potential barrier (at the semi-conductor side) is lowered (by a level of *V*). This eases the restrictions of electron migrations and therefore increased electron flow from the semi-conducting phase to the interfaces. Furthermore, since the potential barrier from the interfaces side remains the same, the level of electrons crossed into the semi-conducting phase is still unchanged. Such imbalance of the bi-direction electron flows effectively creates current from the interfaces to the semi-conducting phase. On the other hand, when under a reverse bias (of *V*), the potential barrier witnesses a rise (of *V*). Similar to the above discussions, the electron flows from the semi-conducting phase are reduced because of the heightened potential barrier. Since the interface-to-semiconductor current still remains unchanged, the resultant net current flows from the interfaces to the semi-conducting phase.

2.1.5.6 Piezo-resistivity

Some amorphous PDCs have been reported to demonstrate significant piezoresistivity, with a polymer-derived SiCN showed piezoresistive coefficients of an unprecedented 4000 [47] following a tunneling-percolation model based on Saha *et al.*[101] who proposed the formation of conductive graphene sheets within the framework of PDCs nano-domains. Similarly, the tunneling-percolation mechanism has been attributed to a reported high strain sensitivity of 145

of a PDC SiCO owing to the presence of a percolating network of electrical conductive free carbon.[102] Interestingly, the electrical resistance of SiCO rises with increased compressive stress, contrary to that of SiCN.

2.1.6 Magnetic Properties

Polymer derived ceramics containing ferrous elements have attracted research efforts investigating its magnetic behaviours. Since PDCs themselves are not inherently magnetic, one common approach to impart such properties is to incorporate PDCs with other ferrous materials or particles to make essentially PDCs composites. One less sophisticated method is to simply disperse Fe_3O_4 powders into liquid-phased polymeric precursors before undergoing a reduction process in graphite, yielding a high M_s of around 57 emu·g^{-1}.[122] Iron silicide fillers have also been incorporate into preceramics producing PDCs with cubic Fe_3Si particles embedded the matrix, showing an M_s of up to 17 emu·g^{-1}.[76] A more fundamental approach to synthesise magnetic PDCs is to modify the design at the molecular / polymeric backbone level, which is to add metallic iron atoms (e.g., via ferrocene).[2] Sun *et al*. have obtained phosphorus-containing PDCs with good magnetisation (M_s up to 50 emu·g^{-1}) exhibiting very low remanence and coercivity.[123] Higher (more than doubled magnetisation of 118 emu·g^{-1}) have been detected from Cobalt-containing PDCs which also retained similarly low remanence and coercivity.[124] In addition, the observed magnetic behaviours also agree with the evidence of the existence of domain-like regimes within PDCs matrix. And such functionalised PDCs with tunable electromagnetic properties may find promising applications as regenerable absorbers or regenerable diesel particulate traps.[76]

2.1.7 Optical Properties

Polymer derived ceramics did not initially attract much attention upon investigating its optical properties since most PDCs are not optically transparent. The blackish appearance of many PDCs is chiefly believed to have cause by the presence of sp^2 carbons forming light-absorbing graphitic thin layers.[2] However, research efforts have yielded largely transparent SiCO PDC discs (due to the lowered presence of sp^2 carbons). [125] These transparent PDCs show a luminescence band centering around 500 nm which the authors ascribed still to the sp^2 carbons. Produce via a sol-gel route, SiCO PDCs doped with Eu^{2+} proved to be a luminescent glass, with an emission band exhibit a peak in 450–480 nm.[126] With the aim of producing high-temperature stable materials for white light applications, an Italian team has pyrolyzed sol-gel derived SiOC PDCs films showing visible luminescence.[127] They show that different pyrolysis temperatures yielded luminescence of varying colours: bluish emitting from low-temperature annealed samples, whereas their high-temperature analogues exhibit green-yellow. Besides SiOC PDCs, polymer derived SiCN have also been reported with regard to its photo-luminescence behaviours and mechanisms.[128] In contrast to their SiCO counterparts, these N-containing PDCs show prominent luminescence at much lowered annealing temperatures (500 – 600 ℃), which the authors attributed to the microstructural re-arrangement as well as the presence of sp^2 carbon along with the formation of radicalized species. In addition, SiOCN PDCs have also been shown to exhibit intense photo-luminescence in the range of 500 – 800 nm.[129] The author also employed the previously-discussed nano-domain model to explain the luminescence phenomena, which they ascribed to the mixed bonds of Si–C–N–O tetrahedral.

2.1.8 Chemical Properties

Chemical stability of PDCs is the reason they attract research interest to develop and study in the first place, with the additional characteristics of superior oxidation resistance properties.[2] There have been extensive research reports with regard to the chemical durability of PDCs. Polymer derived SiOC ceramics have been put to the test of highly corrosive acidic and basic solutions to examine its chemical stability.[130] Compared to its silica counterparts, SiOC PDCs show much greater endurance because of the presence of Si-C bonds, and the cross-linked carbons as well as the highly disordered composition, which jointly retard the transport of nucleophilic species.

The oxidation behaviors of PDCs have been widely studied (with focus on systems of SiC, SiCO, SiCN, and SiBCN). Here, the pyrolysis processes play a vital role, since the elimination of H atoms is key to achieve parabolic oxidation rates.[2] Most systems investigated reveal a dense, continuous (defect-free) oxide layer above the ceramic interfacial areas. Efforts have also been devoted to the effects of additional elements incorporated with Si-C-N PDC systems (e.g., B, Al, as well as Zr), [109,131,132] relying on the blockage effect of these added atoms towards a dropped O_2 diffusion rates.

2.1.9 Applications of Polymer Derived Ceramics

As the above-discussed superior properties of polymer derived ceramics indicate, they could find numerous potential applications in various technical fields which this section aims to review and correlate the structure, processing and properties relationships.

The fundamental mechanism of application / properties tailoring lies with the versatile capability of designing the microstructures of the pre-ceramic polymers at a molecular level.

When combined with various types of fillers as previously discussed (e.g., metallic and polymeric), the properties of PDCs can be tuned to meet or more often exceed conventional ceramics in terms of mechanical strength, electrical / dielectric behaviours, and oxidation / corrosion resistance. It is therefore promising both in terms of fundamental research as well practical applications to study the properties of PDCs more in-depth.

2.1.9.1 PDCs Protective Coatings

Since the processing of polymer derived ceramics is based on liquid phased polymeric precursors, coatings / thin membranes could be produced while retaining the exceptional wear / oxidation / corrosion resistance capabilities.[133] SiCO coatings have been applied on to fibres acting as flame / temperature shields.[1] SiCN has also been spray coated on conventional substrates against oxidising environments and mechanical wears.[134] Similar techniques have produced porous SiCN membranes aimed for gas (e.g., hydrogens) separation under high temperatures.[135]

2.1.9.2 Micro-electro-mechanical Systems (MEMS)

The successful development of micro- or nano- electro mechanical systems relies on the inter-connectivity of different components of various sizes. This again depends on the capability of producing parts with complex shapes / dimensions. Conventional methods, besides the lack of high accuracy, are limited in terms of this aspect, since molds of pre-determined corresponding shapes would need to be manufactured first, which is also less cost-effective. The (high temperature as well as harsh environment) mechanical strength of polymer derived ceramics makes them a very promising candidate for MEMS components with desired features can be as small as less than one micron achievable via lithographic techniques.[136] Typical examples of polymer derived ceramics MEMS include: electrostatic actuators (which could also find use

in high power laser systems)[54], photonic crystals[137], as well as embossed micro-fluidic channels[138].

2.1.9.3 PDCs Fibres

The fibres, which are composite in nature, made from polymer derived ceramics combines both the strength of carbon fibres and oxidation / corrosion resistance of ceramics. These PDC fibres have found wide applications as ceramics reinforcements and have attracted extensive further research interests for performance optimisations. Till today, three generations of PDC (mainly non-oxide) fibres have been developed, with the latest ones have already been successfully commercialised possessing exceptional thermal stability as well as very high Young's modulus. Flores *et al*. have reported polymer derived SiCN fibres which can retain a Young's modulus of over 300 GPa under temperatures as high as 1400 degrees Celsius.[139]

2.1.9.4 Polymer Derived Composites

Though polymer derived ceramics themselves already possess composites-like properties, tremendous interests and efforts have still been devoted to the further development of PDC-based composites combining the superior properties of many other newly-discovered nano materials. Carbon nanotubes / PDC composites have been reported with the modulus, hardness, as well as damage resistance of the reinforced composite product greatly improved even with just a small amount of multi-walled carbon nanotubes incorporated.[51]

2.1.9.5 Sensing Materials / Devices based on Polymer Derived Ceramics

As discussed in previous sections, one of the most unique aspects of PDCs are that their microstructures could change with external parameters (e.g., temperature, stress, and strain),

which lead to detectable changes in intrinsic bulk properties (such as: thermal coefficient, electrical conductivity, as well as relative permittivity).

Heat flux sensor for gas turbine environment under high temperatures have been reported based on polymer derived SiCN via lithography microfabrication techniques.[140] Temperature sensors have also been variously reported take advantage of the "tunneling percolation" effect due to microstructural changes. One example demonstrated a wireless PDC (SiCN) sensor based on cavity radio frequency resonator.[141] Another showed a SiAlCN-based high temperature sensor with retained good accuracy even after many repetitive cycles.[142]

Pressure sensor, with desired shapes and very high hardness (23 GPa), for high temperatures have also been reported employing the drag effect.[143] Gas sensing capabilities of PDCs have also been investigated, with hydrogen sensors being explored owing to the semiconducting behavior of polymer derived SiCN which were reported to show good performance up to 785 K.[144]

2.2 Polymer-Derived SiAlCN Ceramics

Due to excellent oxidation and corrosion resistance[111], anomalously high piezoresistivity[47] as well as its capability for temperature measurement in harsh environment[142], SiAlCN has become a novel promising candidate of high-temperature multi-functional material. It is particularly attractive to apply and integrate the PDCs into wireless sensing systems and embedded within the interior regions of moving parts of turbine engines, highly irradiative surfaces of gasifiers / reactors to detect the real-time temperatures and pressures to gain reliable and accurate feedbacks for system operation optimisations. Its excellent mechanical strength

means it could also find potential future applications in civil engineering field for structural health monitoring (for example: high-rise buildings or long-span bridges).

Polymer-derived SiAlCN ceramics has been found to have more superior oxidation resistance than other silicon-based materials, with the oxidation rate for the SiAlCN is about an order of magnitude lower than that for pure silicon carbide/nitride.[58,110] It was also observed that SiAlCN exhibits excellent water-vapour corrosion resistance under 1100 ℃, which was attributed to the formation of aluminum-doped cristobalite oxide scale.[111]

Electric properties characterisations of PDC SiAlCN show a smooth increase of DC conductivity with elevated sintering temperatures.[3] The dielectric measurements revealed that the dielectric constant and dielectric loss rise with increasing temperature.[3]

Temperature sensor design based on polymer-derived SiAlCN for high-temperature applications has been reported.[142] The sensor resistance showed a monotonous change with ambient temperature (up to 830 ℃), and has demonstrated excellent accuracy repeatability to both uni-directional and bi-directional temperature variations.

2.3 Desalination Membranes

The imminent risks of global water shortages pose as threats not only to those directly impacted due to the lack of clean water for everyday usage, industrial waste processing and treatment, as well as agricultural irrigations, but also cause collateral damages to the society since the imbalance of such basic human needs of accessing clean water would induce social unrest and conflicts. [6]

As a readily accessible and abundant resource, seawater has the promising potential of greatly reducing the risks of the fresh water shortage. However, as a complex mixture of various types

of salt, water, and dissolved solvents, seawater is not directly potable or useful for industrial or agricultural demands. For decades, researchers and engineers have been exploring materials and techniques for removing the mineral components within seawater in an efficient and cost-effective manner. Durable and selective-filtering membranes have been the dominant candidates for such applications, with the polymeric membranes still account for the majority of the commercially available products. [8] With respect to the most widely-adopted desalination techniques, reverse-osmosis (RO) have been the dominant method for producing large amounts of fresh water, with multistage flash (MSF), multi-effect distillation (MED) are also attracting increasing attentions. RO is a high-pressure membrane process that utilises a semipermeable polymeric membrane to retain salts and low-molecular-weight solutes while allowing the passage of water via diffusion. However, a major drawback of RO remains, which is its high energy demands due to the pressurisation process, which in turn contributes to the release of greenhouse gases from fueling burning. The polymeric membranes developed decades ago have underwent significant modifications in terms of increasing desalination performances for example new polymerisation routes, developing thin-film composite membranes, as well as post-synthesis surface modifications to obtain membranes with high permeability, salt rejection rates, fouling-resistant capability, and chlorine-tolerance. In addition, future challenges for desalination technique also come from integrating renewable energy source, as well as stringent water standard and brine management.[9]

In addition to the polymeric-based membranes, there have been many recently developed materials for desalination applications, although not fully capable of large-scale industrial usage. For example, ceramics-based membranes have been used in harsh environmental situations (e.g., high-temperature, highly-radioactive feeds, and highly-reactive components) where polymeric membranes could not endure. [145] Furthermore, mixed matrix membranes (e.g.,

incorporating zeolite nano-particles) have been developed with smoother, more hydrophilic surface exhibiting improvement in salt rejection rates.[146] Another category of novel desalination membrane involves the incorporation of carbon nanotubes (CNTs) which have been excellent water transport. However, although CNTs-integrated membranes show great promise in flux enhancement, efficient synthesis methods to produce membranes with well-aligned CNTs, as well as the development of surface modifications for more efficient salt rejection remain major obstacles for future applications.[147]

Nano-structured RO membranes offer inherently high permeability as well as salt ions rejection, while the development of nanotechnologies could bring forth multitudes of innovative progresses towards high-performing desalination membranes. However, practical issues of cost-effectiveness, scaling-up, and potential health risks still demand extensive investigations. [9]

2.4 Two-Dimensional Materials for Desalination Applications

As a promising alternative to the conventional polymeric desalination membranes, a viable potential solution stands with engineering the structure of traditional materials into tailored porosity or exploring a new type of intrinsically porous nanomaterials-based membranes. Recently developed two-dimensional (2D) materials present unprecedented opportunities for water desalination and molecular sieving technologies owing to their structural uniqueness.[11-13] Their extremely small thickness (i.e., a few Å for 2D monolayers) projects superior water permeation rates benefiting from small diffusion lengths for molecular transports while their high mechanical flexibility renders advantages for membrane integrations. Moreover, 2D materials produced by chemical synthetic routes possess high-density "intrinsic" structural imperfections (e.g., near atomic vacancies) whose physical dimensions are comparable to those

of salt ions and water molecules.[14] In this endeavor, a variety of 2D materials have been explored including graphene,[15-18] dichalcogenides,[19-22] and graphene oxides,[23-26] along with substantive efforts for the structural engineering of traditional membrane materials such as zeolites,[27-30] and metal-organic frameworks [31-34].

Although for graphene in its pristine form is impervious to water molecules, techniques to generate nanopores on graphene sheets have been developed, and the nanoporous graphene membranes have shown great potential in desalination performances, with some investigations have demonstrated their capability of withstanding high pressures associated with RO. For example, Suk *et al*. have shown that graphene-based membranes show water permeation rates of 2–3 orders of magnitude higher compared to conventional RO membranes, with salt rejections approaching 100%.[148] However, mature techniques for producing large-area graphene with well-defined distribution of nanopores are still absent at this stage of research. [15] In addition to graphene-based membranes, graphene-oxide-based membranes offer many desiring features for potential water treatment technologies including distinct microstructural design, hydrophilicity, excellent mechanical strength, as well as good anti-fouling performances.

In addition to graphene and GOs based desalination membranes, many other types of 2D nanoporous membranes have been investigated for their potential for filtration applications owing to their ultra-thinness as well as inherent nano-sized pores for impeding salt ion translocations. For example, zeolites are composed of three-dimensionally interconnected nanopores of 0.3-0.8 nm, and have been shown to be able to effectively reject salt ions, while retaining a water permeability of 40 L/(cm^2 · day · MPa), similar to that of graphene.[149] Moreover, covalent organic frameworks (COFs) consisting of tunable and precisely controlled nanopores

have been proposed as a promising candidate for filtration ultrathin membranes. For instance, Triazine framework nanoporous membranes have demonstrated a water permeation of 24.6 L/(cm^2 day MPa), and a salt rejections rate of nearly 100%.[150] Furthermore, owing to their high flexibility, mechanical strength, and hydrophilicity, MXenes with controllable thickness can also yield suitable membranes for separation applications with ultra-fast water flux. $Ti_3C_2T_x$ MXene membranes have been shown to have a water flux of 37.4 L/(m^2 h bar), due to the hydrophilic nature of the material and the presence of intra-layer water molecules. [151]

2D materials of mono-to-few layers (e.g., h-BN, phosphorene, and MoS_2) have attracted extensive investigations towards their potentials for ionic sieving. A prominent example is 2D MoS_2 which have been fabricated for nanoporous membranes for desalination applications, in addition to many theoretical projections of their performances. MoS_2 also demonstrates excellent mechanical properties (e.g., MoS_2 nanoporous 1 nm-thick membrane possesses a Young's modulus of 270 GPa), as well as good flexibility. 2D molybdenum disulfide (MoS_2) layers have recently gained significant interests for a wide range of water and environmental technologies. They not only share the intrinsic structural advantages inherent to other 2D materials but also present additional suitability such as excellent chemical stability and non-toxicity.[35-37] Furthermore, a variety of structural variations such as point defects, grain boundaries, and van der Waals (vdW) gaps have been ubiquitously observed in 2D MoS_2 layers grown via chemical vapour deposition (CVD) process.[38-40] Such "intrinsically" present structural imperfections of very high concentration (e.g., areal density of ~10^{13} cm^{-2} for sulphur vacancies[41]) offer 2D MoS_2 layers high promise as an efficient membrane material for water desalination applications. In fact, several studies based on theoretical calculations and molecular dynamics simulations have predicted superior desalination performances of monolayer 2D MoS_2.[14,19,41,152,153] Heiranian *et al*. have predicted that 2D MoS_2 monolayers of

enriched defective sites can exhibit ~2-5 orders-of-magnitude higher water fluxes than traditional filtration membranes, which is even 70% greater than the performance of graphene nanopores.[154] Köhler *et al*. have projected that the ion rejection capability of 2D MoS_2 membranes is superior to graphene under a wide range of test conditions including pressure, nanopore size, and cation valences.[152] Li *et al.* have simulated the desalination performance of 2D MoS_2 layers, demonstrating high water transport rate (355.3 L m^{-2} h^{-1} bar^{-1}) and excellent salt rejection capability.[155] Despite the theoretically-projected promise of 2D MoS_2 layers, their experimental utilisation for membrane-based desalination technologies has been rarely approached. A few experimental studies have explored MoS_2 laminar membranes of very large thickness (typically, ~1-10 μm) constituting mechanically stacked individual 2D flakes.[14] Sun *et al*. studied ~1.7 μm thick MoS_2 membrane films prepared via chemical exfoliation and subsequent filtration of aqueous dispersion.[156] Hirunpinyopas *et al.* demonstrated chemically functionalised ~5 μm thick laminar membranes composed of exfoliated 2D MoS_2 flakes employing the similar filtration process.[157] These laminar 2D MoS_2 membranes of large thickness have exhibited significantly limited desalination efficiencies, failing in meriting the structural uniqueness and performance advantages projected with near atom-thick membranes. For example, their water permeation rates were experimentally identified to be in a range of ~245-275 L m^{-2} h^{-1} bar^{-1},[156,157] significantly falling short of theoretical values predicted by simulation studies.[154] Moreover, ion rejection rates of mere ~15-30% were reported for pristine laminar 2D MoS_2 membranes of ~1-5 μm thickness. Scarcity of experimental studies on the 2D MoS_2 layers-based membranes of near atomic thickness for water desalination is attributed to technical difficulties associated with integrating 2D layers preserving their structural integrity. Particularly, it has been challenging to produce large-scale (> cm^2) "continuous" 2D

MoS_2 layers of ~1-10 nm thickness and their seamless integration onto porous substrates, hindering their applications to desalination technologies.

CHAPTER 3: INTERFACIAL CHARACTERISTICS OF POLYMER DERIVED SIALCN CERAMICS[1]

3.1 Introduction

The bi-phasic nature of PDCs features two phases of different conductivities, with the free-carbon phase exhibited higher conductivity than the amorphous matrix phase. The difference in conductivity between the two phases gives the materials many unique electrical properties, notably high-temperature semiconducting behaviour [46,158] and anomalous piezoresistivity.[47,159] It was shown that the dc (direct current) conductive behaviour of PDCs was determined by the concentration of the free-carbon phase.[95] When the free-carbon content is high, a tunneling percolation network is formed by the free-carbon clusters, leading to high piezoresistivity.[160] On the other hand, when the free-carbon content is low, the materials exhibit amorphous semiconducting behavior.[161]

Previous studies also demonstrated that the electric heterogeneity resulted in an internal potential barrier at the interface between the matrix and the free-carbon clusters. This barrier caused the transition of the ac (alternating current) conduction mechanism from the long-distance transport of the charge carriers to the interfacial polarisation.[114] The barrier also led to a very high permittivity in PDCs.[118,162] Given its importance in determining the dielectric behaviour of PDCs, the behavior of the barrier itself has yet been explored.[120]

In this study, the behaviour of the internal potential barrier is studied by using a polymer-derived amorphous silicoaluminum carbonitride (*a*-SiAlCN) as the model material, which

[1] Part of contents in this Chapter contains published works adapted with permission from: Hao Li, Baisheng Ma, & Linan An. Effect of temperature on internal potential barriers in polymer-derived amorphous ceramics. *Ceramics International* **45**, 13575-13578 (2019). Copyright 2019 Elsevier Ltd and Techna Group. Published on March 30th 2019. Hao Li prepared the samples and conducted part of materials characterization, as well as analyzed the data.

exhibited excellent oxidation and corrosion resistance.[58,109] It is revealed that the interfacial capacitance of the material can be described by a double Schottky barrier model. The height of the barrier and the charge-carrier concentration exhibit Arrhenius dependence on testing temperature and annealing temperature respectively. The results are discussed in terms of the electronic structures of the material.

3.2 Experimental Methods

The *a*-SiAlCN studied here was prepared from a polyaluminasilazane precursor following the procedure as previously reported.[163] First, the precursor was synthesized by mixing/reacting liquid polysilazane (VL20, Kion, Huntingdon Valley, PA) as the major precursor with 20 wt% poly (melamine-co-formaldehyde) acrylated solution (PVN, Sigma-Aldrich, St. Louis, MO) as the N source and 5 wt% aluminumtri-sec-butoxide (ASB, Sigma-Aldrich, St. Louis, MO) as the Al source. The mixing/reacting was carried out at 80 °C for 12 h under continuous stirring to ensure the completion of the reaction. The synthesized precursor was then photo-cured under ultraviolet light, followed by heat-treatment at 120 °C for 12 h to enhance cross-link. The cross-linked samples were finally annealed at different temperatures (i.e., 1100, 1300, and 1400 ℃) for 4 h to obtain *a*-SiAlCN ceramic specimens of 10 mm in diameter and 1 mm in thickness. The entire procedure was protected by flowing ultrahigh-purity argon. The obtained samples were characterised via X-Ray diffraction utilising a Rigaku D/MAX Xray Diffractometer (XRD Rigaku, Tokyo, Japan) with a monochromatic Cu-Kα radiation (λ=0.154 nm), which confirmed that they are amorphous without detectable crystalline phase. Furthermore, Raman spectroscopy was also used to examine the microstructural evolution of the free carbon phase in the material. Raman spectra of samples prepared under different pyrolysis temperatures were obtained from the Renishaw inVia Raman microscopy (Renishaw Inc., Gloucestershire, UK).

The excitation source was a 532 nm line of silicon-solid laser. For each sample, 25 Raman spectra were obtained by a 10 μm×10 μm mapping acquisition for measurement accuracy.

To obtain the complex impedance spectra of the samples, silver paste was painted on their surfaces as the electrodes. The spectra were acquired in a frequency range of 4 Hz–10 MHz on an Agilent 4294 A precision impedance analyzer with a 16065 A external voltage bias fixture. The measurement was performed at different temperatures (i.e., testing temperature range of 50-150 ℃ and on samples underwent annealing treatment from 1100 to 1400 ℃), and dc bias (0-10 V).

3.3 Results and Discussions

3.3.1 Raman Spectroscopy and XRD

Raman spectroscopy is a useful characterisation tool for investigating the formation and evolution of free carbon phase in PDCs.[164] As shown in the Raman spectra (Figure 16), two prominent bands at approximately 1350 cm^{-1} ("D-band" resulting from breathing modes of sp^2 carbon atoms in rings) and 1582 cm^{-1} ("G-band" due to in-plane bond stretching of sp^2 carbon) can be observed, which feature the presence of free carbon.[165,166] As shown in Figure 16, both the D and G peaks exhibit shifting trend as annealing temperature increases, with the G peaks showing an up-shift, whereas the D peaks exhibit an initial up-shift before remained stable around 1350 cm^{-1}. Such shifts stemmed from microstructural changes: the up-shift of D peak reflects the increase in the number of ordered three-fold aromatic rings, whereas that of the G peak indicates the transition from disordered carbon to nanocrystalline carbon.[167] Such shifting patterns along with the decrease in the widths of D and G peaks indicate the graphitisation process of the free carbon phase as it transitions from amorphous carbon to nanocrystalline

graphite as annealing temperature increases.[166,167] An increase of the D-to-G peak intensity ratio was observed as annealing temperature increased, resulting from the in-plane growth of nanopolycrystalline graphite.[166,167] In addition, it has been revealed that during the pyrolysis stage of PDCs, large amounts of unpaired electrons (i.e., dangling bonds) are formed owing to the release of hydrogen and methane,[168-170] where the unpaired electrons are related to the carbon-dangling bond in the free carbon phase.[3,170] The presence of these unpaired electrons facilitates charge accumulation under AC field at the interface between the matrix and free carbon phases which exhibit different conductivities.[118]

XRD analysis revealed that samples pyrolyzed at up to 1400 ℃ are amorphous exhibiting no obvious diffraction peaks, indicating that they are all amorphous without significant indications of the formation of crystalline carbon, which is expected to appear at higher temperatures (Figure 17). The amorphous feature is common to most polymer derived ceramics with comparable annealing history.[114,171]

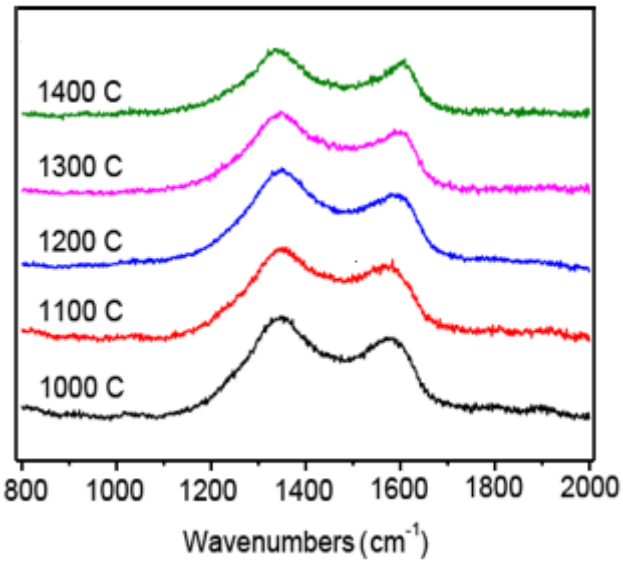

Figure 16 Raman spectra of SiAlCN samples pyrolyzed at different temperatures.

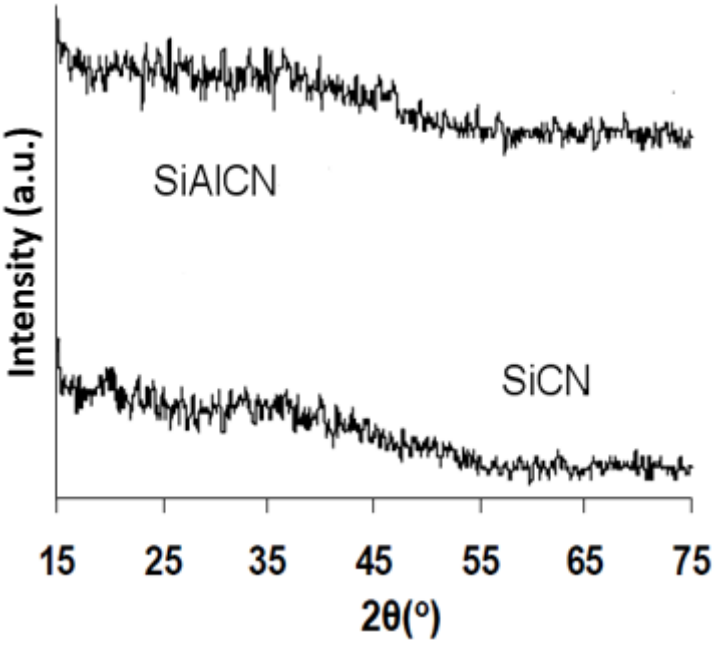

Figure 17 XRD of SiAlCN sample at 1400 ℃, with that of SiCN for reference.

3.3.2 Effect of Testing Temperature

Figure 18 shows the typical complex impedance spectra of the *a*-SiAlCN, obtained under various testing temperatures without the effect of bias. It is seen that all the spectra contain two semi-circular arcs. Previous study demonstrated that the one in high-frequency region (left) corresponds to the free-carbon phase, and the other in low-frequency region (right) corresponds to the amorphous matrix.[116] In addition, only moderate decrease in impedance was observed as the temperature increased, since such modest change in testing temperature would not cause microstructural rearrangements or any changes in chemical compositions in PDCs due to its superior thermal stability.[93]

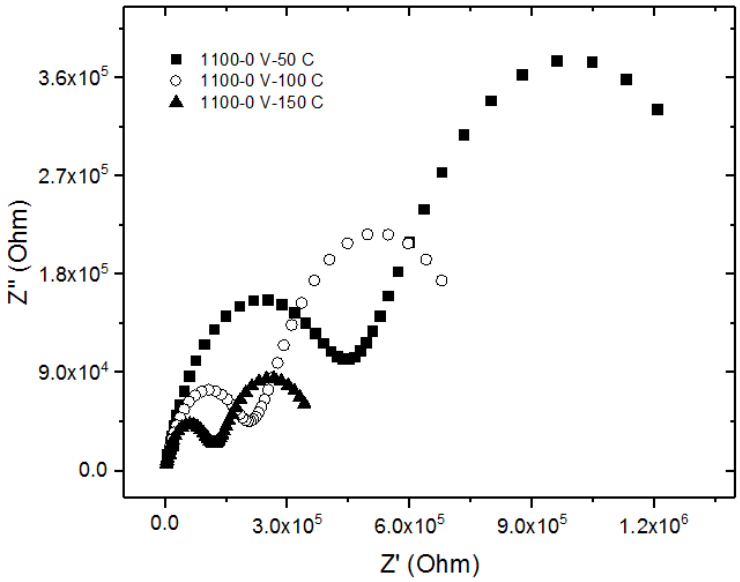

Figure 18 Influence of testing temperature on the complex impedance of the *a*-SiAlCN ceramics, without bias.

Typical impedance spectra of the *a*-SiAlCN under different bias are shown in Figure 19, with the specimen kept under 150 °C testing temperature. It is interesting to note that the response of the free-carbon phase is not affected by the dc bias; but the response of the amorphous matrix is greatly held down as the dc bias increases. This indicates that the arc in low-frequency area has significant contribution from the interfacial polarisation.[172]

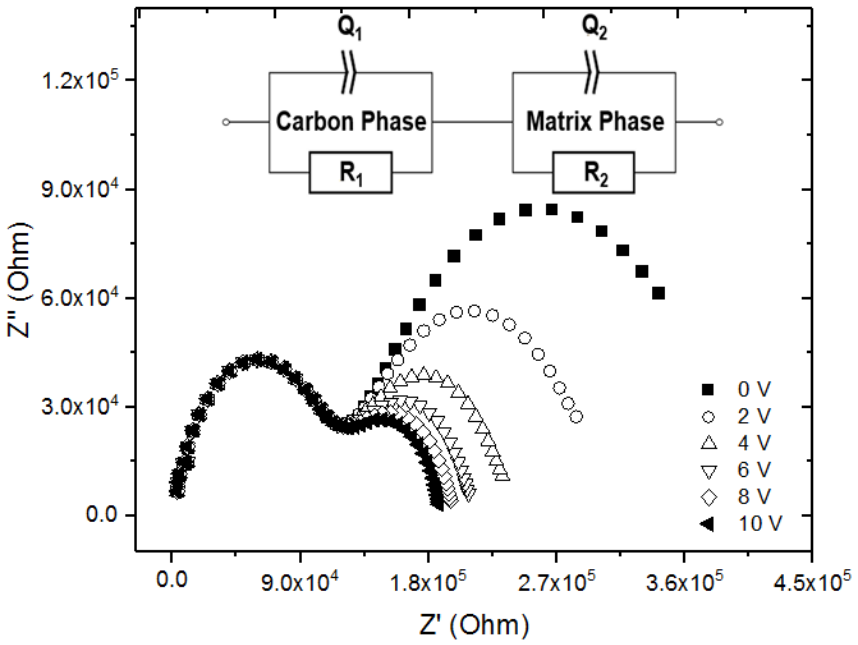

Figure 19 The complex impedance spectra of the *a*-SiAlCN, measured at 150 ^{o}C under different dc bias as labeled. The inset is the equivalent circuit used to analyze the spectra.

The spectra were further analysed by curve-fitting them with a modified-Debye equivalent circuit comprised of two parallel constant phase element (*CPE* or *Q*)-resistance (*R*) circuits connected in series (the inset in Figure 19). The parameters obtained from the best fitting are summarized in Table 2. As can be seen, the capacitance (C_2) of the amorphous matrix is about three orders of magnitude higher than that (C_1) of the free-carbon phase, suggesting that the capacitance of the amorphous matrix is mainly due to the contribution from the internal barriers.[172] The applied bias has negligible effect on the resistance and capacitance of the free-carbon phase. In contrast, the resistance of the amorphous matrix and the capacitance of the interface decrease with increasing dc bias levels. Similar trends were observed at all testing temperatures.

.

Table 2 Parameters obtained by curve-fitting the impedance spectra in Figure 19

Bias (V)	R_1 (ohm)	C_1 (nF)	R_2 (ohm)	C_2 (nF)
0	1.18×10^5	4.46×10^{-3}	2.89×10^5	2.69
2	1.17×10^5	4.42×10^{-3}	1.88×10^5	1.49
4	1.16×10^5	4.36×10^{-3}	1.23×10^5	1.15
6	1.15×10^5	4.33×10^{-3}	9.68×10^4	0.97
8	1.15×10^5	4.31×10^{-3}	8.33×10^4	0.88
10	1.15×10^5	4.31×10^{-3}	7.50×10^4	0.81

Previous studies suggested that in heterogeneity materials, a Schottky barrier could be formed at the interface between the phases with different conductivities.[173] This barrier provides extrinsic capacitance. The dependence of the interfacial capacitance on the applied dc bias can be described by a double Schottky barrier model.[172,173] According to the model, the interfacial capacitance can be related to the dc bias by the following equation[174]

$$(\frac{1}{C}-\frac{1}{2C_o})^2=\frac{2}{\varepsilon' qN_d}(\phi_b-V) \qquad (1)$$

where C and C_o are capacitances of the interface with and without the applied dc bias, respectively; ε' is the permittivity of the material; q is the electronic charge; N_d is the charge carrier concentration in the more conducting phase; ϕ_b is the height of the potential barrier; and V is the applied dc bias. This equation suggests that the modified capacitance ($(\frac{1}{C}-\frac{1}{2C_o})^2$) should exhibit a linear relationship with the bias.

Figure 20 is a typical plot of $(\frac{1}{C} - \frac{1}{2C_0})^2$ as a function of *V*, using the data obtained from the *a*-SiAlCN at 150 ^{o}C (Table 2). The good linear trend indicates that the double Schottky barrier model well represents the behaviour of the *a*-SiAlCN, similar to that reported previously.[120] This result is not surprising since the microstructure of the *a*-SiAlCN is comparable to that of the inter barrier layer capacitor (IBLC),[173,175] with the free-carbon clusters analogous to the relatively conducting grains and the amorphous matrix analogous to the relative insulating grain boundaries.

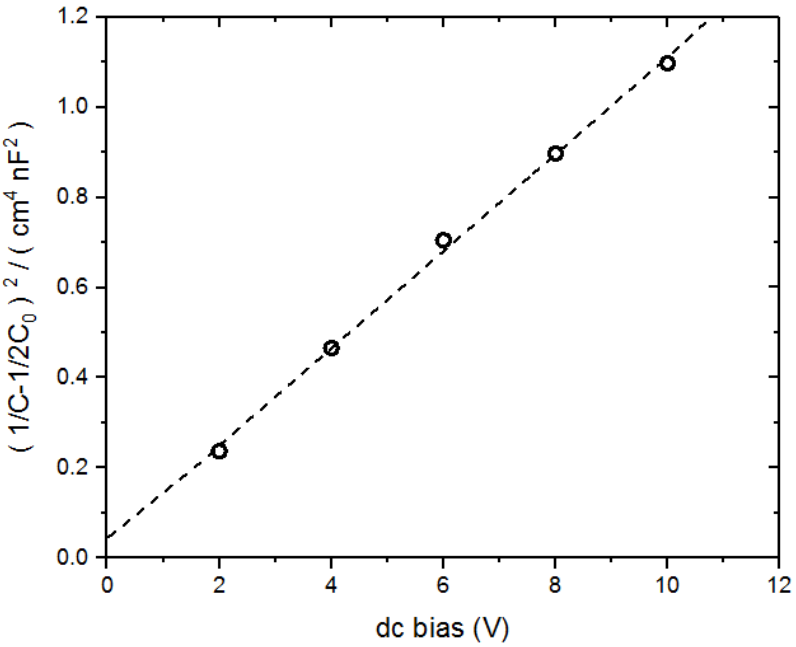

Figure 20 Plot of the modified interfacial capacitance vs. dc bias, using the data obtained at 150℃.

The interfacial behaviour was then studied by estimating the charge-carrier concentration and the potential barrier height of the *a*-SiAlCN from the intercept and the slope of the fitting lines obtained at various testing temperatures. Figure 21 shows the dependence of the charge-carrier concentration and the potential barrier height on testing temperature. It is seen that the charge-

carrier concentration increases with increasing testing temperature, but the barrier height decreases with increasing testing temperature. The figure also reveals that both the charge-carrier concentration and the barrier height exhibit Arrhenius dependence on testing temperature, indicating that they are dominated by thermally active processes. The estimated activation energies are 0.07 eV and 0.054 eV for charge-carrier concentration and barrier height, respectively. The difference in the activation energy suggests that they are governed by different processes.

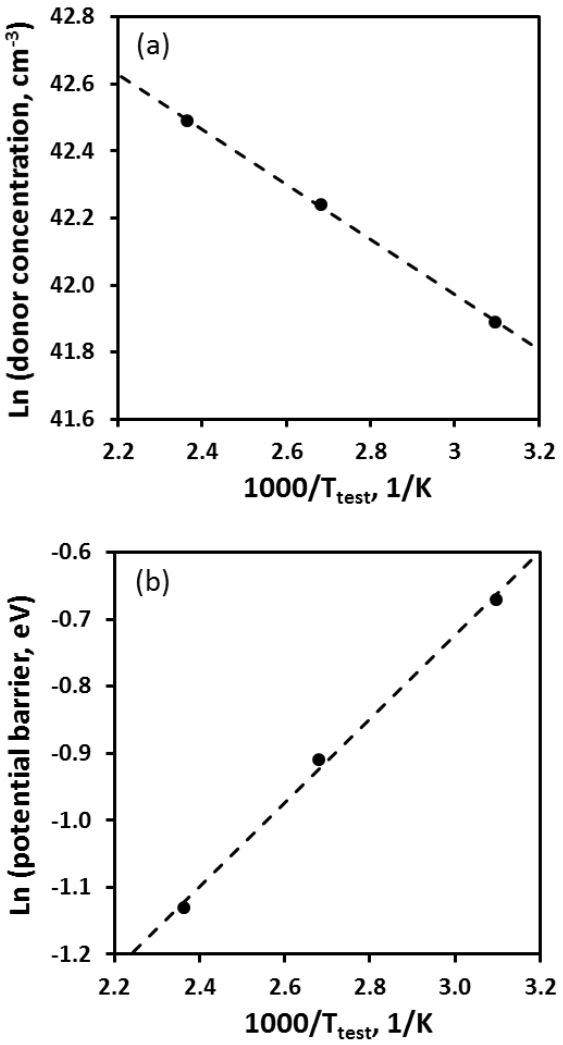

Figure 21 The influence of testing temperature on the charge-carrier concentration (a) and potential barrier (b).

The above phenomena can be correlated to the unique heterogeneous structure of the *a*-SiAlCN. Previous studies demonstrated that both the free-carbon phase and the amorphous ceramic matrix are *n*-type semiconductors with significantly different conductivities.[95,164] The gaps between Fermi energy and conduction band are different for the amorphous Si-based ceramics and the free-carbon phases.[161,176] A Schottky barrier can then be established between the two phases with the potential height approximating to the difference between their Fermi levels. As

a result, double (back-to-back) Schottky barriers are created at the interfaces between *n*-type free-carbon clusters (Figure 22).

The formation of the internal potential barrier is discussed below. At the point immediately after the bi-phasic PDC is under external AC electric field, the free carbon phase and the ceramic matrix phase establish close electrical contact where the respective Fermi energy levels (E_F) are still different and not in thermal equilibrium (i.e., as shown in the flatband diagram in Figure 22a, where E_{BT} and E_F represent the mobility edge for band-tail and Fermi level at this point, respectively). Because of the Fermi energy levels difference between the free carbon and the ceramics matrix phase, the electrons in the free carbon phase tend to transverse through the junction to lower their energy. The departed electrons leave behind, due to the ionised donor atoms, a positive charge, which then causes the formation of a negative field and lowers the band edges of free carbon. Thermal equilibrium will finally be achieved (i.e., no net electrons flow) when the free-carbon-to-matrix electrons diffusion equals the electrons-drifting stemming from the formed internal electric field.[177] A leveled Fermi energy is thus reached at thermal equilibrium, with the band tail being bent therefore a potential barrier to overcome (as shown in Figure 22b).

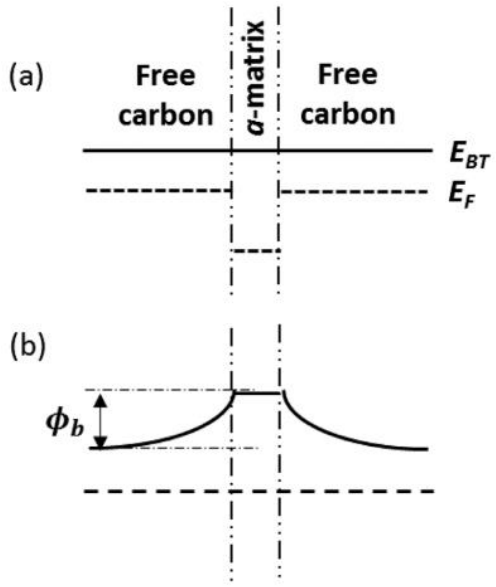

Figure 22 Schematic illustrations of the energy structure of the *a*-SiAlCN, (a) flatband diagram and (b) thermal equilibrium diagram. A back-to-back double Schottky barrier is formed as the gap between the band tail (E_{BT}) and Fermi level (E_F) for the free-carbon phase is different from that of the matrix phase.

According to this model, the increase in charge carrier concentration with temperature (Figure 21a) suggests that more electrons are excited to the band tail in the free-carbon phase. This can be understood as follows. For crystalline semiconductors, the charge-carrier concentration is fixed by the doping concentration and is temperature independent within a reasonable temperature range. However, for amorphous semiconductors, since chemical environment is different from defect to defect, the energy level of defects (dangling bonds) is varied in a range to form a narrow defect band within the band gap. Accordingly, increasing temperature will activate more defects, leading to more charge carriers. The activation energy estimated from the plot in Figure 21a is likely corresponds to the difference between the band-tail and defect levels. This is consistent with the fact that the material exhibited the band-tail hopping conduction behavior in the temperature range used here.[158]

The cause for the change in barrier height with temperature (i.e., a 0.19 eV change within a temperature range of 100 °C) is rather complex. Two possible factors could lead to an increase in Fermi level: (1) increasing temperature (increasing temperature could reduce the band gap); and (2) increasing concentrations of active defects. In the present study, the first factor (i.e., band gap drop due to increasing temperature) would play only a negligible role, since the coefficient for the temperature-dependent band gap change would only appear at a miniscule level,[178] and therefore would not be able to cause any significant effect over a moderate (100 °C) temperature increase. On the other hand, increasing temperature leads to higher levels of active dopants (dangling defects) concentrations for both the free carbon and the amorphous matrix, which lead to an increased Fermi level in both phases. However, the two phases experience different degrees of the Fermi level changes: the amorphous matrix would witness a more substantial rise (exhibiting stronger temperature dependence), because of the deeper defect levels in the amorphous matrix compared to its free carbon counterparts. Such variation in the magnitudes of Fermi level rise in the two phases would therefore result in a reduced difference between the Fermi energy in the free carbon and amorphous matrix phases, which leads to the decrease in the potential barrier height. Since the charge-carrier concentration has Arrhenius temperature dependence for both the free carbon and the amorphous, the potential barrier should exhibit similar Arrhenius temperature-dependence, which is consistent with the experimental results shown in Figure 21b.

3.3.3 Effect of Annealing Temperature

As a more systematic approach towards studying the interfacial behaviors of PDCs, the influence of annealing temperatures on the internal potential barrier was also assessed in addition to that of the testing temperature. As discussed in the above section, the range of

variation in testing temperature did not cause microstructural rearrangements or band gap drop. Instead, an increased Fermi level in both phases was induced by increased concentrations of thermally-activated defects.

In contrast, variations in annealing temperatures of PDCs would have profound effects in both microstructural evolutions and electronic structure changes.[171,179] It is well-established that both the free carbon phase and the amorphous matrix phase experience a gradual increase in the degree of order with increasing annealing temperature.[115] On one hand for the free carbon phase, increasing annealing temperature induces a transformation from amorphous carbon to nanocrystalline graphite,[105] accompanied by the sp^3–sp^2 transition.[180] One the other hand for the amorphous matrix phase, it has been revealed that as annealing temperature increases, the major structural evolutions involve the de-mixing of the SiC_xN_{4-x} mixed bonds, resulting in the shrinkage of the SiC_xN_{4-x} area, thus a reduced number of the mix-bonded silicon tetrahedral, and therefore a more ordered structure.[170,171,181,182]

Figure 23 shows the typical complex impedance spectra of the *a*-SiAlCN, obtained under various annealing temperatures, under the same testing conditions without the effect of dc bias. It shows more drastic changes in impedance due to increased annealing temperatures in comparison with the influence of varying testing temperature (e.g., as shown in Figure 18).

Superimposing bias voltage at different levels has induced very similar effects in the impedance behaviours (as observed in Figure 19), which also exhibit two semi-circular arcs corresponding to the amorphous matrix and the free carbon phase, with the former showed significant diminishing features as bias level rose and negligible influence on the free carbon phase. Such features again indicate significant contribution from the interfacial polarisation to the amorphous matrix phase (represented by the low-frequency semi-arc).[116,172] The spectra were

analysed by curve-fitting them with the modified-Debye equivalent circuit (the same as shown in the inset in Figure 19). Comparable trends in the changes in the resistance and capacitance of the amorphous matrix and free carbon phases were observed across all samples under similar measurement conditions as discussed in Section 3.3.2. Similar to that discussed above, the contribution from the internal barriers accounts for the larger capacitance of the amorphous matrix.

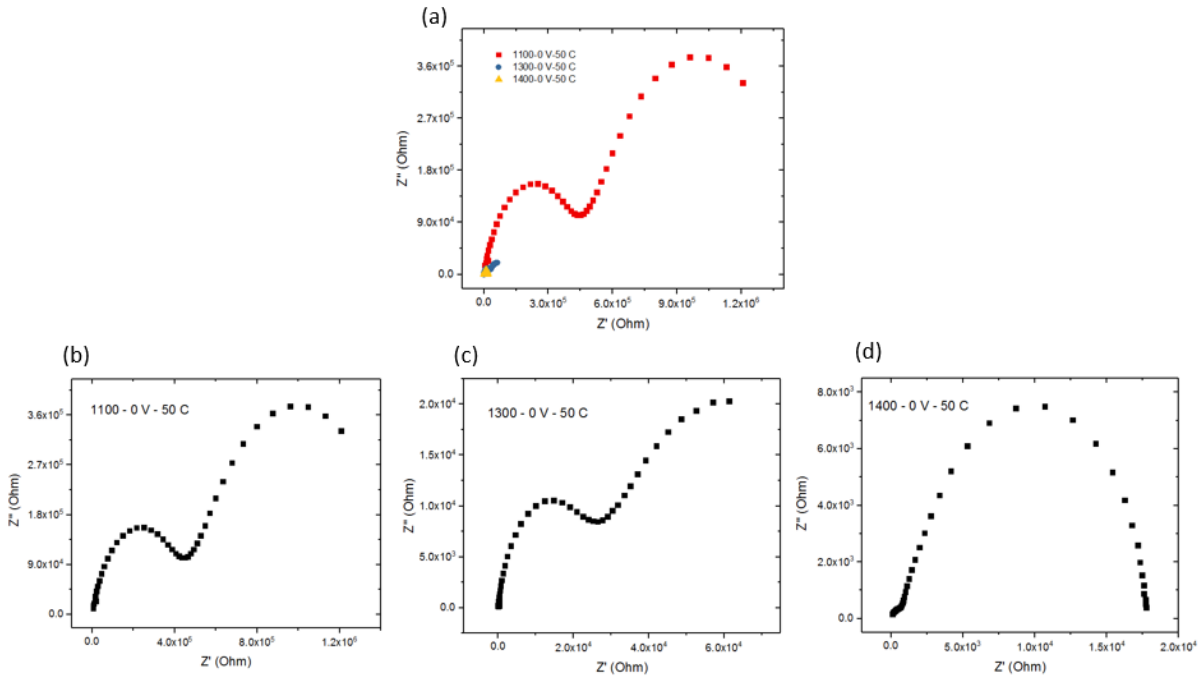

Figure 23 Influence of annealing temperature on the complex impedance of the *a*-SiAlCN ceramics, under 50 ℃ without dc bias voltage. Combined plots of different annealing temperatures are shown in (a) in the same scale, and the individual plots corresponding to 1100 ℃, 1300 ℃ and 1400 ℃ are shown in (b), (c), and (d) respectively.

The double Schottky barrier model (as discussed in detail in Section 3.3.2) was similarly applied to describe the bias dependent interfacial capacitance to account for the influence of annealing temperature. Good linear fitting trend was observed in the modified capacitance

$((\frac{1}{C} - \frac{1}{2C_o})^2)$ versus bias voltage (V) plots, similar to that shown in Figure 20. The charge carrier concentration and the potential barrier height of the *a*-SiAlCN are estimated from the intercept and the slope of fitting lines for samples obtained under different annealing temperatures. Figure 24 shows the annealing temperature dependence of the charge-carrier concentration and the potential barrier height, with both parameters increase with elevated annealing temperature.

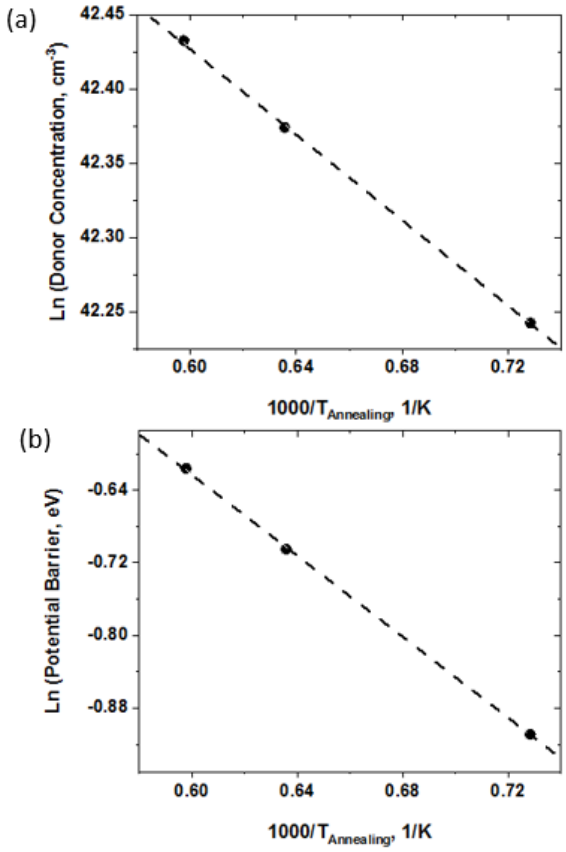

Figure 24 The influence of annealing temperature on the charge-carrier concentration (a) and potential barrier (b).

Such phenomena are also correlated to the heterogeneous structure of the *a*-SiAlCN (i.e., biphasic material comprised of a free carbon phase and an amorphous ceramic matrix phase possessing significantly different conductivities). As discussed above, double (back-to-back)

Schottky barriers are created at the interfaces between *n*-type free carbon clusters, since the gaps between Fermi energy and band tail are different for the amorphous Si-based ceramics and the free carbon phases (Figure 22).[161,176]

Previous studies have suggested that in the free carbon phase, an increased amount of C-dangling bonds would lead to the increase in charge carrier concentration with rising annealing temperature (Figure 24a).[158,169] As discussed above, a defect band is formed within the band gap, with the defects are predominantly the C-dangling bonds, which act as donors to provide electrons. Previous studies have revealed that the concentration of the C-dangling bonds increases with increasing annealing temperature.[169,183] Therefore, the increase in C-dangling bonds leads to an increase in the density of the defect states, resulting in more defects, leading to more charge carriers, thus higher donor concentrations with increasing annealing temperature.

With respect to the increase of potential barrier height with increasing annealing temperature (Figure 24b), it can be understood as follows considering the changes in the respective Fermi levels in the free carbon and amorphous matrix phases. It has been revealed that C-dangling bonds are present as defects in the free carbon phase, and also within the bulk of the amorphous ceramic network,[169] with the free carbon contains much more defects than the amorphous matrix (i.e., higher defect concentration).[115] In addition, investigations have shown that the concentration of the C-dangling bonds increases with increasing annealing temperature, leading to an increase in the density of the defect states.[179,184] Therefore, due to the increase in annealing temperature, both the free carbon and the amorphous matrix witness higher levels of active dopants (dangling defects) concentrations, which lead to an increased Fermi level in both phases, both moving towards the band tail, which is consistent with previous reports.[179]

However, the two phases experience different degrees of the Fermi level increase: the free carbon would witness a more significant rise, because of the higher defect concentration compared to that of the amorphous matrix. Such variation in the magnitudes of Fermi level rise in the two phases would therefore result in an enlarged difference between the Fermi energy in the free carbon and amorphous matrix phases, which leads to the increase in the potential barrier height.

3.4 Conclusions

The complex impedance spectra of the polymer-derived *a*-SiAlCN were measured under various dc bias voltages in a temperature range between 50 and 150 °C, on the samples annealed at different temperatures (1100-1400 ℃). All spectra, regardless of temperature and bias, consist of two semi-circular arcs, corresponding to the free-carbon phase and the interface, respectively. The impedance of the free-carbon phase is independent of the bias, while that of the interface decreased significantly with increasing dc bias. It is shown that the change of the interfacial capacitance with the bias can be explained using the double Schottky barrier model. The charge-carrier concentration and potential barrier height were estimated by comparing the experimental data and the model. The results revealed that increasing testing temperature led to an increased charge-carrier concentration and a reduced barrier height, both following Arrhenius dependence, whereas the increase in annealing temperature resulted in increased charge-carrier concentration and barrier height. The phenomena were explained in terms of the unique bi-phasic microstructures of the material.

CHAPTER 4: FEW LAYER 2D MOS_2 MEMBRANES OF NEAR ATOMIC THICKNESS FOR HIGH EFFICIENCY WATER DESALINATION[2]

4.1 Introduction

The availability of freshwater resources has decreased with increasing potable, agricultural, and industrial water demands around the globe for the past decades.[5] This global challenge, along with the adversely accelerating climate change, has been calling for immediate solutions for meeting the demands. Apart from the conservation of existing water resources, increasing the freshwater supply is deemed as a more sustainable and direct solution.[6] Since seawater is readily accessible and abundant, various thermal and physical desalination technologies have been utilised worldwide to produce drinking water by removing dissolved salts and other minerals from saline water. While multi-stage flash (MSF), multi-effect distillation (MED), and reverse osmosis (RO) are the most widely used desalination technologies, RO membrane is gaining market share at a faster pace.[7,8] RO is a high-pressure membrane process that utilises a semi-permeable polymeric membrane to retain salts and low-molecular-weight solutes while allowing the passage of water via diffusion. Despite the operational simplicity, RO membranes suffer from several technical limitations including low conversion efficiency, membrane fouling, and energy demand to pressurise the feedwater.[9,10] Accordingly, developing high-performance membrane materials with improved water recovery without compromising the solute rejection remains a compelling demand.

[2] Part of contents in this Chapter contains published works adapted with permission from: Hao Li, Tae-Jun Ko, Myeongsang Lee, Hee-Suk Chung, Sang Sub Han, Kyu Hwan Oh, Anwar Sadmani, Hyeran Kang, and Yeonwoong Jung. Experimental Realization of Few Layer 2D MoS_2 Membranes of Near Atomic Thickness for High Efficiency Water Desalination. *Nano Letters* **19**, 5194−5204 (2019). Copyright 2019 American Chemical Society. Published on July 1st 2019. Hao Li co-conceived the project, prepared the membrane materials and characterized them, performed the desalination tests, and analyzed the data.

A potentially promising solution stands with engineering the structure of traditional materials into tailored porosity or exploring a new type of intrinsically porous nanomaterials-based membranes. Recently developed two-dimensional (2D) materials present unprecedented opportunities for water desalination and molecular sieving technologies owing to their structural uniqueness.[11-13] Their extremely small thickness (i.e., a few Å for 2D monolayers) projects superior water permeation rates benefiting from small diffusion lengths for molecular transports while their high mechanical flexibility renders advantages for membrane integrations. Moreover, 2D materials produced by chemical synthetic routes possess high-density "intrinsic" structural imperfections (e.g., near atomic vacancies) whose physical dimensions are comparable to those of salt ions and water molecules.[14] In this endeavour, a variety of 2D materials have been explored including graphene,[15-18] dichalcogenides,[19-22] and graphene oxides,[23-26] along with substantive efforts for the structural engineering of traditional membrane materials such as zeolites,[27-30] and metal-organic frameworks [31-34]. Amongst them, 2D molybdenum disulfide (MoS_2) layers have recently gained significant interests for a wide range of water and environmental technologies. They not only share the intrinsic structural advantages inherent to other 2D materials but also present additional suitability such as excellent chemical stability and non-toxicity.[35-37] Furthermore, a variety of structural variations such as point defects, grain boundaries, and van der Waals (vdW) gaps have been ubiquitously observed in 2D MoS_2 layers grown via chemical vapour deposition (CVD) process.[38-40] Such "intrinsically" present structural imperfections of very high concentration (e.g., areal density of ~10^{13} cm^{-2} for sulphur vacancies[41]) offer 2D MoS_2 layers high promise as an efficient membrane material for water desalination applications. In fact, several studies based on theoretical calculations and molecular dynamics simulations have predicted superior desalination performances of monolayer 2D MoS_2.[14,19,41,152,153] Heiranian *et al*. have predicted

that 2D MoS_2 monolayers of enriched defective sites can exhibit ~2-5 orders-of-magnitude higher water fluxes than traditional filtration membranes, which is even 70% greater than the performance of graphene nanopores.[154] Köhler *et al*. have projected that the ion rejection capability of 2D MoS_2 membranes is superior to graphene under a wide range of test conditions including pressure, nanopore size, and cation valences.[152] Li *et al.* have simulated the desalination performance of 2D MoS_2 layers, demonstrating high water transport rate (355.3 L m^{-2} h^{-1} bar^{-1}) and excellent salt rejection capability.[155] Despite the theoretically-projected promise of 2D MoS_2 layers, their experimental utilisation for membrane-based desalination technologies has been rarely approached. A few experimental studies have explored MoS_2 laminar membranes of very large thickness (typically, ~1-10 μm) constituting mechanically stacked individual 2D flakes.[14] Sun *et al*. studied ~1.7 μm thick MoS_2 membrane films prepared via chemical exfoliation and subsequent filtration of aqueous dispersion.[156] Hirunpinyopas *et al.* demonstrated chemically functionalized ~5 μm thick laminar membranes composed of exfoliated 2D MoS_2 flakes employing the similar filtration process.[157] These laminar 2D MoS_2 membranes of large thickness have exhibited significantly limited desalination efficiencies, failing in meriting the structural uniqueness and performance advantages projected with near atom-thick membranes. For example, their water permeation rates were experimentally identified to be in a range of ~245-275 L m^{-2} h^{-1} bar^{-1},[156,157] significantly falling short of theoretical values predicted by simulation studies.[154] Moreover, ion rejection rates of mere ~15-30% were reported for pristine laminar 2D MoS_2 membranes of ~1-5 μm thickness.[157] Scarcity of experimental studies on the 2D MoS_2 layers-based membranes of near atomic thickness for water desalination is attributed to technical difficulties associated with integrating 2D layers preserving their structural integrity. Particularly, it has been challenging to produce

large-scale (> cm^2) "continuous" 2D MoS_2 layers of ~1-10 nm thickness and their seamless integration onto porous substrates, hindering their applications to desalination technologies.

In this Chapter, we discuss the experimental realisation of high-efficiency water desalination enabled by ultra-thin 2D MoS_2 layers-based membranes. We demonstrate the integration of centimetre-scale CVD-grown 2D MoS_2 layers of only ~7 nm thickness onto porous polymeric substrates and studied their desalination performances. This new type of near atom thick-membranes exhibits an excellent combination of high water permeability approaching theoretically predicated values and superior ionic sieving performance for various seawater salts. Fundamental mechanisms responsible for the observed high desalination efficiency are also discussed.

4.2 Experimental Method

CVD growth of 2D MoS_2 layers: Very thin films of Mo (typically, ~2-2.5 nm thickness) were deposited onto SiO_2/Si substrates via electron beam evapouration to ensure the growth of horizontally-oriented 2D MoS_2 layers avoiding their unwanted vertical alignment.[185-187] As-deposited Mo-SiO_2/Si samples were then placed inside a 1 inch quartz tube located in the middle of a horizontal tube furnace (Lindberg Blue M, ThermoScientific). Subsequently, sulphur powders (99.5%, Sigma-Aldrich, St. Louis, MO) were loaded within the quartz tube at the furnace upstream side. The furnace was pumped down to a base pressure of 5 mTorr following purging with high-purity argon (Ar) gas. It was then ramped up to 780 ℃ and was held for 50 mins at a ramping rate of 15 ℃/min under a constant flow of Ar gas (100 SCCM). After the reaction, the furnace was naturally cooled down to room temperature under Ar supply.

Water permeation rate measurement: A typical external pressure method was used to assess the water permeation rate by employing a common dead-end filtration setup. The sandwiched membrane containing 2D MoS_2 layers was placed inside a leak-free syringe filter holder. The water permeation rate was calculated by weighing the volume of water passing through the 2D MoS_2/PES membrane area under a constant pressure of 1 bar as a function of time.

Salt ion rejection rate measurement: A conductivity probe (ThermoScientific, model: Orion 013605MD) connected to a solute conductivity meter (ThermoScientific, model: Orion 5 Star) was used to monitor conductivities in respective containers. The probe was thoroughly rinsed each time before each measurement. The salt rejection rate was calculated by $\left(1-\frac{C_P}{C_F}\right)\times 100\%$, where C_P and C_F are the conductivity of the permeate and feed side, respectively. Seawater salts of NaCl (99%, Sigma-Aldrich, St. Louis, MO), KCl (99%, Sigma-Aldrich, St. Louis, MO), $MgCl_2$ (98%, Sigma-Aldrich, St. Louis, MO), and $CaCl_2$ (93%, Sigma-Aldrich, St. Louis, MO) of various concentrations were employed for rejection rates measurements. Each measurement was repeated for three times to improve consistency and averaged values are presented.

TEM/STEM characterisation: The crystalline structure of 2D MoS_2 layers was characterised using a JEOL ARM200F FEG-TEM/STEM with a Cs-corrector. Plane-view TEM samples were prepared by delaminating the 2D MoS_2 layers from SiO_2/Si substrates inside water and by transferring them to holey carbon TEM grids. Cross-sectional TEM samples were prepared by focused ion beam (FIB)-based milling and lift-out techniques. As-grown 2D MoS_2 layers-SiO_2/Si substrates were coated with a carbon film of ~100 nm thickness and were subsequently cross-sectioned inside a FIB (Quanta 2D FEG, FEI). Ga ion milling (30 keV) was executed until the target area became electron transparent and the prepared

specimen was transferred to a TEM grid using a micromanipulator (Omniprobe). All TEM operations were performed at an accelerating voltage of 200 kV.

AFM characterisation: Topography images and height profiles of the 2D MoS_2 layers integrated on PES supporters were obtained with AFM (nanoIR2 by Anasys Instruments, Santa Barbara, CA) operated in a tapping mode at a scan rate of 1 Hz. AFM probes (PR-EX-T125-10, Anasys Instruments) with a nominal spring constant of 30 N/m were employed.

MD simulation: MD simulations were performed using a large-scale atomic/molecular massively parallel simulator (LAMMPS) package[188] in a similar way to a recent computational study.[154] We generated a 2D MoS_2 layer (4.1×3.5 nm^2) with a nanopore (1.6 nm in diameter) and applied a constant pressure (250 atm) to the graphene piston using VMD 1.9.1.[189] The simulation system is $6.0 \times 5.6 \times 11.5$ nm^3 in size containing ~6,600 atoms. Lennard-Jones (LJ) parameters for 2D MoS_2 layer,[154] graphene sheet,[190] and NaCl [191] were obtained from previous studies. The mixing rule was applied to obtain the remaining LJ parameters following the recent computational study.[154] Specifically, TIP3P water model[192,193] and SHAKE algorithm were employed to maintain water molecules in rigid states. The cut-off distance for LJ was set to 10 Å and long-range electrostatic interactions were calculated using the Ewald method.[194]

4.3 Results and Discussion

4.3.1 2D MoS_2 Layers Membrane Preparations and Characterisations

Centimetre-scale 2D MoS_2 layers were grown by the modified CVD process developed in our lab.[195-197] A thin film of Mo (typically, ~2-2.5 nm thickness) was deposited onto a SiO_2/Si substrate via electron beam evapouration. The as-deposited Mo-SiO_2/Si sample was thermally sulphurised inside a CVD chamber under the controlled flow of vapourised sulphur (S), which

yields the conversion of Mo to 2D MoS_2 layers. Detailed conditions for 2D MoS_2 layers growth are described in *Method* section. After the CVD reaction, as-prepared 2D MoS_2-SiO_2/Si sample was gently immersed into de-ionised water until the 2D MoS_2 layers were spontaneously delaminated. The separated 2D MoS_2 layers floating on the water surface were then gently scooped up with a polyethersulfone (PES) membrane substrate (~0.03 μm pore size and ~100 μm thickness; commercial products from Sterlitech, Kent, WA). Note that PES has been extensively employed as a substrate for conventional desalination[198] as well as 2D materials-based membranes.[199] Following the integration of 2D MoS_2 layers on PES, a thin film of polydimethylsiloxane (PDMS) was selectively deposited on the 2D MoS_2/PES surface leaving a small opened area which is to function as a membrane directly exposed to water. Figure 25(a) illustrates the membrane preparation procedure, from the large-area CVD growth of 2D MoS_2 layers and their integration onto PES substrate as well as selective PDMS sealing. Given that the porosity of PES substrates is much larger than the intrinsic near-atomic vacancies inherent to 2D MoS_2 layers (to be verified in the later section), water permeation and ionic sieving are exclusively determined by 2D MoS_2 layers which are the integral part of the membrane. Prior to the integration of 2D MoS_2 layers, the PES surface can be treated with oxygen plasma to ensure the uniform adhesion of large-area 2D MoS_2 layers to it. Figure 25(b) demonstrates the water-assisted delamination of 2D MoS_2 layers from a SiO_2/Si growth substrate, revealing that only 2D MoS_2 layers become spontaneously detached upon immersion in water. The success of this facile 2D layer separation is attributed to the combined effect of the high surface energy contrast between 2D MoS_2 basal planes and SiO_2 surface as well as the weak vdW molecular attraction in between them as clarified in our previous reports.[200]

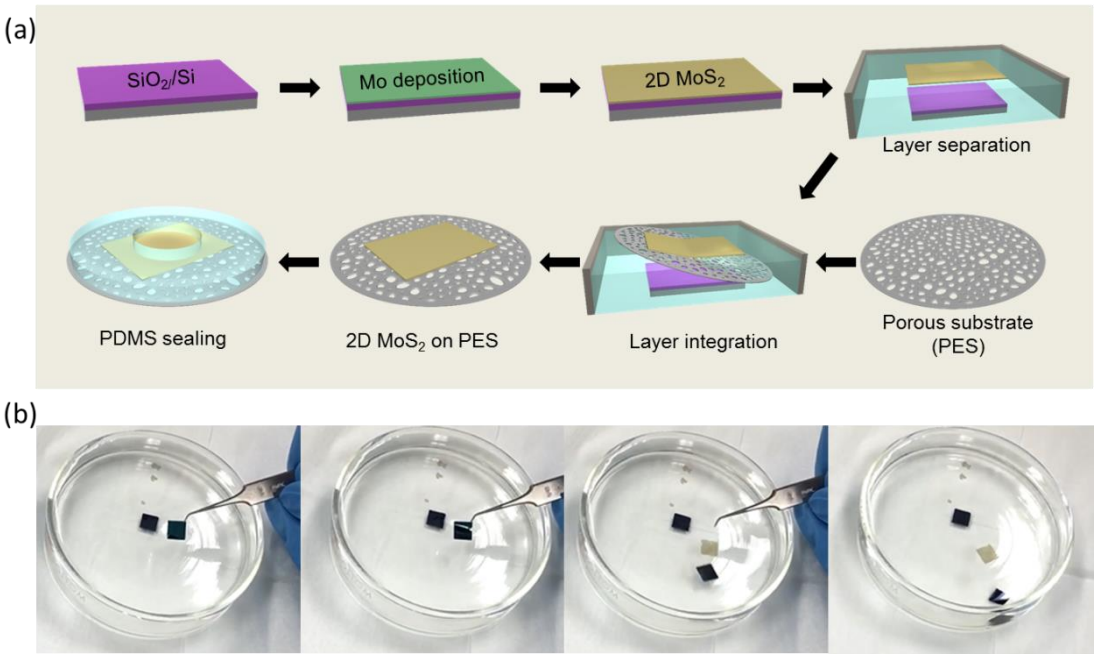

Figure 25 (a) Schematic procedures for few-layer 2D MoS_2 membranes preparation, transfer, and integration. (b) Sequential images showing the detachment process of 2D MoS_2 layers from a SiO_2/Si substrate upon water immersion.

Prior to investigating the water permeation and ion rejection capability of 2D MoS_2 layers integrated on PES substrates, we first verified the material quality of CVD-grown 2D MoS_2 layers in their as-grown state. Figure 26(a) shows an image of 2D MoS_2 layers grown on a SiO_2/Si substrate of > 2 cm^2 in size. The chemical and structural integrity of the as-grown 2D MoS_2 layers were characterised via Raman spectroscopy and transmission electron microscopy (TEM). Figure 26(b) presents a typical Raman spectrum of the CVD-grown 2D MoS_2 layers revealing two distinctive peaks. The peak positions correspond to the in-plane (E^1_{2g}) and out-of-plane (A_{1g}) vibration modes of 2D MoS_2 layers, confirming their presence on the growth substrate.[185,201,202] Figure 26(c) shows a TEM image of the same sample in Figure 26(a) in a cross-sectional view, revealing the presence of continuous 2D MoS_2 layers of uniform thickness. Figure 26(d) shows an enlarged view of the red box in Figure 26(c), revealing the

crystalline structure of 2D MoS_2 layers. The image clarifies that they are composed of horizontally-oriented individual layers of uniform ~7 nm thickness. Moreover, the individual 2D layers are separated by the physical gaps formed by vdW interaction with an average interlayer spacing of ~0.65 nm. Figure 26(e) illustrates the atomic schematics of the 2D MoS_2 layers corresponding to the red box in Figure 26(d). Although the vdW gap denotes the interlayer spacing corresponding to Mo-to-Mo distance across adjacent 2D layers, the actual "physical gap" which serves as a transport channel for molecular diffusion in this case should be close to ~0.3 nm determined by the interlayer S-to-S distance. Note that the dimension of this transport channel is larger than that of a single water molecule, i.e., ~0.275 nm in a diagonal length.[203] Figure 26(f) shows a plane-view high-resolution TEM (HRTEM) image of the horizontally-oriented 2D MoS_2 layers. The image clearly reveals the Moiré fringes of hexagonal MoS_2 basal planes, reflecting the crystallographic stacking of mis-oriented individual 2D layer grain as well as indicating the presence of grain boundaries.[195] These comprehensive characterisation results conclude that our CVD-grown 2D MoS_2 layers possess high spatial continuity and uniform thickness (~7 nm in Figure 26(c), (d)) while containing a large degree of intrinsic structural porosity (e.g., ~0.65 nm vdW gaps). Such combined attributes of macroscopic structural homogeneity and near atomic scale heterogeneity render the CVD-grown 2D MoS_2 layers high suitability as desalination membranes, as verified below.

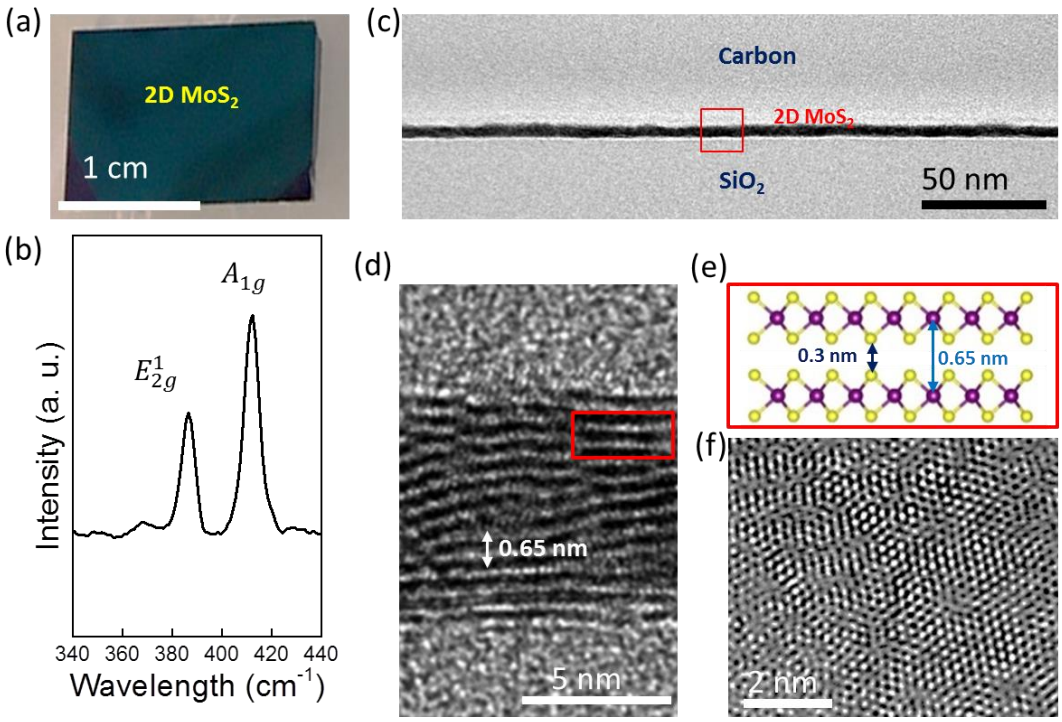

Figure 26 (a) Optical image of as-grown 2D MoS_2 layers on a SiO_2/Si substrate. (b) Raman spectrum of the corresponding CVD-grown 2D MoS_2 layers. (c) TEM image of the same sample in Figure 26(a) in a cross-sectional view. (d) Enlarged view of the red box in Figure 26(c). (e) Atomic schematics of the few-layer 2D MoS_2 corresponding to the red box in Figure 26(d). (f) Plane-view HRTEM image of horizontally-oriented 2D MoS_2 layers showing Moiré fringes.

Having identified the intrinsic structural suitability of the CVD-grown 2D MoS_2 layers for desalination applications, we then characterised the morphologies of 2D MoS_2 layers integrated on PES supporting substrates. As depicted in Figure 25(a), complete membranes are in a configuration such that the 2D MoS_2 layers are selectively covered by an impermeable PDMS film, which defines a specific region for water penetration by sealing the surrounding surface. Figure 27(a) illustrates a schematic set-up for water permeation measurements. The 2D MoS_2 layers-integrated PES substrate was covered with another bare PES substrate on the back side.

It was subsequently sandwiched in between two PDMS sealing films defining a membrane area of ~5 mm on the centre region. Note that this sandwich-like assembly has been extensively employed in configuring nanomaterials-based membranes including 2D materials of large thickness (> 1 μm).[157] This layered membrane was then loaded inside a syringe filter holder in a typical dead-end filtration setup. The water permeation rate was then measured via an external pressure method by weighing the volume of water passing through the membrane area (i.e., ~5 mm central hole composed of 2D MoS_2/PES only) as a function of time under a constant pressure. Details are presented in the *Method* section. Figure 27(b) shows a representative image of a 2D MoS_2 layers-integrated PES supporter achieved following the procedures in Figure 25(a). On top of the sample surface, PDMS was selectively deposited (denoted by yellow false colour) leaving an open membrane hole at the center while sealing the surrounding area. The morphology of the 2D MoS_2 layers integrated on PES was characterised by atomic force microscopy (AFM) and Raman spectroscopy. Figure 27(c) shows an AFM topography image of 2D MoS_2 layers whose thickness was determined by obtaining the height profile across their interface with PES (denoted by the yellow line). Figure 27(d) shows the corresponding AFM height profile revealing that the integrated 2D MoS_2 layers are ~7 nm thick which corresponds to ~10-11 layers given the interlayer spacing of ~0.65 nm.[204,205] The result is quite consistent with the TEM characterisation (Figure 26(d)) obtained from the sample in a pristine state before integration onto PES, indicating the high fidelity of our 2D layer integration process. Figure 27(e) shows a Raman profile of the 2D MoS_2 layers on PES, revealing two characteristic peaks of E_{2g}^1 and A_{1g} vibration modes consistent with the observation prior to their separation and integration (Figure 26(b)). This analysis confirms that the 2D MoS_2 layers integrated on PES maintain their original structural and chemical integrity, which were not altered through the membrane preparation procedures.

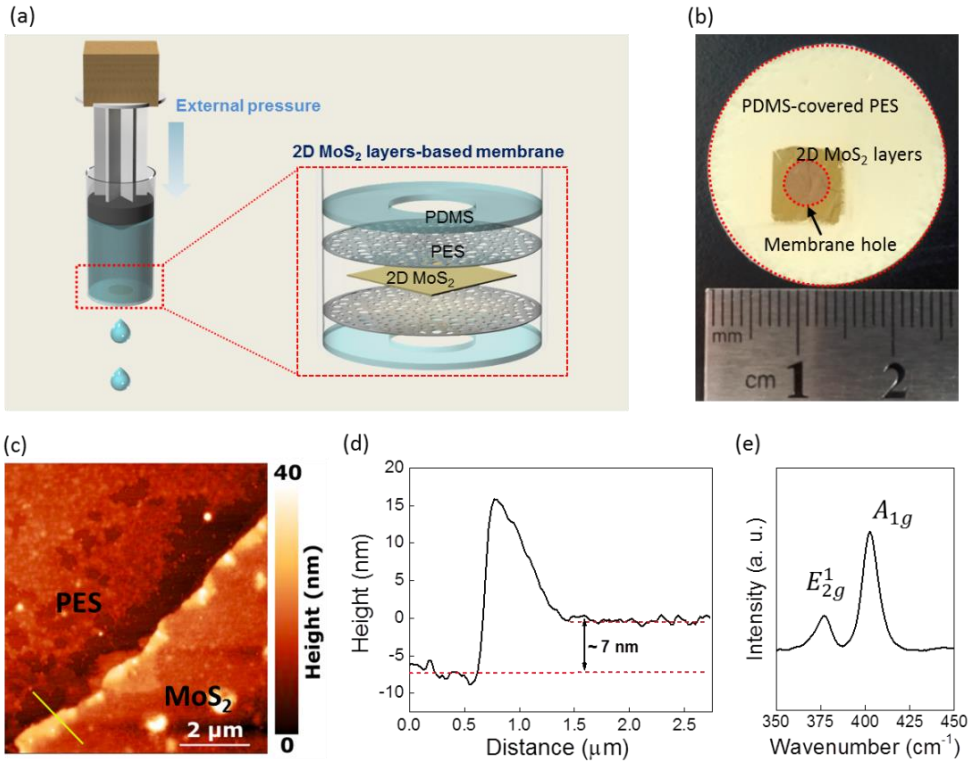

Figure 27 (a) Schematic set-up for water permeation measurement. (b) Representative image of a 2D MoS_2 layers-integrated PES supporter with PDMS sealing. 2D MoS_2 layers-membrane hole is denoted by the inner dotted circle. (c) AFM topography image of a 2D MoS_2 layers/PES interface. (d) AFM height profile corresponding to the yellow line in Figure 27(c). (e) Raman spectrum profile obtained from 2D MoS_2 layers integrated on a PES supporter.

4.3.2 Desalination Performances Evaluations and Comparisons

Desalination efficacies of 2D MoS_2 layers on PES supporters were investigated by measuring their water permeation and salt ion rejection rates. The water permeation rate was determined via the external pressure method employing the equipment described in Figure 27(a). Figure 28(a) compares the water permeation rates of bare PES vs. 2D MoS_2 layers (~7 nm thick) integrated on PES, revealing the exclusive role of 2D MoS_2 layers on controlling the

permeability of water molecules. The bare PES substrate exhibits a high water flux of 2735 (± 139) L m^{-2} h^{-1} bar^{-1}, reflecting its intrinsic porosity of large size and high density (~0.03 μm pore size). Integrating 2D MoS_2 layers suppresses the permeability to 322 (± 27.2) L m^{-2} h^{-1} bar^{-1} owing to their intrinsic porosity of much smaller dimension - typically, atomic vacancies of ~1-1.5 nm in size which is to be verified in the later section. It is noteworthy that this permeability value achieved with ~7 nm thick 2D MoS_2 layers is significantly larger (up to > 30%) than those realised with the 2D MoS_2 laminar membranes of ~1-10 μm thickness,[156,157] indicating their suitability for desalination. Such micrometer-thick 2D MoS_2 laminar membranes have been developed by mechanically stacking up individual 2D flakes dispersed in aqueous solvents using filtration processes. Owing to the nature of high pressure-demanding methods in their preparation, the assembled 2D laminar MoS_2 layers often tend to exhibit uncontrolled physical gaps in between constituent layers.[199,206,207] For example, an interlayer spacing of ~0.3 nm has been reported,[199] which is much smaller than the intrinsic vdW gap distance of ~0.65 nm observed with our CVD-grown 2D MoS_2 layers (Figure 26(d), (e)). Accordingly, the transport of water molecules in between 2D layers becomes interfered, resulting in lower water permeation rates given the diameter of a single water molecule is ~0.275 nm.[203] Moreover, the 2D MoS_2 laminar membranes assembled by the high-pressure liquid filtration processes exhibit significantly larger thickness of ~1-10 μm compared to our CVD-2D MoS_2 layers, which further contributes to slowing down the transport kinetics of water molecules. The proficiency of our CVD-2D MoS_2 layers on PES supports for rejecting a variety of salt ions was determined using a measurement set-up whose schematic is presented in Figure 28(b). A custom-built apparatus composed of a pair of one-litre water containers and a conductivity probe was assembled with a leakage-proof pathway. The sandwiched membrane containing 2D MoS_2 layers was then placed inside the water pathway which allows for the

access of ions only through the 2D MoS_2 layers-membrane hole. The container at the permeate side was filled with pure de-ionised water while the feed side maintained an equal volume of de-ionised water mixed with salt ions to be tested. Measurements were carried out at room temperature under continuous stirring of a magnet in the feed container to minimise the concentration gradient of test salt ions. We have quantified the movement of ions by employing the conductivity measurement method well established in the field;[157] i.e., the salt rejection rate was calculated by $\left(1-\frac{C_P}{C_F}\right)\times 100\%$, where C_P and C_F are the conductivity of the permeate and feed side, respectively.[208] Measurement conditions are detailed in the *Method* section. Various seawater salts of diverse concentrations were tested: (1) sodium chloride (NaCl) of 0.6 M (equivalent to seawater salinity concentration[209]), (2) NaCl of 0.469 M (typical seawater Na^+ concentration[210]), (3) potassium chloride (KCl) of 0.1 M, (4) magnesium chloride ($MgCl_2$) of 0.1 M, and (5) calcium chloride ($CaCl_2$) of 0.1 M. The concentration of 0.1 M for KCl, $MgCl_2$ and $CaCl_2$ was selected for measurements consistency although the typical seawater concentrations of K^+, Mg^{2+} and Ca^{2+} are below 0.1 M.[210,211] Figure 28(c) presents the plots of seawater ion rejection rates obtained at identical interval times during the course of three hours. Remarkably, the 2D MoS_2 layers-integrated membrane exhibits very high salt rejection capability (> 99.5%) for all the tested species at their respective concentrations. Moreover, the durability of the membrane in retaining desalination capability was evaluated by using 0.1 M NaCl solute as a testing agent over a continuous time period of > 24 hours. Figure 28(d) confirms the superior performance of the 2D MoS_2 layers-integrated membrane which retains ~ 98.3% rejection rate even after 24 hours. Apart from the rejection rate tests with single-ionic solutions, two different types of seawater containing multiple ions were employed to further assess the desalination efficacies of our CVD-2D MoS_2 layers. One was actual seawater obtained from the Atlantic coast and the other was synthetic seawater prepared to mimic the

concentrations of typical ion species present in standard seawater, i.e., Na^+ of 0.469 mol/L [210], K^+ of 0.01 mol/L [210], Mg^{2+} of 0.0528 mol/L [210], and Ca^{2+} of 0.01 mol/L [210]. Figure 28(e) presents salt rejection rates for both cases, confirming the excellent desalination capability of near 100% rejection rates. It is noteworthy that the overall desalination efficiencies of our CVD grown-2D MoS_2 layers of ~7 nm thickness are significantly higher than those of previously developed micrometre-thick 2D MoS_2 laminar membranes assembled via liquid filtration processes.[157] Detailed comparisons will be presented in the later section. Figure 28(f) presents pressure-dependent rejection rates for various salt ions of diverse concentrations. The plots reveal a slight decrease of the rejection rates with increasing applied pressure which exerts higher mechanical forces causing more ion translocation events, consistent with numerical predictions with monolayer 2D MoS_2.[154] Moreover, the high rejection rate of > 98.5 % is well retained for all salt ions irrespective of applied pressure within the tested range. We believe that the superior salt rejection performance observed with our CVD-2D MoS_2 layers is attributed to their ionic sieving capability owing to the intrinsically present vdW gaps of uniform spacing (Figure 26(e)). Meanwhile, the micrometer-thick 2D MoS_2 laminar membranes inevitably contain a high density of uncontrolled physical gaps in between the edges of adjoining 2D flakes owing to the intrinsic randomness associated with stacking them up in solutions. Discussion will follow in the later section of this Chapter.

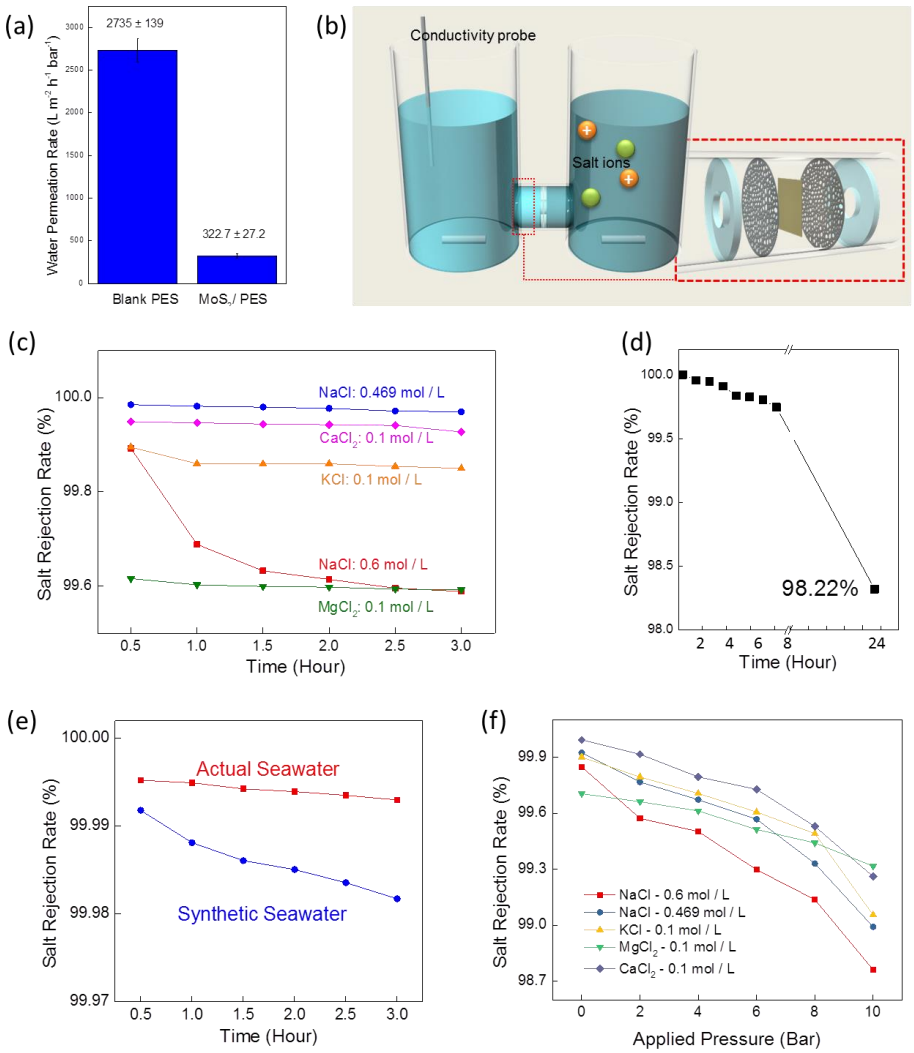

Figure 28 (a) Comparison of water permeation rates for 2D MoS_2 layers/PES vs. bare PES. (b) Schematics of salt rejection rates measurement set-up. (c) Time-dependent rejection rates for typical seawater salt ions of various species. (d) Rejection rate for 0.1 M NaCl over a continuous 24-hour period. (e) Salt rejection performances of 2D MoS_2 layers tested with actual and synthetic seawater. (f) Pressure-dependent rejection rates for various salt ions.

We compare the desalination performances of our CVD-2D MoS_2 layers with previously developed thin membrane materials. Figure 29(a) presents comparisons with a variety of systems ranging from conventional porous membrane materials to recently developed

nanostructured materials. The materials include MFI zeolite,[212] seawater reduced reverse osmosis (RO),[213] brackish RO,[213] nanofiltration,[213] high-flux RO,[213] polysulfone[214] as well as graphene oxide enhanced polyamide thin-film nanocomposite membrane (GO/PA),[215] and multi-walled carbon nanotubes incorporated polyamide (MWNTs-PA)[216] materials. The comparison plot is presented in terms of water permeability vs. salt rejection rate – two most decisive indicators for defining the performances of desalination membranes. This survey result reveals that our CVD-2D MoS_2 layers present an outstanding combination of high permeability and strong ionic sieving capability. Despite the similar ion rejection rates noted for many of the compared materials, our CVD-2D MoS_2 layers of extremely small (~7 nm) thickness exhibit orders-of-magnitude higher water permeability. We note that monolayer graphene membranes in recent experimental studies exhibit much higher water permeability than our CVD-2D MoS_2 layers, which must be attributed to their extremely small one-atom thickness.[217,218] However, it is worth mentioning that their areal dimensions are very limited, i.e., in a range of ~ 20 μm^2 [217] to ~10^4 μm^2 [218], much smaller than our "centimetre-scale" membrane areas. Moreover, the fabrication of these monolayer graphene membranes has relied on top-down lithographic patterning processes, much more complicated than our facile manual integration approach. Furthermore, we compare the desalination performances of the CVD-2D MoS_2 layers with previously developed 2D MoS_2 laminar membranes of micrometre thickness prepared via liquid exfoliation/filtration processes (Figure 29(b)). Compared to the traditional membrane materials (Figure 29(a)), we note that decently higher water permeability was achieved with these micrometre-thick 2D MoS_2 laminar membranes.[157] However, they significantly fall short of our CVD-2D MoS_2 layers of ~ 7 nm thickness in terms of ionic sieving capability. Particularly, pristine 2D MoS_2 laminar membranes of ~1-5 μm thickness exhibit ion rejection rates of only ~15-30%,[157] in a sharp contrast to the performance (i.e.,

rejection rate > 99%) achieved with our CVD-2D MoS_2 layers which were not even functionalised for further property improvement.

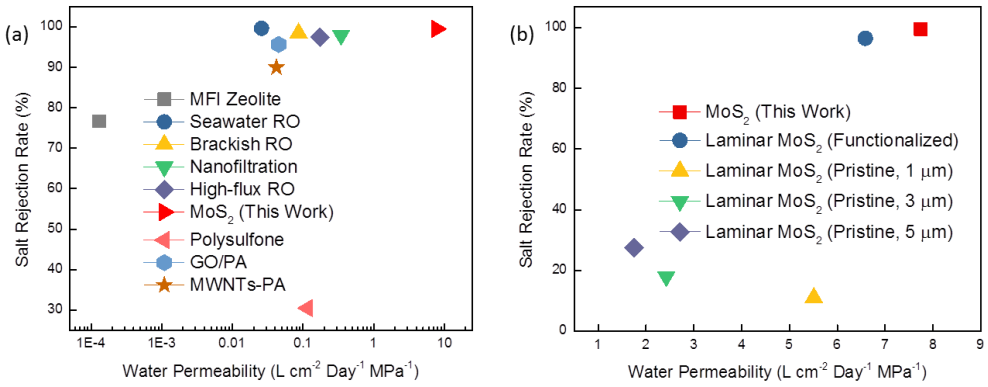

Figure 29 (a) Desalination performances of various membranes regarding salt rejection and water permeation rates. (b) Desalination performances of the CVD-2D MoS_2 layers of ~7 nm thickness developed in this study vs. 2D MoS_2 laminar membranes of micrometer thicknesses prepared via liquid exfoliation/filtration processes.

Due to the imperfect nature of CVD process optimisation, intrinsic structural variations such as atomic vacancies and grain boundaries have been regarded inevitably present in CVD-grown 2D MoS_2 layers.[38,40,199,219-221] For instance, various types of near atomic-scale vacancies have been identified to exist within CVD-grown 2D MoS_2 basal planes, including mono-sulphur vacancy (V_S), di-sulphur vacancy (V_{S2}), vacancy complex of Mo with three surrounding sulphur (V_{MoS3}), and vacancy complex of Mo with three surrounding pairs of di-sulphur (V_{MoS6}).[38] Water permeability achieved with CVD-2D MoS_2 layers can be understood by considering the dimensional effect of this intrinsic porosity as well as its areal density; i.e., the size of these vacancies should be large enough to allow for the facile translocation of water molecules and their areal density should be large to ensure high probability for the translocation event. Amongst the above listed vacancies, it has been known that sulphur vacancies of various

sizes yield a large areal density of up to ~10^{13} cm^{-2}, [41] rendering CVD-grown 2D MoS_2 layers sulphur-deficient in general.[220,222] However, it is known that the areal density of large-sized (~ 1 nm) intrinsic sulphur vacancies such as V_{MoS6} is much smaller than that of small-sized vacancies, e.g., V_S of < 0.3 nm.[220] This competing situation makes it difficult to experimentally quantify and identify the kind of specific vacancies which most govern water permeability. In addition to the intrinsic atomic vacancies within basal planes, CVD-grown 2D MoS_2 layers contain a large density of intrinsic "nanopores" present along the grain boundaries formed by individually stitching 2D grains of distinct crystallographic orientation. The size of these nanopores is larger than that of the atomic vacancies within basal planes as they are generally composed of multiple un-coordinated atoms. For instance, nanopores of ~0.6–0.82 nm^2 in size can be naturally formed by adjoining 2D layers in a binary stack while their size can further vary with grain boundary angles.[223,224] Accordingly, their role on governing water permeation and ion rejection must become pronounced as far as they are abundantly present within grain boundaries, which must be the case for our CVD-2D MoS_2 layers as verified in the next section. Indeed, theory predicts that nanopore sizes of ~0.74–0.98 nm would yield the optimal combination of high salt rejection rate and high water permeation flux for 2D MoS_2 layers.[41] In addition to the contributions from atomic vacancies and nanopores to water permeation, the uniformly spaced vdW gaps inherent to our CVD-2D MoS_2 layers (Figure 26(e)) are believed to play a significant role as well, particularly, for achieving high ionic sieving capability. In fact, the physical sizes of the hydrated ions tested in this experiment are identified to be larger than the interlayer vdW gap size of our horizontally-aligned 2D MoS_2 layers. The interlayer vdW gap which functions as a channel for molecular/ionic transport is ~0.65 nm wide accompanying the actual S-to-S distance of ~0.3 nm, as shown in Figure 26(d) and Figure 26(e). Meanwhile, diameters of the tested cations in their hydrated states are as follows: 0.66 nm (K^+),

0.72 nm (Na^+), and 0.86 nm (Mg^{2+}).[225,226] This observation suggests that the transportation of the hydrated ions through the vdW gap within our material is efficiently impeded, which well explains the observed high rejection rates. In addition to the above accounted dimensional/geometrical effect, electrostatic interaction of atomic vacancies is considered as another major factor for governing both water permeation and ionic sieving. Theory suggests that salt ions encounter significantly high energetic and steric barriers when approaching sulphur vacancies while water molecules are relatively unaffected.[155] For example, cations (e.g., Na^+) experience high Coulombic barrier since the sulphur vacancies are positively charged due to the surplus amount of un-bonded Mo atoms.[155] Moreover, these atomic vacancies expose hydrophilic Mo-rich sites which can readily attract water molecules allowing for their efficient permeation while impeding ion movements, yielding high water flux and ion rejection rates.[154, 227] Molecular dynamics (MD) simulation studies by Köhler *et al*. further justify this analysis, identifying that the water-accessible nanopores of up to ~1 nm present strong ion rejection capability even at a high pressure of 100 MPa.[152]

The proposed desalination mechanism based on the intrinsic nanopores and vdW gaps of CVD-2D MoS_2 layers is elucidated in Figure 30. The schematic in Figure 30(a) illustrates that the nanopores primarily present within the grain boundaries of poly-crystalline 2D MoS_2 layers allow for the efficient permeation of water molecules. The illustration in Figure 30(b) shows a cross-sectional view of water permeation and ion rejection events through the interlayer vdW gaps within horizontally-aligned multilayer 2D MoS_2. While water molecules easily translocate through the nanopores as well as transport within the interlayer vdW gaps, the transportation of hydrated ions is efficiently interfered owing to their relatively large sizes. Accordingly, high water fluxes and ion rejection rates should be resultant, as above experimentally verified. The presence of such nanopores localised within grain boundaries has

been directly verified by aberration-corrected TEM characterization. Figure 30(c)-Figure 30(g) present representative TEM images of the CVD 2D MoS_2 layers of ~ 7 nm thickness, highlighting their intrinsic structural imperfections. Figure 30(c) and Figure 30(d) reveal their typical poly-crystalline structure with ample crystalline grains and grain boundaries. The red arrows in Figure 30(c) denote the areas where multiple nanopores are observed, typically across the grain boundaries. Figure 30(d) shows one large (~ 1.5 nm) localised nanopore (blue dotted circle) observed in the area different from Figure 30(c). Figure 30(e)-Figure 30(g) present HRTEM images of localised grain boundaries and their detailed crystalline structures. Figure 30(e) reveals a large-sized (~ 2 nm) highly disordered region (red dotted circle) constituting multiple nanopores of various sizes on the interfacial junction formed by the grains of two distinct crystallographic orientations. Note that the yellow triangle and the green hexagon clarify two different Moiré fringes evidencing the distinct orientation of each grain. Figure 30(f) and Figure 30(g) present zoomed-in HRTEM images of individual nanopores on the grain boundaries of the same sample – areas different from Figure 30(e). The images clearly evidence the presence of multiple nanopores the size of which varies in a range of ~0.5 nm to ~ 1 nm (denoted by the yellow circles), suitable for the permeation of water molecules. Although it is experimentally challenging to precisely quantify the areal density of such vacancies in a statistical manner, their presence is strongly believed to be responsible for the overall desalination performances.

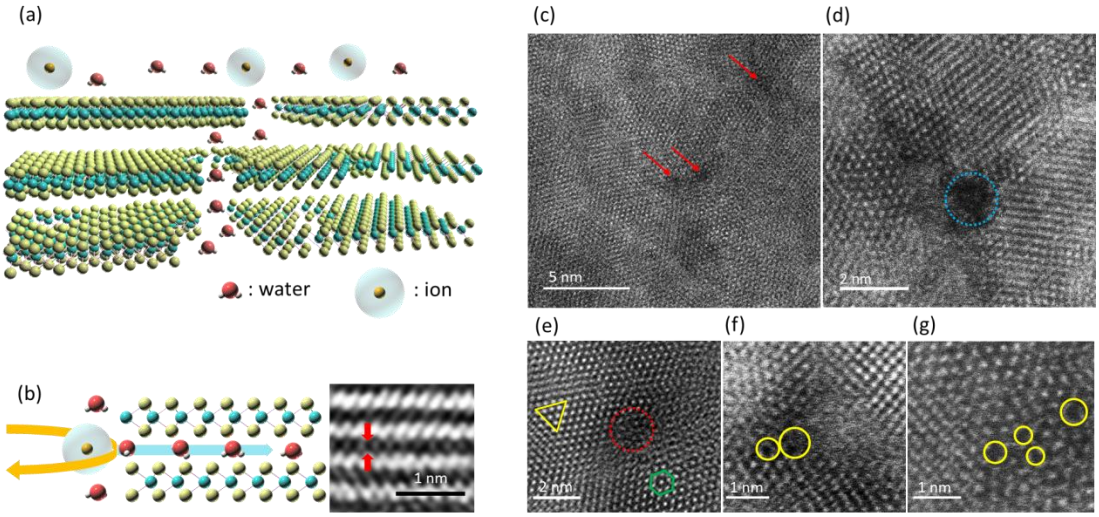

Figure 30 (a) Schematic illustration to visualize the translocation of water molecules through nanopores within the grain boundaries of horizontally-aligned multilayer 2D MoS_2. Note that the size of the nanopores is large enough to allow for water permeation. (b) Side-view illustration to show that water molecules easily transport through the interlayer vdW gaps while hydrated ions are efficiently rejected due to their larger sizes. The inset HRTEM image visualizes the vdW gap (red arrows) which functions as a water transporting channel. (c)-(g) TEM images to confirm the presence of intrinsic nanopores within the grain boundaries of CVD-2D MoS_2 layers revealing: (c) multiple nanopores, (d) a localized nanopore of ~1.5 nm in size, (e) distinct grain orientations, and (f)-(g) nanopores of various sizes.

Lastly, we further justify the exclusive role of nanopores within 2D MoS_2 layers on the experimentally observed water permeation and ionic sieving effects. We have carried out non-equilibrium molecular dynamics (MD) simulations and monitored the filtration of saline water through a 2D MoS_2 layer containing a near-atomic scale vacancy. A schematic of the simulation system is shown in Figure 31(a) which illustrates NaCl-containing saline water at the onset of a filtration process. A NaCl concentration of 0.6 M was chosen to mimic seawater salt concentration conditions. A graphene sheet placed on top of the saline water box acts as a

rigid piston and the permeation of water molecules is directly visualised using visual molecular dynamics (VMD) 1.9.1.[189] Upon the application of constant pressure to the piston, water molecules as well as Na^+ and Cl^- start to move toward the 2D MoS_2 layer. Figure 31(b) illustrates the time-lapse snapshot of this molecular and ionic movement at varying timeframes. It is apparent that a majority of water molecules facilely pass through the pore, which becomes more pronounced as the timeframe extends from 5 ps to 40 ps, while both Na^+ and Cl^- barely penetrate it. This MD simulation result well agrees with our experimental observation of high water permeability and ion rejection rates and is also consistent with the recent computational study.[154]

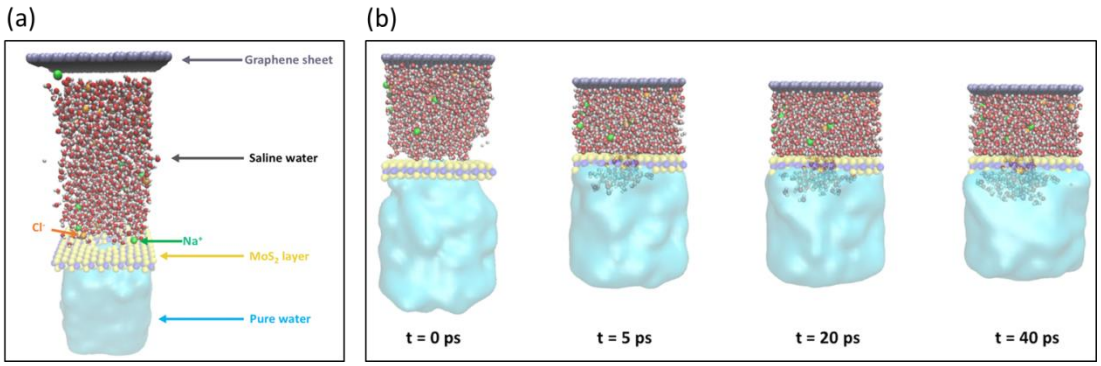

Figure 31 (a) Schematic of MD simulation system. Saline water is located between the graphene sheet which acts as a rigid piston and the 2D MoS_2 layer. Green and orange spheres indicate Na^+ and Cl^- ions, respectively. Pure water is located underneath the 2D MoS_2 layer to prevent the dispersion of filtered water. (b) Time-lapse snapshot images of water desalination through the near atomic vacancy of the 2D MoS_2 layer during 40 ps MD simulations.

4.4 Conclusion

In summary, we experimentally evaluated the performances of CVD-grown few-layer 2D MoS_2 of ~7 nm thickness as water permeable membranes for desalination and molecular sieving. This near atom-thick membrane presented an excellent combination of high water permeability and high ionic sieving capability for a variety of tested ions, outperforming previously developed 2D MoS_2 layer membranes of much larger thickness. This experimentally confirmed superiority is believed to be a combined result of small thickness and near atomic vacancies inherent to CVD-grown 2D MoS_2 layers, verified by STEM characterization and MD simulation. The present study merits further investigations towards the potential exploration of 2D materials for high-efficiency membrane and desalination technologies.

CHAPTER 5: WATER DESALINATION VIA VERTICALLY-ALIGNED 2D MOS_2 LAYERS MEMBRANES

5.1. Introduction

The past decades have seen an escalating global shortage of freshwater resources due to the spiraling rise of water demands from the agricultural and industrial sectors.[5] Apart from the management and conservation of existing water resources, more environmentally and technologically sustainable solutions that facilitate increasing freshwater supplies are urgently demanded around the globe in mitigating the challenging impacts of the looming water crisis, particularly during the rapidly evolving effects of climate change.[6] Significant technological and research efforts have been devoted towards seawater desalination techniques, due to the abundance and accessibility of oceans and seas, aiming to produce freshwater in a more time and energy efficient manner.[10] Amongst the most widely adopted desalination technologies are the multi-stage flash (MSF), multi-effect distillation (MED), and reverse osmosis (RO), with RO increasingly attaining more market share.[7,8] As a pressure-driven process, the RO polymeric membranes still face unfavourable technical drawbacks in particular low conversion efficiency, and the high energy demand for pressurising the feedwater. Therefore, the development and adoption of high-performance membrane materials still present compelling demands, especially materials armed with an inherently balanced combination of optimal water recovery efficiency and maximised solute rejection rates.

Two-dimensional (2D) materials based membranes have rapidly emerged as a promising candidate for addressing and overcoming the undesirable trade-offs between permeability and selectivity for improved desalination performances.[11-13,149]

Their desirable unique suitability stems from a combination of the ultra-thinness of only one-to-few molecular layers which allows for rapid water pathways as well as superior ionic/molecular sieving capabilities due to versatile mechanisms (e.g., in-plane nanopores, interfacial voids, and inter-gallery channels).[12] In addition, many other attributes of 2D materials including their high mechanical flexibility and chemical functionality further qualify them as a favourable alternative towards high-performance desalination. Moreover, the chemical synthetic processing routes can impart intrinsic sieving/filtration nano-channels which can be even further tailored towards desired channel sizes, distribution density, and orientation configurations for optimal desalination capabilities.[14,228,229]

In this endeavour, the ionic sieving and water permeation performance of various types of 2D materials have been explored, with the most notable categories of examples include graphene,[15-18,230] dichalcogenides,[19-22,231] and graphene oxides.[23-26,232]

Amongst a host of 2D materials based membranes, 2D molybdenum disulfide (MoS_2) layers attracted newly gained research efforts for their promise in water and environmental fields,[149,153] along with their demonstrated superior properties in various other fields of applications including electronics,[233] catalysis,[234] biomedical,[235] and energy conversion and storage[236]. In addition to their inherent structural advantages, other attributes such as excellent chemical stability and non-toxicity further make 2D MoS_2 layers a fitting candidate for high-performance desalination applications.[35-37] Despite their promising potential as an efficient membrane material for water desalination applications, only limited experimental research efforts have been devoted towards the investigation of 2D MoS_2 layers for their ionic sieving and water permeation capabilities, whilst extensive theoretical projections based on molecular dynamics simulations have already revealed their promising outlooks in this

regard.[19,149,154,155,237] Recent experimental desalination assessments of 2D MoS_2 flakes/layers based membranes include chemically functionalised ~5 μm thick laminar membranes composed of exfoliated 2D MoS_2 flakes via a filtration process.[157] Moreover, a recent notable work by Li *et al*. reported the experimental demonstration of high-efficiency water desalination membranes based on horizontally-aligned few-layer 2D MoS_2 of only ~7 nm thickness, attributing the high performance to the small thickness and near atomic vacancies inherent to the CVD-grown 2D MoS_2 layers.[238]

Compared to their horizontally-aligned counterparts, vertically-aligned 2D / nano materials have received even more scarce research efforts for their potential roles in environmental applications, both in terms of theoretical and experimental investigations. Amongst the limited reported results, few explored the theoretical performance of vertical graphene-based membranes, whilst the majority of the efforts have been devoted to vertically-aligned carbon nanotubes (VA-CNTs).[229,239-242] In addition, a recent MD simulations work by Köhler *et al*. has suggested that theoretically the transport of water through MoS_2 nanotubes can be as anomalous as in CNTs, potentially have promising applications such as nano-filtration.[243] In this Chapter we present results and discussions on the superior ionic sieving capability of a vertically-aligned 2D MoS_2 layers based membrane, both the experimentally demonstrated capabilities, with a special attention on the comparisons with its horizontal counterparts[238] with regards to the differences in performances and the respective underlying mechanisms.

5.2. Experimental Methods

CVD Growth of 2D VA-MoS_2 Layers: Ultra thin films of Mo (6 nm thickness) were deposited onto SiO_2/Si substrates via electron beam evapouration (Thermionics VE-100 evapourator) at a deposition rate of 0.15 Å s^{-1}. As-deposited Mo-SiO_2/Si samples were then centrally-placed inside a 1 inch quartz tube located in the middle of a horizontal tube furnace (Lindberg Blue M, ThermoScientific). Sulphur powders (99.5%, Sigma-Aldrich, St. Louis, MO) placed in a ceramic boat were then loaded within the quartz tube at the furnace upstream side. The furnace was then pumped down to a base pressure of 1 mTorr following purging with high-purity argon (Ar) gas. The tube system was then ramped up to 780 ℃ at a ramping rate of 15 ℃/min for 50 mins and was held for another 50 mins under the constant flow of Ar gas (100 SCCM), with a working pressure of 75 mTorr. After the CVD reaction, the furnace was naturally cooled down to room temperature under continuous Ar supply.

Water Permeation Rate Measurement: A typical external pressure method was used for the water permeation rate assessments via a common dead-end filtration setup. The sandwiched membrane with exposing holes over the vertically-aligned 2D MoS_2 layers was secured inside a leak-free syringe filter holder. The water permeation rate was calculated by weighing the volume of water passing through the 2D VA-MoS_2/PES membrane area under a constant pressure of 1 bar as a function of time.

Salt Ion Rejection Rate Measurement: A conductivity probe (ThermoScientific, model: Orion 013605MD) connected to a solute conductivity meter (ThermoScientific, model: Orion 5 Star) was used to monitor conductivities in respective containers, in order to quantify salt ion concentration variations. The conductivity probe was calibrated on a routine basis, and was thoroughly rinsed with de-ionised water each before measurements. The salt rejection rate was

calculated via $\left(1-\frac{C_P}{C_F}\right)\times 100\%$, where C_P and C_F are the conductivity of the permeate and feed side, respectively. Common seawater salt types of sodium chloride (NaCl) (99%, Sigma-Aldrich, St. Louis, MO), potassium chloride (KCl) (99%, Sigma-Aldrich, St. Louis, MO), magnesium chloride ($MgCl_2$) (98%, Sigma-Aldrich, St. Louis, MO), and calcium chloride ($CaCl_2$) (93%, Sigma-Aldrich, St. Louis, MO) were employed for salt rejection rates measurements. The seawater salt solutions tested were as follows: (1) NaCl of 0.6 M (equivalent to seawater salinity concentration[209]), (2) NaCl of 0.469 M (typical seawater Na^+ concentration[210]), (3) KCl of 0.1 M, (4) $MgCl_2$ of 0.1 M, (5) $CaCl_2$ of 0.1 M, (6) actual seawater sampled from the Florida Atlantic coast, and (7) synthetic seawater. The concentration of 0.1 M for KCl, $MgCl_2$ and $CaCl_2$ was selected for measurements consistency, although the typical seawater concentrations of K^+, Mg^{2+} and Ca^{2+} are below 0.1 M.[210,211] The synthetic seawater solution was prepared to mimic the concentrations of typical salt ion species present in standard seawater, i.e., Na^+ of 0.469 mol/L [210], K^+ of 0.01 mol/L [210], Mg^{2+} of 0.0528 mol/L [210], and Ca^{2+} of 0.01 mol/L [210]. Each measurement was repeated for three times to improve testing consistency, with the averaged values presented in the corresponding plots.

AFM Characterisation: Topography images and height profiles of the vertically-aligned 2D MoS_2 layers integrated on PES substrates were acquired with Anasys nanoIR AFM (Anasys Instruments, Santa Barbara, CA) operated in tapping mode with the scan rate of 1 Hz. The AFM probes (Model: PR-EX-T125-10, Anasys Instruments) had a nominal spring constant of 30 N/m.

5.3. Results and Discussions

5.3.1 Vertical 2D MoS2 Layers Preparations and Characterizations

Vertically-aligned (VA) 2D MoS_2 layers of centimetre-scale were grown based on a modified chemical vapour deposition (CVD) process previously developed in our research group.[195-197] A thin film of Mo (~6 nm thickness) was deposited onto a SiO_2/Si substrate via electron beam evaporation, followed by a thermal sulphurisation process inside a CVD chamber, producing VA 2D MoS_2 layers. Conditions for VA 2D MoS_2 layers growth are detailed in *Methods* section. As-prepared VA 2D MoS_2-SiO_2/Si sample following the CVD process was then facilely delaminated via a water-assisted process, with the afloat VA 2D MoS_2 layers gently transferred onto an O_2 plasma treated porous poly(ether sulfone) (PES) membrane substrate (~0.03 μm pore size and ~100 μm thickness, Sterlitech, WA), which has been extensively employed as substrate for assessing desalination performance of 2D materials-based membranes.[199] The 2D VA-MoS_2/PES surface was then covered with a selectively deposited thin layer of non-permeable polydimethylsiloxane (PDMS), exposing a pre-defined open region of 2D vertically-aligned MoS_2 layers as the ionic sieving membrane upon solutions contact (Figure 32(a)). The growth, delamination, transfer and integration of 2D layers onto PES substrates followed similar procedures as illustrated on our previous report.[238] With the PES substrate possessing pores greatly exceeding the sizes of salt ion species, the ionic sieving effects can only be attributed to the 2D VA-MoS_2 layers (with the possible mechanism shown schematically in Figure 32(b) and discussed in detail in latter sections of this Chapter).

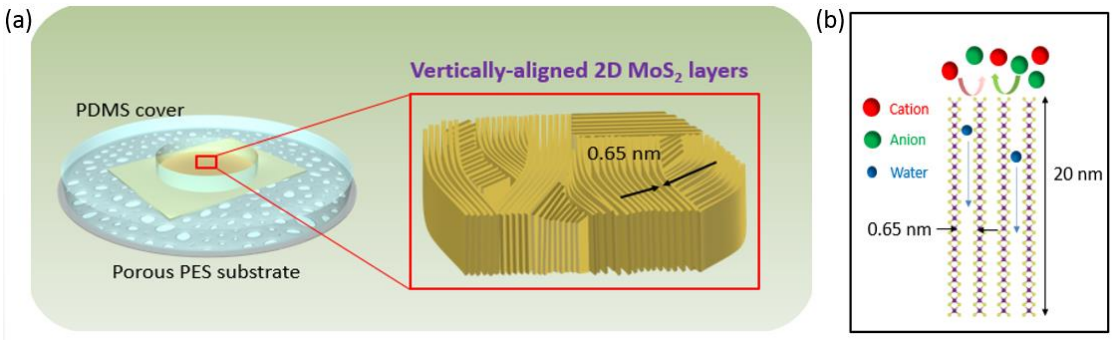

Figure 32 (a). Schematic depiction of 2D VA-MoS_2 layers integrated onto porous PES substrate. A non-permeable PDMS layer is selectively deposited on the MoS_2/PES, leaving an opened area allowing water/solution penetration through the exposed 2D VA-MoS_2 layers. The enlarged view of the red rectangle area shows the vertical alignment of the 2D VA-MoS_2 layers, note the vdW gaps of ~0.65 nm as indicated by the arrows. (b). Schematic illustration of proposed mechanism for the water permeation and salt rejection of 2D VA-MoS_2 layers. The inherent vdW gaps of the vertically-aligned MoS_2 layers pose restrictions towards inbound salt ions mainly due to size exclusions. Whilst the hydrophobic interior regions between the MoS_2 layers facilitate smooth transport of water molecules.

Prior to the integration of VA 2D MoS_2 layers onto PES substrates, the material quality of as-grown 2D MoS_2 layers was first assessed. The structural and chemical integrity of the CVD-grown VA 2D MoS_2 layers were characterised via transmission electron microscopy (TEM) and Raman spectroscopy. A plane-view of the as-grown 2D MoS_2 layers via HR-TEM clearly demonstrates the vertical alignment of 2D MoS_2 layers (Figure 33(a)), with the inset showing a typical interlayer spacing of ~0.65 nm between the adjacent MoS_2 layers. In addition, a cross-sectional view of the 2D MoS_2 layers via TEM (Figure 33(b)) reveals the presence of continuous 2D MoS_2 layers that are of uniform thickness. Shown as an enlarged view of the blue box in Figure 33(b), the crystalline structure of 2D MoS_2 layers is further revealed in

Figure 33(c) with the corresponding atomic arrangements of the 2D MoS_2 layers also illustrated as in the red boxes, which further clarifies the vertical orientation of the 2D MoS_2 layers, and again confirms an average interlayer spacing of ~0.65 nm. Furthermore, the typical Raman spectrum of the as-grown MoS_2 layers (red spectrum line in Figure 33(d)) confirms the presence of 2D MoS_2 layers, with the two distinctive peaks corresponding to the in-plane (E^1_{2g}) and out-of-plane (A_{1g}) vibration modes of 2D MoS_2 layers, respevtively.[185,201,202] These comprehensive characterisation results conclude that our CVD-grown 2D MoS_2 possess continuous and vertically-aligned layers, with multitudes of intrinsic sub-nanometre vertical channels (e.g., ~0.65 nm vdW gaps). Such microstructural attributes impart VA 2D MoS_2 layers with unique suitability as desalination membranes.

Subsequent morphological characterisations of the as-integrated VA 2D MoS_2 layers on PES substrates were performed via atomic force microscopy (AFM) and Raman spectroscopy. The AFM height profile (Figure 33(e)) corresponding to the yellow line across the VA 2D MoS_2 / PES interface (Figure 33(e) inset) shows that the integrated 2D VA-MoS_2 layers are ~20 nm thick (which is within the reasonable range as produced from a 6 nm Mo seed layer). The Raman profile of the as-integrated VA 2D MoS_2 layers / PES (blue spectrum line in Figure 33(d)) reveals the resembling characteristic peaks of E^1_{2g} and A_{1g} vibration modes, which are consistent with the observation prior to 2D layers separation and integration (i.e., near-overlapping red spectrum line in Figure 33(d)). The results confirm that after the VA 2D MoS_2 layers integration onto PES substrates, they preserved a maintained structural and chemical integrity.

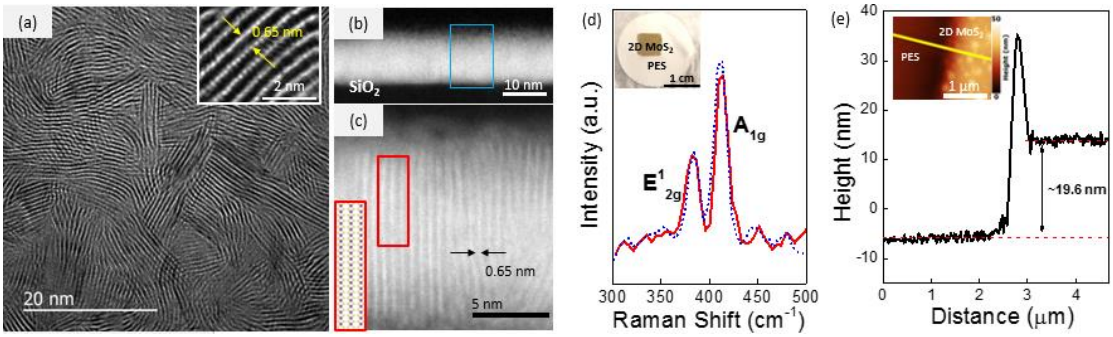

Figure 33 (a). Plane view of the HR-TEM imaging of the smooth 2D VA-MoS_2 layers, clearly showing the vertical alignment of the 2D MoS_2 layers. The inset shows a zoomed-in view of the vertical layers with well-defined vdW gaps of ~0.65 nm as indicated by the yellow arrows. (b). A cross-sectional view of the 2D VA-MoS_2 layers, showing continuous 2D VA-MoS_2 layers with uniform thickness. (c). An enlarged view of the 2D VA-MoS_2 layers as shown in the blue rectangle area in Figure 33(b), showing the vertically-aligned nano-channels formed in between the parallel 2D MoS_2 layers, again with a well-defined vdW gaps distance of ~0.65 nm (indicated by the black arrows). Atomic schematic representation of the vertical MoS_2 nano-channels is also depicted (see the two corresponding areas in the red rectangles). (d). Typical Raman spectra of the 2D VA-MoS_2 layers before (red line) and after (blue line) the PES integration, showing the two distinctive peaks corresponding to the E_{2g}^1 and A_{1g} vibration modes. The inset picture shows a representative sample after the 2D VA-MoS_2 layers (dark gold area) have been integrated onto the PES substrate (white area). (e). Representative AFM height profile of 2D VA-MoS_2 layers integrated onto the PES substrate, here showing a thickness of approximately 20 nm. The height profile was taken along the gold-coloured line on the inset AFM imaging, across the boundary between the PES substrate and the 2D VA-MoS_2 layers.

5.3.2 Water Permeation Assessments

Figure 34(a) illustrates a schematic set-up for water permeation measurements. The 2D VA-MoS_2 layers-integrated PES substrate was covered with another bare PES substrate. After the 2D layers integration, the sample was subsequently sandwiched between two non-permeable PDMS sealing films both exposing pre-defined open areas overlapping with the 2D VA-MoS_2 layers membrane region. Note that this sandwich-like assembly has been extensively employed in configuring nanomaterials-based membranes including 2D materials of large thickness (> 1 μm).[157] This layered membrane was then loaded inside a syringe filter holder in a typical dead-end filtration setup. The water permeation rate was then measured via common external pressure method by weighing the volume of water passing through the membrane area (i.e., the central hole filtration region composed of 2D VA-MoS_2/PES only) as a function of time under a constant pressure. Details are presented in the *Methods* section.

Due to the vertical nature of the 2D MoS_2 layers configuration in our case, the pathways that allow passage for water molecules are treated as parallel continuous nano-channels, which should account for the vast majority of water permeation, with some types of defects (e.g., edge sites and dislocations) may only have very insignificant contributions.

Before proceeding with the experimental assessments of the water permeation capability of 2D VA-MoS_2 layers, it is worth exploring the theoretical performance of water permeability of a single nano-channel of vertical 2D MoS_2 layers (and this *per nano-channel* estimation will be further extended to the *per unit area* value).

Since the "openings" for water molecules to penetrate upon contact on the surfaces of 2D VA-MoS_2 layers do not present themselves as geographical "holes", (instead, there are parallel "slits" composed of adjacent nano-channels). Therefore, for the sake of reasonable and

simplified estimations, the preferable "opening" for water molecules permeation is considered as the area defined by the following two dimensional factors: (1). the width of each of the parallel "slits" d=0.333 nm [244], and (2). the Sulphur-to-Sulphur distance within a single 2D MoS_2 layer d_S=0.316 nm [245].

The theoretical water permeation capability of 2D VA-MoS_2 layers is based on the Hagen-Poiseuille (H-P) permeability, which describes the water flux under ideal and non-slip flow conditions through cylindrical pores, and is widely adopted as a base for theoretical estimations.[239,246,247]

The theoretical H-P permeability for vertical 2D MoS_2 layers maybe calculated via the following equation:[239,247]

$$Q = \frac{\pi(\frac{d}{2})^4}{8\mu} \cdot \frac{\Delta P}{L} \qquad (2)$$

Where

Q = The water flux = the volume of water passage per unit time, per unit pressure, per nano-opening

d = Size of nano-opening

μ = Viscosity of de-ionised water (at 20 ℃) [248]

ΔP = Trans-membrane pressure

L = Nano-opening length

Therefore, from Equation. 2, the theoretical H-P permeability is calculated as:

$$Q = 5.54 \times 10^{-18} \frac{L}{h \cdot bar \cdot opening}$$

Furthermore, based on the dimensional factors (d and d_S) mentioned above, the number of nano-openings per 1 cm^2 for 2D VA-MoS_2 layers can be estimated as 4.88×10^{14} $\frac{Opening}{cm^2}$, which is the areal density. Note this estimation is at least 50 times more compared to that of the horizontally-aligned CVD-grown 2D MoS_2 layers.[41]

Therefore, the theoretical estimation of the Hagen–Poiseuille permeability of a typical 2D VA-MoS_2 layers sample (under ideal, non-slip conditions) can be deduced by combining Equation. 2 and the estimated areal density, which gives:

$$Q_{H-P} = 27 \frac{L}{h \cdot bar \cdot m^2}$$

For comparisons, the reported theoretical Hagen–Poiseuille water permeability of vertical CNTs varies in a wide range: from $Q = 0.0053$ $\frac{L}{h \cdot bar \cdot m^2}$ to $Q = 3.35$ $\frac{L}{h \cdot bar \cdot m^2}$ (due to varied sample parameters like pore densities and sizes).[247]

The experimentally assessed water permeation rate, based on the common dead-end filtration method, for 2D VA-MoS_2 layers is $Q = 1656.8\ (\pm 129.7)$ $\frac{L}{h \cdot bar \cdot m^2}$.

The prominent difference of the water permeations rates between the theoretical Hagen–Poiseuille permeability and the experimentally assessed values indicate that the vertical 2D MoS_2 layers possess highly slippery nano-channels for water molecules. Comparable and sometimes even more dramatic enhancement effects on water permeability have been reported on vertical CNTs membranes.[247,249-251]

We believe the hydrophobicity of the vertical 2D MoS_2 layers would most likely account for such contrasting differences. For comparison, the underlying mechanism behind the significant enhancement effects for vertical CNTs has been similarly attributed to hydrophobic–hydrophobic interaction, stemming from the hydrophobicity of the inner wall of CNTs.[239,252] Furthermore, theoretical MD simulations study also supports the presence of an induced super-flow regime inside MoS_2 nanotubes, leading to high water mobility.[243]

Comparing to the their horizontally-aligned counterparts, vertical 2D MoS_2 layers clearly show a higher water permeability (see the comparison plot in Figure 34(b)).[238] Such contrast is ascribed to the different pathways that water molecules take. In the case of horizontal-MoS_2 2D layers, water translocates through the nanopores as well as transports within the interlayer vdW gaps.[238] Whilst in 2D VA-MoS_2 layers, three main factors are at play contributing to the enhanced water permeability: 1). the available passages for water molecules become more abundant, due to the presence of the numerous "slits" like openings (i.e., the vdW gaps between layers of vertical MoS_2); 2). the vertically-aligned layers present much more straightforward "straight-to-the-end" passages, compared to the "zig-zag" routes that water molecules take when migrate through the horizontal MoS_2 layers; and 3). the hydrophobicity of the interior regions between the vertical MoS_2 layers further leads to rather "slippery" pathways for water molecules to move more smoothly.

5.3.3 Salt Rejection Evaluations

In addition to the superior water permeability capability discussed above, the salt rejection performances of 2D VA-MoS_2 layers were also assessed.

The proficiency of 2D VA-MoS_2 layers on PES supports for salt ions rejection was determined via the bespoke measurement set-up (depicted in Figure 34(c)) as described in detail in our previous report, following similar procedures and testing conditions.[238] In brief, a leak-free solution passage via only the sandwiched 2D VA-MoS_2 layers connects the permeate and feed side containing de-ionised water and different types of testing salt solutions respectively. The levels of the migration of salt ions were quantified via the conductivity measurement method well established in the field;[157] i.e., the salt rejection rate was calculated by $\left(1-\frac{C_P}{C_F}\right)\times 100\%$, where C_P and C_F are the conductivity of the permeate and feed side, respectively.[208] Measurement procedures, conditions as well as the different types of salt solutions underwent testing are detailed in the *Methods* section. Figure 34(d) presents the plots of seawater ion rejection rates obtained at identical interval times during the course of three hours towards various types of respective salt ion species, whilst the plots for multi-ionic mixture solutions are given in Figure 34(e).

The results (as given in Figure 34(d) and Figure 34(e)) show a high level of capability for 2D VA-MoS_2 layers acting as reliable hindrance to the passage of common seawater salt ion species at various concentrations, for both single-ionic and multi-ion mixture solutions (with an overall salt rejection rate of > 99.7%).

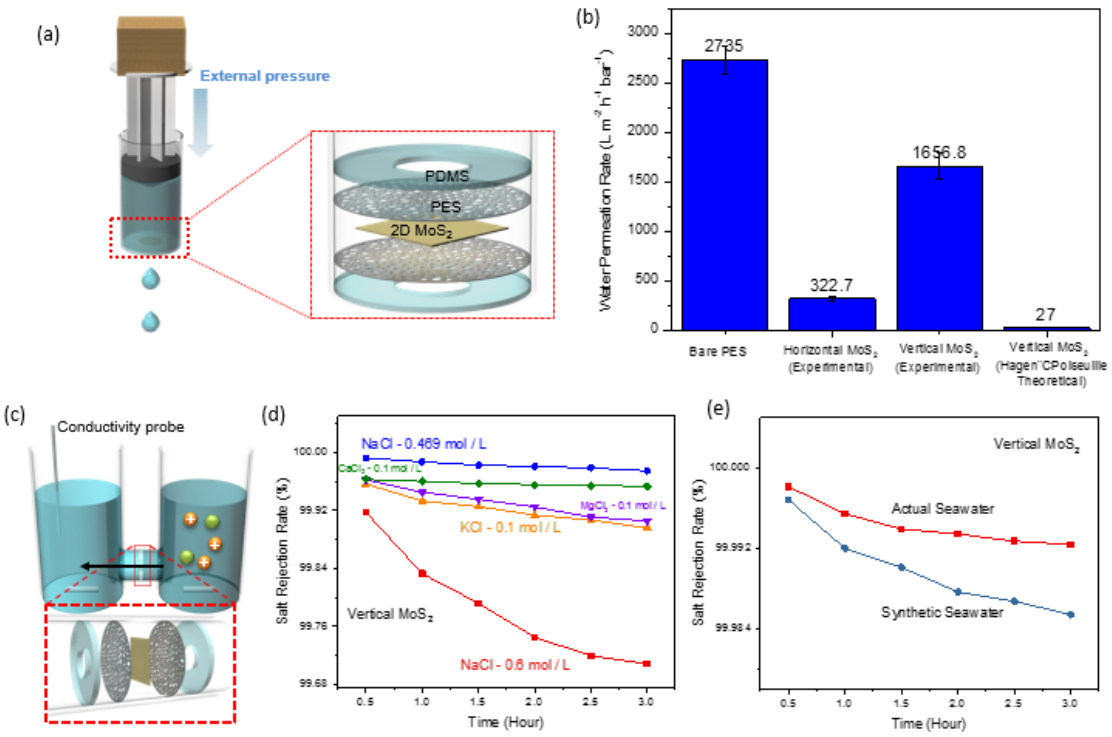

Figure 34 (a). Schematic depiction of the water permeation measurement set-up. The enlarged view shows the sandwiched membrane composed of 2D VA-MoS_2 layers integrated on PES substrate, with another bare PES covered on top of them. The selectively-deposited PDMS regions are also shown with the circular areas left open for water/solution penetration. (b). The comparisons of water permeation rates for: 1). bare PES substrates, 2). horizontal 2D MoS_2 layers,[238] 3). vertically-aligned 2D MoS_2 layers, and 4). the theoretical Hagen-Poiseuille permeability of 2D VA-MoS_2 layers. (c). Schematic representation of the salt rejection rates measurement set-up. The sandwiched membrane composed of 2D VA-MoS_2 layers / PES, with selective PDMS sealing is shown in the enlarged view. (d). Salt rejection rates of 2D VA-MoS_2 layers towards various types of seawater ions over a continuous 3-hr time period. (e). Salt rejection rates of 2D VA-MoS_2 layers towards synthetic and actual seawater samples over a continuous 3-hr time period.

Due to the similarity of assessment methodology and testing conditions, the following discussions focus on the salt ions rejection performance of 2D VA-MoS_2 layers as compared to their horizontal counterparts, in addition to comparisons with vertical-CNTs.

It is found that across all the different types of ionic solutions, the vertically-aligned 2D MoS_2 layers show a slight yet consistently higher performance in terms of salt rejection rates under similar testing conditions compared to the horizontally-aligned 2D MoS_2 layers[238] (representative optical imaging of 2D H-MoS_2/PES and TEM imaging of the horizontal layers are shown in Figure 35(a)). The respective salt rejection performance comparison plots are given in Figure 35(b)-(f) for single-ionic solutions, and in Figure 35 (g)-(h) for multi-ionic mixture solutions. This improvement of performance may due to two possible reasons (also illustrated in Figure 32(b)): 1). Compared to H-MoS_2 layers, which possess nano-pores of varying degrees of sizes, the VA-MoS_2 layers instead contain filtration networks of near-consistent dimensions (i.e., tiny "slits" of approximately 0.65 nm in width. See Figure 33(a) and Figure 33(c)). Such narrow-sized vdW gaps "slits" are well-suited for allowing the smooth and even maybe accelerated passage for water molecules, which have a diagonal length of ~0.275 nm.[203] And at the same time, the hydrated salt ions face both dimensional exclusions upon encountering the narrow "slits" due to their larger sizes (also note the actual Sulphur-to-Sulphur distance of ~0.3 nm.[244]), and the energetic impedance of having to lose their solvation shells if they are to squeeze through.[225,226] Additionally 2). The thickness of 2D VA-MoS_2 layers are inherently higher than that of the H-MoS_2 layers, since the growth of vertical 2D MoS_2 layers prefers thicker (>~3 nm) Mo-seed layers.[185] Thus possessing lengthened barriers preventing the salt ions from passing through.

Despite many MD simulations works[253,254] as well as extensive experimental investigations[229,247] on the potential of VA-CNTs membranes for desalination applications, their practical feasibility has been limited by the actual pore sizes which remain larger than 1 nm [213,239,247], greater than the hydrated radius of typical salt ions (e.g., Na^+ of 0.72 nm).[225,239] It is worth noting that extensive molecular dynamics simulations have shown that the inner pore diameter of VA-CNTs should reach ~0.6 nm for optimal salt rejection rates.[240,253,254] Although the present technologies have the capability to reduce the pore diameter of VA-CNTs to this range, a critical pore size of ~0.7 nm would pose as a limiting factor, beyond which the transport of water will be impeded due to the confinement effect.[240,253,255] Therefore, although VA-CNTs have demonstrated exceptionally high experimental water permeability (e.g., up to 10,500 $\frac{L}{h \cdot bar \cdot m^2}$) [247], their practical prospect as salt rejection membranes remains uninviting.[239,240,256,257] For example, molecular modelling indicates that even with a pore diameter of 0.75 nm for VA-CNTs membranes, they would only yield a 58% of salt rejection capacity.[253,254] Furthermore, experimental investigations of the salt rejection capacity of VA-CNTs membranes show that with an average pore size of 1.6 nm, only up to 60% ion exclusion efficiency was observed.[258] Therefore, alternative to seawater desalination, vertical CNTs have instead found promising application potential as filtration membranes towards larger-sized species like heavy hydrocarbons and microbial contaminants.[256,259]

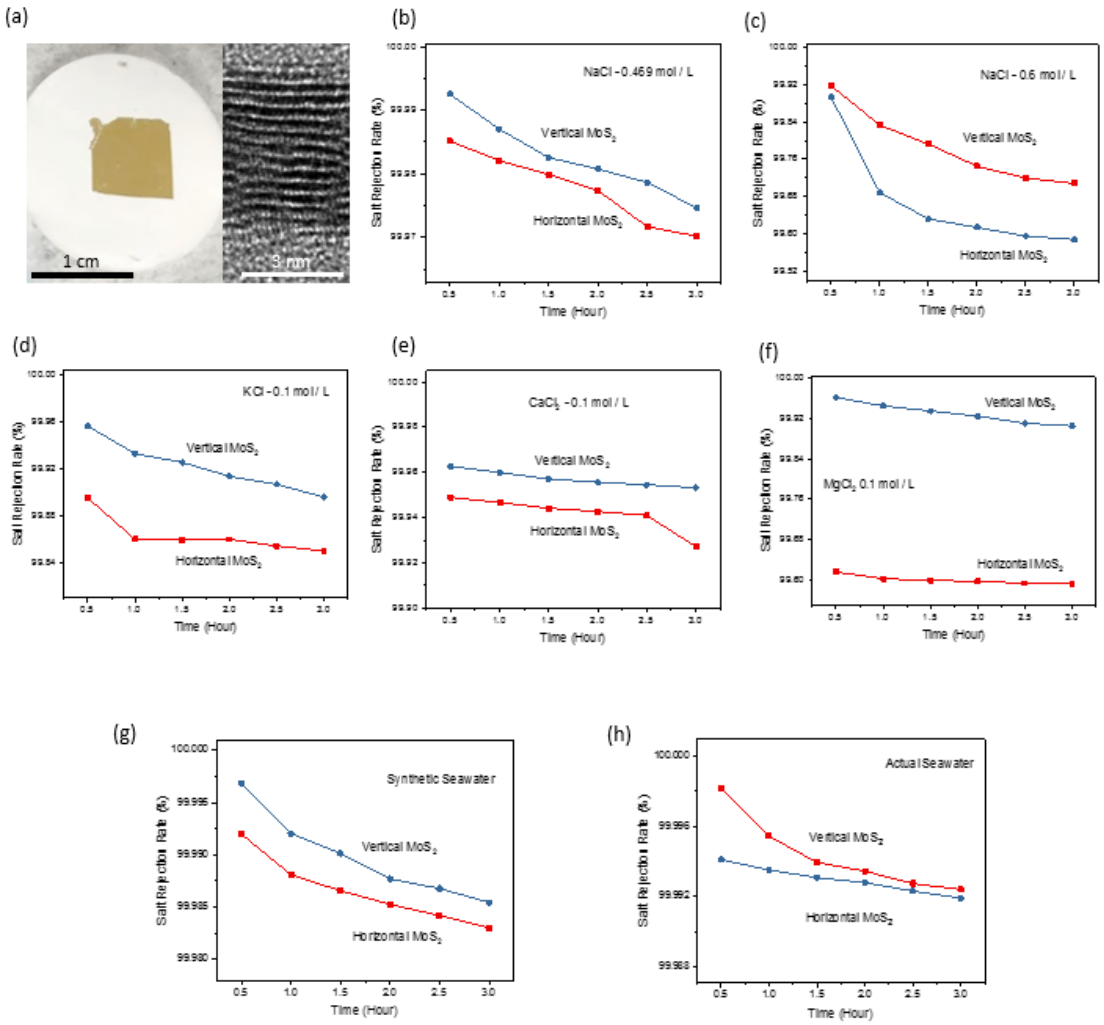

Figure 35 (a). Representative optical imaging of the 2D horizontal-MoS_2 layers integrated onto PES substrate. Along with a top-view HR-TEM imaging showing the horizontally-aligned 2D MoS_2 layers. (b). Comparison plots of the respective salt rejection rates for 2D vertically-aligned MoS_2 layers and 2D horizontally-aligned MoS_2 layers towards 0.469 mol/L NaCl solution over a continuous 3-hr time period under similar measurement conditions. (c). Comparison plots of the respective salt rejection rates for 2D vertically-aligned MoS_2 layers and 2D horizontally-aligned MoS_2 layers towards 0.6 mol/L NaCl solution over a continuous 3-hr time period under similar measurement conditions. (d). Comparison plots of the respective salt rejection rates for 2D vertically-aligned MoS_2 layers and 2D horizontally-

aligned MoS_2 layers towards 0.1 mol/L KCl solution over a continuous 3-hr time period under similar measurement conditions. (e). Comparison plots of the respective salt rejection rates for 2D vertically-aligned MoS_2 layers and 2D horizontally-aligned MoS_2 layers towards 0.1 mol/L $CaCl_2$ solution over a continuous 3-hr time period under similar measurement conditions. (f). Comparison plots of the respective salt rejection rates for 2D vertically-aligned MoS_2 layers and 2D horizontally-aligned MoS_2 layers towards 0.1 mol/L $MgCl_2$ solution over a continuous 3-hr time period under similar measurement conditions. (g). Comparison plots of the respective salt rejection rates for 2D vertically-aligned MoS_2 layers and 2D horizontally-aligned MoS_2 layers towards synthetic seawater over a continuous 3-hr time period under similar measurement conditions. (h). Comparison plots of the respective salt rejection rates for 2D vertically-aligned MoS_2 layers and 2D horizontally-aligned MoS_2 layers towards actual seawater over a continuous 3-hr time period under similar measurement conditions.

Comparisons of water permeability of 2D VA-MoS_2 layers (the present work) with reported performances of VA-CNTs and commercial ultrafiltration (UF) are given in Table 3 Comparisons of membrane specifications and water permeability., along with the corresponding materials properties of the testing samples. (Note: Amongst the reported results for VA-CNTs, there are vast performance differences because of inherent variations of sample parameters like pore densities and sizes).

Table 3 Comparisons of membrane specifications and water permeability.

Membrane specifications	This study	Lee *et al.*[247]	Yu *et al.*[250]	Zhang *et al.*[260]	Baek *et al.*[239]	Hinds *et al.*[249]	Holt *et al.*[246]	Du *et al.*[241]	UF [247]
Average (CNT) inner diameter, nm	N/A	4.1	3.0	10	4.8	7.5	1.6	10	5.7
Thickness, nm	19.6	10^6	7.5×10^5	1.2×10^5	2×10^5	5×10^3	2.5×10^3	4×10^6	2×10^4
Pore density, 10^{10} pore /cm^2	4.88×10^4	300	290	10	6.8	6	25	2.4	9
Water permeability at 20 ℃, L m^{-2} h^{-1} bar^{-1}	1,657	10,500	2,740	1,913	1,100	606	267	234	32
Calculated water	270,000	677	276	7,348	159	33,481	578	53	4,096

permeability at 20 ℃, $\times 10^{-4}$ L m^{-2} h^{-1} bar^{-1}									

5.4 Summary

In summary, we experimentally evaluated the performances of vertically-aligned CVD-grown 2D MoS_2 layers (approximately 20 nm in thickness) as water permeable membranes for desalination and ionic sieving. This ultra-thin membrane presented an excellent combination of high water permeability and high ionic sieving capability for a variety of tested ions, which with improved performances compared to horizontally-aligned 2D MoS_2 layer layers membranes. This experimentally confirmed superiority is believed to be a combined result of small thickness and the hydrophobic interiors regions of the vertical MoS_2 layer sheets. The present study merits further investigations towards the potential exploration of 2D materials for high-efficiency membrane and desalination technologies.

CHAPTER 6: CONCLUSIONS

In summary of the present dissertation, the behavior of the internal potential barrier in a polymer-derived amorphous SiAlCN ceramic was studied by measuring its complex impedance spectra at various dc bias as well as different testing and annealing temperatures. The complex impedance spectra of the polymer-derived a-SiAlCN were measured under various dc bias voltages in a temperature range between 50 and 150 °C, as well as different annealing temperatures (1100-1400 ℃). All spectra, regardless of temperature and bias, consist of two semi-circular arcs, corresponding to the free-carbon phase and the interface, respectively. The impedance of the free-carbon phase is independent of the bias, while that of the interface decreased significantly with increasing dc bias. It is shown that the change of the interfacial capacitance with the bias can be explained using the double Schottky barrier model. The charge-carrier concentration and potential barrier height were estimated by comparing the experimental data and the model. The results revealed that increasing testing temperature led to an increased charge-carrier concentration and a reduced barrier height, both following Arrhenius dependence, whereas the increase in annealing temperature resulted in increased charge-carrier concentration and barrier height. The phenomena were explained in terms of the unique bi-phasic microstructures of the material. The research findings reveal valuable information of temperature-dependent properties of polymer derived ceramics, and should contribute towards more precise understanding and control of the electrical as well as dielectric properties of polymer derived ceramics.

Furthermore, the desalination performances and underlying mechanisms of two-dimensional CVD-grown MoS_2 layers membranes have been experimentally assessed. Based on a successful large-area few-layer 2D materials growth, transfer and integration method, the 2D

MoS_2 layers membranes showed preserved chemical and microstructural integrity after integration. We experimentally evaluated the performances of CVD-grown few-layer 2D MoS_2 of ~7 nm thickness as water permeable membranes for desalination and molecular sieving. This near atom-thick membrane presented an excellent combination of high water permeability and high ionic sieving capability for a variety of tested ions, outperforming previously developed 2D MoS_2 layer membranes of much larger thickness. Such performances are attributed to the dimensional and geometrical effect, as well as the electrostatic interaction of the inherently-present CVD-induced atomic vacancies (as verified by STEM characterization and MD simulation) for governing both water permeation and ionic sieving at the solution/2D-layer interfaces. The present study merits further investigations towards the potential exploration of 2D materials for high-efficiency membrane and desalination technologies.

CHAPTER 7: FUTURE WORK

The interfaces of nanomaterials are integral parts for defining the properties and performances of many types of materials. Therefore, the investigations of the roles of interfaces should also be extended to the studies of inherent properties of their bordering phases as well as the influences of the externally applied fields. The following suggestions are proposed for aiding future research efforts.

(a).

The eventual aims of the investigations on the electrical and dielectric properties of polymer derived ceramics is multi-fold: (1) to understand the origin and fundamental mechanism of conductions; (2) to decipher the microstructure-processing-properties relationships (i.e., how the different parameters / conditions / techniques would influence its electrical / dielectric performance); (3) to gain in-depth knowledge of better controlling / targeting its structures and properties towards different and wider applications (e.g., harsh environment sensing, and environmental barrier coatings). There are a number of factors that could influence its eventual performance, for example: (a) the ratio of initial ingredients; (b) the processing temperatures; (c) temperatures under which the PDC materials operate; and (d) contaminations (especially oxygen species) introduced during processing steps. Based on the results and discussions of the present investigations, in order to continue to build a more thorough understanding of controlling the electrical and dielectric properties of PDCs (for scientific research as well as practical applications purposes), the following further recommendations are provided as a suggestive guideline:

(1). Since the PDCs materials are particularly notable for their high-temperature-stable properties as well as promising future applications under harsh environments, it would be empirical to investigate the performance of PDCs (in particular their electronic / dielectric properties) under in-service conditions / environments. Though many research works have demonstrated the structural stability of PDCs, its long-term influence over PDCs microstructures and properties still demand in-depth efforts before the materials render practically useful. In addition, impedance measurements of even wider ranges should be investigated as temperatures could have shifted peaks towards higher ends.

One additional aspect of a future research direction worth pursuing of is to study the synergistic effects of the material's responses to both temperatures and external compressive pressures. It was found / observed that the polymer derived SiAlCN ceramics, at the same time, show prominent responses to varying degrees of temperatures and pressure. This effect could undermine its future applications for harsh environment sensing, since the actual operating environment of such sensors would have both rapidly-changing temperatures and pressures present. Since these two effects arise from different origins, it truly worth more further explorations on the improved control of this effect. It is suggested that one approach to reduce such effect would be to study how the processing / annealing route would affect such synergistic effect. And another more resistive path would be to combine electrical engineering knowledge via clever design of circuits to minimise the effect, which would normally require product shape-control technique during processing.

(2). To study the effect of microstructures on the double Schottky barriers model in controlling PDC dielectric properties. Especially the electronic band / energy structures of PDCs with different annealing / pyrolysis histories. The presence of varying levels of defects in different

PDCs dictates the relative complexity of determining their band structure. However, various experimental microstructural characterisation techniques should be useful for identifying the electronic structures of PDCs. Examples include: optical absorption measurement, X-ray photoelectron spectroscopy (for bond information). They could provide critical information on the microstructural evolutions and assist the evaluations of how various factors may affect the relative permittivity as well as dielectric loss of polymer derived ceramics, which are crucial indicators of the practical applicability of these materials for future applications.

(3) The aims of studying the electronic as well as the dielectric properties of PDCs are to have more precise and dependable controls for practical sensing applications. It is therefore imperative to conduct further investigations on the integration and packaging processes of the sensing materials (i.e., PDCs) into an integral system. The reliability and accuracy of the sensing system first depends on the innate microstructures of the PDC sensing material. From a holistic scientific point of view, the materials processing will have fundamental effects on the performance of PDCs, which requires further investigations as well as future explorations of the applicability of novel processing techniques.

(b).

The filtration / selective separation properties of 2D layers-based membranes are just beginning to gain substantial research attentions, and the practical applications are still in its infancy. Significant endeavors and discoveries await in developing device-level / large-scale applications of them.

(1). As a fundamental aspect of research and development, viable methods for the growth, transfer and integration of large-area 2D membranes are vital for the implementations of 2D

layers-based desalination devices / equipment. Most importantly, the long-term durability as well as defect-free integration and operations still require extensive investigations.

(2). As a novel type of nanomaterials, the long-term immunological bio-compatibility, toxicology, and bio-persistence of 2D materials shall be established via intensive research efforts to ensure the health aspects are addressed properly.

(3). Another potential avenue for future investigations would be the evaluation of controlled pore size generations to produce nanopores with desired sizes to meet the needs of selective filtrations. Detailed studies are required to fine-tune the operational procedures and parameters for optimal nanopore size distributions.

APPENDIX: COPYRIGHT PERMISSIONS

CHAPTER 3

CHAPTER 4

Figure 2 and Figure 4

Copyright Clearance Center RightsLink®

My Orders | My Library | My Profile | Welcome h.li@knights.ucf.edu Log out | Help

My Orders > Orders > All Orders

License Details

This Agreement between University of Central Florida -- Hao Li ("You") and John Wiley and Sons ("John Wiley and Sons") consists of your license details and the terms and conditions provided by John Wiley and Sons and Copyright Clearance Center.

Print Copy

License Number	4710360985939
License date	Nov 15, 2019
Licensed Content Publisher	John Wiley and Sons
Licensed Content Publication	Journal of the American Ceramic Society
Licensed Content Title	Polymer-Derived Ceramics: 40 Years of Research and Innovation in Advanced Ceramics
Licensed Content Author	Gian Domenico Sorarù, Ralf Riedel, Gabriela Mera, et al
Licensed Content Date	Jun 18, 2010
Licensed Content Volume	93
Licensed Content Issue	7
Licensed Content Pages	33
Type of Use	Dissertation/Thesis
Requestor type	University/Academic
Format	Print and electronic
Portion	Figure/table
Number of figures/tables	2
Will you be translating?	No
Title of your thesis / dissertation	INTERFACIAL BEHAVIOR IN POLYMER DERIVED CERAMICS AND SALT WATER PURIFICATION VIA 2D MOS2
Expected completion date	Nov 2019
Expected size (number of pages)	150
Original Wiley figure/table number(s)	Figure 2 and Figure 6

Figure 6, Figure 7, Figure 8, and Figure 9

Copyright Clearance Center Marketplace™

Royal Society of Chemistry - License Terms and Conditions

This is a License Agreement between Hao Li ("You") and Royal Society of Chemistry ("Publisher") provided by Copyright Clearance Center ("CCC"). The license consists of your order details, the terms and conditions provided by Royal Society of Chemistry, and the CCC terms and conditions.

All payments must be made in full to CCC.

Order Date	15-Nov-2019	Type of Use	Republish in a thesis/dissertation
Order license ID	1004063-1	Publisher	Royal Society of Chemistry
ISSN	2050-7496	Portion	Chart/graph/table/figure

LICENSED CONTENT

Publication Title	Journal of materials chemistry. A, Materials for energy and sustainability	Country	United Kingdom of Great Britain and Northern Ireland
Author/Editor	Royal Society of Chemistry (Great Britain)	Rightsholder	Royal Society of Chemistry
Date	12/31/2012	Publication Type	e-Journal
Language	English	URL	http://pubs.rsc.org/en/journals/journaliss...

REQUEST DETAILS

Portion Type	Chart/graph/table/figure	Distribution	Worldwide
Number of charts / graphs / tables / figures requested	4	Translation	Original language of publication
Format (select all that apply)	Electronic	Copies for the disabled?	No
Who will republish the content?	Academic institution	Minor editing privileges?	No
Duration of Use	Life of current edition	Incidental promotional use?	No
Lifetime Unit Quantity	Up to 499	Currency	USD
Rights Requested	Main product		

Figure 10 and Figure 11

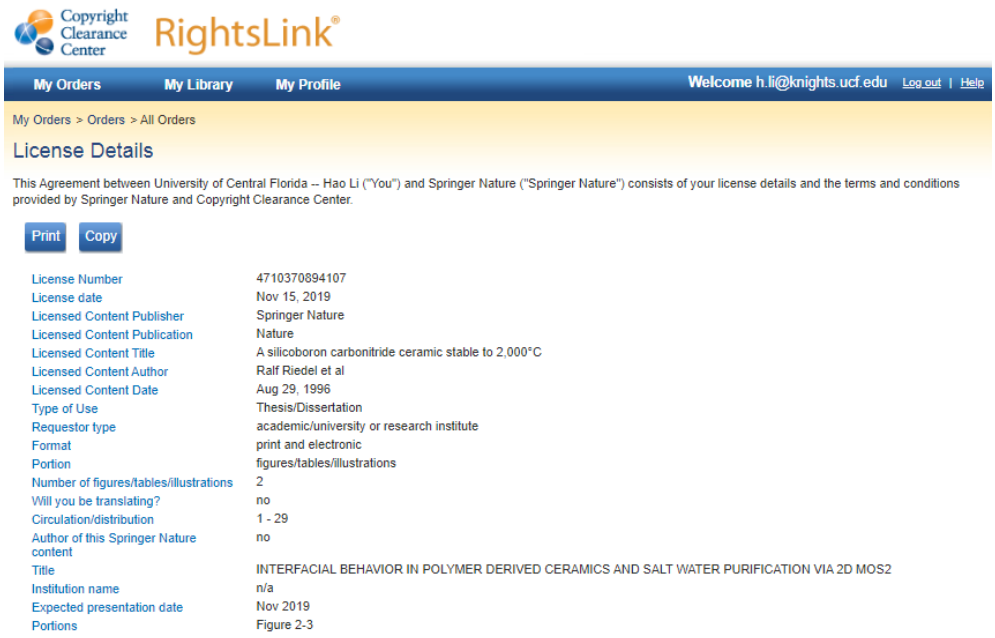

Copyright Clearance Center RightsLink®

My Orders | My Library | My Profile | Welcome h.li@knights.ucf.edu Log out | Help

My Orders > Orders > All Orders

License Details

This Agreement between University of Central Florida -- Hao Li ("You") and Springer Nature ("Springer Nature") consists of your license details and the terms and conditions provided by Springer Nature and Copyright Clearance Center.

Print Copy

License Number	4710370894107
License date	Nov 15, 2019
Licensed Content Publisher	Springer Nature
Licensed Content Publication	Nature
Licensed Content Title	A silicoboron carbonitride ceramic stable to 2,000°C
Licensed Content Author	Ralf Riedel et al
Licensed Content Date	Aug 29, 1996
Type of Use	Thesis/Dissertation
Requestor type	academic/university or research institute
Format	print and electronic
Portion	figures/tables/illustrations
Number of figures/tables/illustrations	2
Will you be translating?	no
Circulation/distribution	1 - 29
Author of this Springer Nature content	no
Title	INTERFACIAL BEHAVIOR IN POLYMER DERIVED CERAMICS AND SALT WATER PURIFICATION VIA 2D MOS2
Institution name	n/a
Expected presentation date	Nov 2019
Portions	Figure 2-3

Figure 12

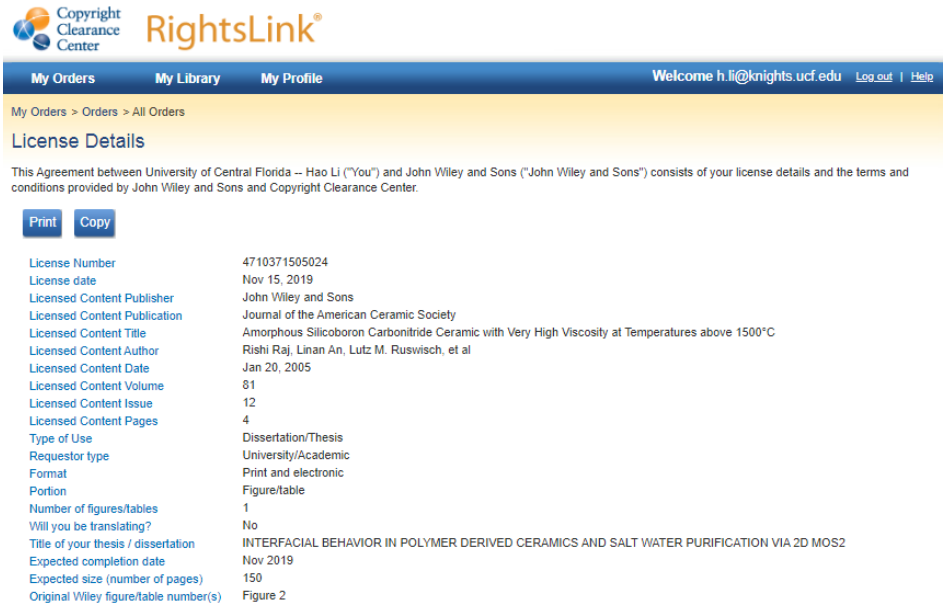

Copyright Clearance Center RightsLink®

My Orders | My Library | My Profile | Welcome h.li@knights.ucf.edu Log out | Help

My Orders > Orders > All Orders

License Details

This Agreement between University of Central Florida -- Hao Li ("You") and John Wiley and Sons ("John Wiley and Sons") consists of your license details and the terms and conditions provided by John Wiley and Sons and Copyright Clearance Center.

Print Copy

License Number	4710371505024
License date	Nov 15, 2019
Licensed Content Publisher	John Wiley and Sons
Licensed Content Publication	Journal of the American Ceramic Society
Licensed Content Title	Amorphous Silicoboron Carbonitride Ceramic with Very High Viscosity at Temperatures above 1500°C
Licensed Content Author	Rishi Raj, Linan An, Lutz M. Ruswisch, et al
Licensed Content Date	Jan 20, 2005
Licensed Content Volume	81
Licensed Content Issue	12
Licensed Content Pages	4
Type of Use	Dissertation/Thesis
Requestor type	University/Academic
Format	Print and electronic
Portion	Figure/table
Number of figures/tables	1
Will you be translating?	No
Title of your thesis / dissertation	INTERFACIAL BEHAVIOR IN POLYMER DERIVED CERAMICS AND SALT WATER PURIFICATION VIA 2D MOS2
Expected completion date	Nov 2019
Expected size (number of pages)	150
Original Wiley figure/table number(s)	Figure 2

Figure 13 and Figure 14

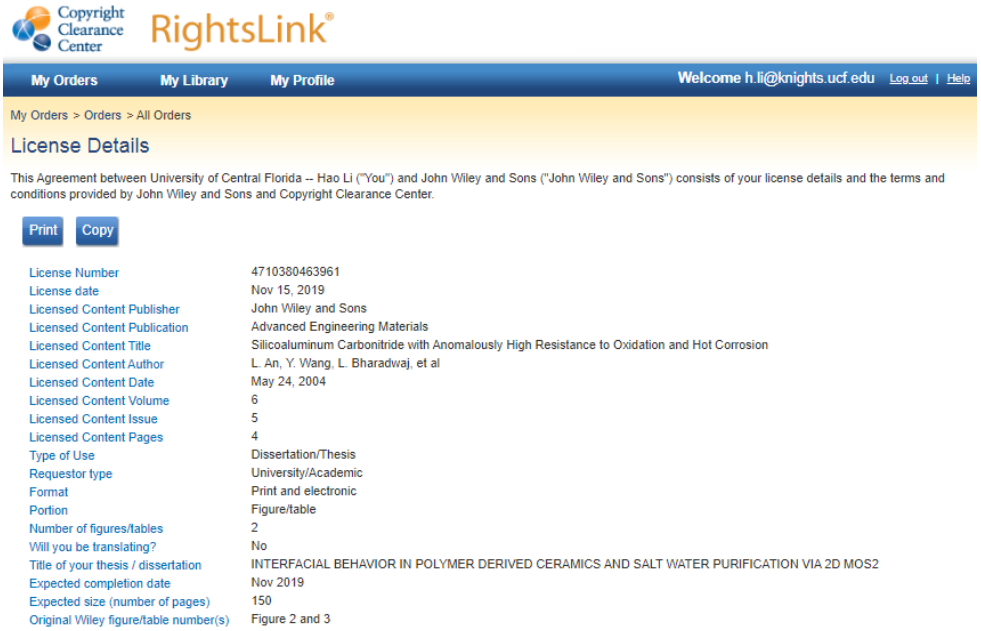

Copyright Clearance Center RightsLink®

My Orders | My Library | My Profile | Welcome h.li@knights.ucf.edu Log out | Help

My Orders > Orders > All Orders

License Details

This Agreement between University of Central Florida -- Hao Li ("You") and John Wiley and Sons ("John Wiley and Sons") consists of your license details and the terms and conditions provided by John Wiley and Sons and Copyright Clearance Center.

Print Copy

License Number	4710380463961
License date	Nov 15, 2019
Licensed Content Publisher	John Wiley and Sons
Licensed Content Publication	Advanced Engineering Materials
Licensed Content Title	Silicoaluminum Carbonitride with Anomalously High Resistance to Oxidation and Hot Corrosion
Licensed Content Author	L. An, Y. Wang, L. Bharadwaj, et al
Licensed Content Date	May 24, 2004
Licensed Content Volume	6
Licensed Content Issue	5
Licensed Content Pages	4
Type of Use	Dissertation/Thesis
Requestor type	University/Academic
Format	Print and electronic
Portion	Figure/table
Number of figures/tables	2
Will you be translating?	No
Title of your thesis / dissertation	INTERFACIAL BEHAVIOR IN POLYMER DERIVED CERAMICS AND SALT WATER PURIFICATION VIA 2D MOS2
Expected completion date	Nov 2019
Expected size (number of pages)	150
Original Wiley figure/table number(s)	Figure 2 and 3

Figure 15

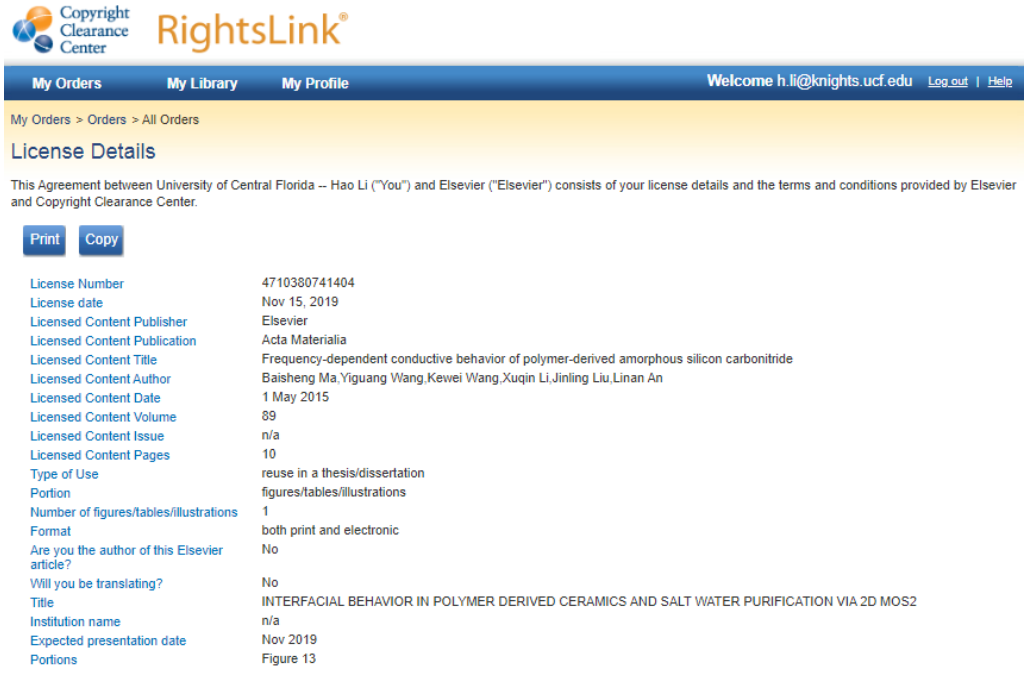

Copyright Clearance Center RightsLink®

My Orders | My Library | My Profile | Welcome h.li@knights.ucf.edu Log out | Help

My Orders > Orders > All Orders

License Details

This Agreement between University of Central Florida -- Hao Li ("You") and Elsevier ("Elsevier") consists of your license details and the terms and conditions provided by Elsevier and Copyright Clearance Center.

Print Copy

License Number	4710380741404
License date	Nov 15, 2019
Licensed Content Publisher	Elsevier
Licensed Content Publication	Acta Materialia
Licensed Content Title	Frequency-dependent conductive behavior of polymer-derived amorphous silicon carbonitride
Licensed Content Author	Baisheng Ma,Yiguang Wang,Kewei Wang,Xuqin Li,Jinling Liu,Linan An
Licensed Content Date	1 May 2015
Licensed Content Volume	89
Licensed Content Issue	n/a
Licensed Content Pages	10
Type of Use	reuse in a thesis/dissertation
Portion	figures/tables/illustrations
Number of figures/tables/illustrations	1
Format	both print and electronic
Are you the author of this Elsevier article?	No
Will you be translating?	No
Title	INTERFACIAL BEHAVIOR IN POLYMER DERIVED CERAMICS AND SALT WATER PURIFICATION VIA 2D MOS2
Institution name	n/a
Expected presentation date	Nov 2019
Portions	Figure 13

LIST OF REFERENCES

1 Riedel, R., Mera, G., Hauser, R. & Klonczynski, A. Silicon-based polymer-derived ceramics: synthesis properties and applications-a review dedicated to Prof. Dr. Fritz Aldinger on the occasion of his 65th birthday. *Journal of the Ceramic Society of Japan* **114**, 425-444 (2006).

2 Colombo, P., Mera, G., Riedel, R. & Soraru, G. D. Polymer-derived ceramics: 40 years of research and innovation in advanced ceramics. *Journal of the American Ceramic Society* **93**, 1805-1837 (2010).

3 Shao, G. *Development Of Polymer Derived Sialcn Ceramic And Its Applications For High-temperature Sensors*, (2013).

4 Biebl, M., Brandl, G. & Howe, R. in *Solid-State Sensors and Actuators, 1995 and Eurosensors IX.. Transducers' 95. The 8th International Conference on.* 80-83 (IEEE).

5 Elimelech, M. & Phillip, W. A. The Future of Seawater Desalination: Energy, Technology, and the Environment. *Science* **333**, 712-717, (2011).

6 Shannon, M. A. *et al.* Science and technology for water purification in the coming decades. *Nature* **452**, 301-311 (2008).

7 Zhao, S., Zou, L., Tang, C. Y. & Mulcahy, D. Recent developments in forward osmosis: opportunities and challenges. *Journal of membrane science* **396**, 1-21 (2012).

8 Fritzmann, C., Löwenberg, J., Wintgens, T. & Melin, T. State-of-the-art of reverse osmosis desalination. *Desalination* **216**, 1-76 (2007).

9 Lee, K. P., Arnot, T. C. & Mattia, D. A review of reverse osmosis membrane materials for desalination—development to date and future potential. *Journal of Membrane Science* **370**, 1-22 (2011).

10 Amy, G. *et al.* Membrane-based seawater desalination: Present and future prospects. *Desalination* **401**, 16-21 (2017).

11 Bhimanapati, G. R. *et al.* Recent advances in two-dimensional materials beyond graphene. *ACS nano* **9**, 11509-11539 (2015).

12 Zhu, J. *et al.* The rapid emergence of two-dimensional nanomaterials for high-performance separation membranes. *Journal of Materials Chemistry A* **6**, 3773-3792 (2018).

13 Liu, G., Jin, W. & Xu, N. Two-dimensional-material membranes: a new family of high-performance separation membranes. *Angewandte Chemie International Edition* **55**, 13384-13397 (2016).

14 Ramanathan, A., Aqra, M. & Al-Rawajfeh, A. Recent advances in 2D nanopores for desalination. *Environmental Chemistry Letters*, 1-15 (2018).

15 Dervin, S., Dionysiou, D. D. & Pillai, S. C. 2D nanostructures for water purification: graphene and beyond. *Nanoscale* **8**, 15115-15131 (2016).

16 Aghigh, A. *et al.* Recent advances in utilization of graphene for filtration and desalination of water: a review. *Desalination* **365**, 389-397 (2015).

17 Mahmoud, K. A., Mansoor, B., Mansour, A. & Khraisheh, M. Functional graphene nanosheets: The next generation membranes for water desalination. *Desalination* **356**, 208-225 (2015).

18 Goh, P. & Ismail, A. Graphene-based nanomaterial: The state-of-the-art material for cutting edge desalination technology. *Desalination* **356**, 115-128 (2015).

19 Danda, G. & Drndić, M. Two-dimensional nanopores and nanoporous membranes for ion and molecule transport. *Current opinion in biotechnology* **55**, 124-133 (2019).

20 Li, M.-N. *et al.* Forward osmosis membranes modified with laminar MoS 2 nanosheet to improve desalination performance and antifouling properties. *Desalination* **436**, 107-113 (2018).

21 Ghim, D., Jiang, Q., Cao, S., Singamaneni, S. & Jun, Y.-S. Mechanically interlocked 1T/2H phases of MoS2 nanosheets for solar thermal water purification. *Nano energy* **53**, 949-957 (2018).

22 Sun, L. *et al.* Ultrafast molecule separation through layered WS2 nanosheet membranes. *ACS nano* **8**, 6304-6311 (2014).

23 Hegab, H. M. & Zou, L. Graphene oxide-assisted membranes: fabrication and potential applications in desalination and water purification. *Journal of Membrane Science* **484**, 95-106 (2015).

24 Li, X. *et al.* Graphene oxide-based efficient and scalable solar desalination under one sun with a confined 2D water path. *Proceedings of the National Academy of Sciences* **113**, 13953-13958 (2016).

25 Mi, B. Graphene oxide membranes for ionic and molecular sieving. *Science* **343**, 740-742 (2014).

26 Joshi, R. *et al.* Precise and ultrafast molecular sieving through graphene oxide membranes. *Science* **343**, 752-754 (2014).

27 Rangnekar, N., Mittal, N., Elyassi, B., Caro, J. & Tsapatsis, M. Zeolite membranes–a review and comparison with MOFs. *Chemical Society Reviews* **44**, 7128-7154 (2015).

28 Wibowo, E., Rokhmat, M. & Abdullah, M. Reduction of seawater salinity by natural zeolite (Clinoptilolite): adsorption isotherms, thermodynamics and kinetics. *Desalination* **409**, 146-156 (2017).

29 Zhu, B. *et al.* Application of robust MFI-type zeolite membrane for desalination of saline wastewater. *Journal of Membrane Science* **475**, 167-174 (2015).

30 Jamali, S. H., Vlugt, T. J. & Lin, L.-C. Atomistic understanding of zeolite nanosheets for water desalination. *The Journal of Physical Chemistry C* **121**, 11273-11280 (2017).

31 Ou, R. *et al.* Water Desalination: Thermoresponsive Amphoteric Metal–Organic Frameworks for Efficient and Reversible Adsorption of Multiple Salts from Water (Adv. Mater. 34/2018). *Advanced Materials* **30**, 1870256 (2018).

32 Denny Jr, M. S., Moreton, J. C., Benz, L. & Cohen, S. M. Metal–organic frameworks for membrane-based separations. *Nature Reviews Materials* **1**, 16078 (2016).

33 Liang, W. *et al.* Linking defects, hierarchical porosity generation and desalination performance in metal–organic frameworks. *Chemical Science* **9**, 3508-3516 (2018).

34 Kadhom, M. & Deng, B. Metal-organic frameworks (MOFs) in water filtration membranes for desalination and other applications. *Applied Materials Today* **11**, 219-230 (2018).

35 Chhowalla, M. *et al.* The chemistry of two-dimensional layered transition metal dichalcogenide nanosheets. *Nature chemistry* **5**, 263 (2013).

36 Chou, S. S. *et al.* Chemically Exfoliated MoS2 as Near-Infrared Photothermal Agents. *Angewandte Chemie* **125**, 4254-4258 (2013).

37 Liu, T. *et al.* Drug delivery with PEGylated MoS2 nano-sheets for combined photothermal and chemotherapy of cancer. *Advanced Materials* **26**, 3433-3440 (2014).

38 Zhou, W. *et al.* Intrinsic structural defects in monolayer molybdenum disulfide. *Nano letters* **13**, 2615-2622 (2013).

39 Banhart, F., Kotakoski, J. & Krasheninnikov, A. V. Structural defects in graphene. *ACS nano* **5**, 26-41 (2010).

40 Najmaei, S. *et al.* Vapour phase growth and grain boundary structure of molybdenum disulphide atomic layers. *Nature materials* **12**, 754 (2013).

41 Kou, J. *et al.* Nanoporous two-dimensional MoS 2 membranes for fast saline solution purification. *Physical Chemistry Chemical Physics* **18**, 22210-22216 (2016).

42 Fritz, G. & Raabe, B. Bildung siliciumorganischer verbindungen. V. Die thermische zersetzung von Si (CH3) 4 und Si (C2H5) 4. *Zeitschrift für anorganische und allgemeine Chemie* **286**, 149-167 (1956).

43 Yajima, S., Hayashi, J. & Omori, M. Continuous silicon carbide fiber of high tensile strength. *Chemistry Letters* **4**, 931-934 (1975).

44 Bernard, S., Fiaty, K., Cornu, D., Miele, P. & Laurent, P. Kinetic modeling of the polymer-derived ceramics route: investigation of the thermal decomposition kinetics of poly [B-(methylamino) borazine] precursors into boron nitride. *The Journal of Physical Chemistry B* **110**, 9048-9060 (2006).

45 Riedel, R., Passing, G., Schönfelder, H. & Brook, R. Synthesis of dense silicon-based ceramics at low temperatures. *Nature* **355**, 714-717 (1992).

46 Ryu, H. Y., Wang, Q. & Raj, R. Ultrahigh-Temperature Semiconductors Made from Polymer-Derived Ceramics. *Journal of the American ceramic society* **93**, 1668-1676 (2010).

47 Zhang, L. *et al.* A silicon carbonitride ceramic with anomalously high piezoresistivity. *Journal of the American Ceramic Society* **91**, 1346-1349 (2008).

48 Ramakrishnan, P. *et al.* Silicoboron–carbonitride ceramics: A class of high-temperature, dopable electronic materials. *Applied Physics Letters* **78**, 3076-3078 (2001).

49 Riedel, R. *et al.* A silicoboron carbonitride ceramic stable to 2,000 °C. *Nature* **382**, 796-798 (1996).

50 Schawaller, D., Clauß, B. & Buchmeiser, M. R. Ceramic filament fibers–a review. *Macromolecular Materials and Engineering* **297**, 502-522 (2012).

51 An, L. *et al.* Carbon-nanotube-reinforced polymer-derived ceramic composites. *Advanced Materials* **16**, 2036-2040 (2004).

52 Chen, Y. *et al.* Self-assembled carbon–silicon carbonitride nanocomposites: high-performance anode materials for lithium-ion batteries. *Journal of Materials Chemistry* **21**, 18186-18190 (2011).

53 Bernard, S. & Miele, P. Ordered mesoporous polymer-derived ceramics and their processing into hierarchically porous boron nitride and silicoboron carbonitride monoliths. *New Journal of Chemistry* **38**, 1923-1931 (2014).

54 Liew, L. *et al.* Ceramic MEMS. *American Ceramic Society Bulletin* **80**, 25 (2000).

55 Birot, M., Pillot, J.-P. & Dunogues, J. Comprehensive chemistry of polycarbosilanes, polysilazanes, and polycarbosilazanes as precursors of ceramics. *Chemical reviews* **95**, 1443-1477 (1995).

56 Laine, R. M., Blum, Y. D., Tse, D. & Glaser, R. (ACS Publications, 1988).

57 Cubbon, R. *Polymeric precursors for ceramic materials*. Vol. 76 (iSmithers Rapra Publishing, 1994).

58 An, L. *et al.* Silicoaluminum carbonitride with anomalously high resistance to oxidation and hot corrosion. *Advanced Engineering Materials* **6**, 337-340 (2004).

59 Funayama, O., Tashiro, Y., Kamo, A., Okumura, M. & Isoda, T. Conversion mechanism of perhydropolysilazane into silicon nitride-based ceramics. *Journal of materials science* **29**, 4883-4888 (1994).

60 Ishikawa, T., Kohtoku, Y., Kumagawa, K., Yamamura, T. & Nagasawa, T. High-strength alkali-resistant sintered SiC fibre stable to 2,200 C. *Nature* **391**, 773-775 (1998).

61 Rocha, R. M. d., Greil, P., Bressiani, J. C. & Bressiani, A. H. d. A. Complex-shaped ceramic composites obtained by machining compact polymer-filler mixtures. *Materials Research* **8**, 191-196 (2005).

62 Otoishi, S. & Tange, Y. Growth rate and morphology of silicon carbide whiskers from polycarbosilane. *Journal of crystal growth* **200**, 467-471 (1999).

63 Zhang, T., Evans, J. & Woodthorpe, J. Injection moulding of silicon carbide using an organic vehicle based on a preceramic polymer. *Journal of the European Ceramic Society* **15**, 729-734 (1995).

64 Evans, J. Seventy ways to make ceramics. *Journal of the European Ceramic Society* **28**, 1421-1432 (2008).

65 Harshe, R., Balan, C. & Riedel, R. Amorphous Si (Al) OC ceramic from polysiloxanes: bulk ceramic processing, crystallization behavior and applications. *Journal of the European Ceramic Society* **24**, 3471-3482 (2004).

66 Janakiraman, N. & Aldinger, F. Fabrication and characterization of fully dense Si–C–N ceramics from a poly (ureamethylvinyl) silazane precursor. *Journal of the European Ceramic Society* **29**, 163-173 (2009).

67 Friedel, T., Travitzky, N., Niebling, F., Scheffler, M. & Greil, P. Fabrication of polymer derived ceramic parts by selective laser curing. *Journal of the European Ceramic Society* **25**, 193-197 (2005).

68 Taki, T., Maeda, S., Okamura, K., Sato, M. & Matsuzawa, T. Oxidation curing mechanism of polycarbosilane fibres by solid-state29Si high-resolution NMR. *Journal of materials science letters* **6**, 826-828 (1987).

69 Ly, H., Taylor, R., Day, R. & Heatley, F. Conversion of polycarbosilane (PCS) to SiC-based ceramic Part 1. Characterisation of PCS and curing products. *Journal of Materials science* **36**, 4037-4043 (2001).

70 Narisawa, M. *et al.* Use of blended precursors of poly (vinylsilane) in polycarbosilane for silicon carbide fiber synthesis with radiation curing. *Journal of the American Ceramic Society* **82**, 1045-1051 (1999).

71 Liew, L.-A. *et al.* Fabrication of SiCN MEMS by photopolymerization of pre-ceramic polymer. *Sensors and Actuators A: Physical* **95**, 120-134 (2002).

72 Pham, T. A., Kim, P., Kwak, M., Suh, K. Y. & Kim, D.-P. Inorganic polymer photoresist for direct ceramic patterning by photolithography. *Chemical Communications*, 4021-4023 (2007).

73 Schulz, M. *et al.* Cross Linking Behavior of Preceramic Polymers Effected by UV-and Synchrotron Radiation. *Advanced Engineering Materials* **6**, 676-680 (2004).

74 Liew, L.-A. *et al.* in *Micro Electro Mechanical Systems, 2001. MEMS 2001. The 14th IEEE International Conference on.* 86-89 (IEEE).

75 Cordelair, J. & Greil, P. Electrical characterization of polymethylsiloxane/MoSi2-derived composite ceramics. *Journal of the American Ceramic Society* **84**, 2256-2259 (2001).

76 Biasetto, L., Francis, A., Palade, P., Principi, G. & Colombo, P. Polymer-derived microcellular SiOC foams with magnetic functionality. *Journal of materials science* **43**, 4119-4126 (2008).

77 Greil, P. & Seibold, M. Modelling of dimensional changes during polymer-ceramic conversion for bulk component fabrication. *Journal of materials science* **27**, 1053-1060 (1992).

78 Kim, Y.-W., Kim, S.-h., Kim, H.-D. & Park, C. B. Processing of closed-cell silicon oxycarbide foams from a preceramic polymer. *Journal of Materials Science* **39**, 5647-5652 (2004).

79 Blum, Y. D., Schwartz, K. B. & Laine, R. M. Preceramic polymer pyrolysis. *Journal of materials science* **24**, 1707-1718 (1989).

80 Chan, H. N. *et al.* Direct, one-step molding of 3D-printed structures for convenient fabrication of truly 3D PDMS microfluidic chips. *Microfluidics and nanofluidics* **19**, 9-18 (2015).

81 Zocca, A. *et al.* SiOC ceramics with ordered porosity by 3D-printing of a preceramic polymer. *Journal of Materials Research* **28**, 2243-2252 (2013).

82 Tian, Y., Shao, G., Wang, X. & An, L. Fabrication of nano-scaled polymer-derived SiAlCN ceramic components using focused ion beam. *Journal of Micromechanics and Microengineering* **23**, 095035 (2013).

83 Eckel, Z. C. *et al.* Additive manufacturing of polymer-derived ceramics. *Science* **351**, 58-62 (2016).

84 Bouyer, E., Schiller, G., Müller, M. & Henne, R. Thermal plasma chemical vapor deposition of Si-based ceramic coatings from liquid precursors. *Plasma Chemistry and Plasma Processing* **21**, 523-546 (2001).

85 Krüger, U. D. & Ullrich, R. (Google Patents, 2006).

86 Colombo, P., Martucci, A., Fogato, O. & Villoresi, P. Silicon carbide films by laser pyrolysis of polycarbosilane. *Journal of the American Ceramic Society* **84**, 224-226 (2001).

87 Tsukuda, S. *et al.* Fabrication of nanowires using high-energy ion beams. *The Journal of Physical Chemistry B* **108**, 3407-3409 (2004).

88 Pivin, J. & Colombo, P. Ceramic coatings by ion irradiation of polycarbosilanes and polysiloxanes: Part I Conversion mechanism. *Journal of materials science* **32**, 6163-6173 (1997).

89 Pivin, J. & Colombo, P. Ceramic coatings by ion irradiation of polycarbosilanes and polysiloxanes: Part II Hardness and thermochemical stability. *Journal of materials science* **32**, 6175-6182 (1997).

90 Pivin, J. C., Colombo, P. & Sorarù, G. D. Comparison of Ion Irradiation Effects in Silicon-Based Preceramic Thin Films. *Journal of the American Ceramic Society* **83**, 713-720 (2000).

91 Bill, J. *et al.* Investigations into the structural evolution of amorphous Si-CN ceramics from precursors. *Zeitschrift für Metallkunde* **91**, 335-351 (2000).

92 Kleebe, H. J. Microstructure and Stability of Polymer-Derived Ceramics; the Si–C–N System. *physica status solidi (a)* **166**, 297-313 (1998).

93 Kleebe, H. J., Störmer, H., Trassl, S. & Ziegler, G. Thermal stability of SiCN ceramics studied by spectroscopy and electron microscopy. *Applied organometallic chemistry* **15**, 858-866 (2001).

94 Mera, G., Tamayo, A., Nguyen, H., Sen, S. & Riedel, R. Nanodomain Structure of Carbon-Rich Silicon Carbonitride Polymer-Derived Ceramics. *Journal of the American Ceramic Society* **93**, 1169-1175 (2010).

95 Wang, Y. *et al.* Effect of thermal initiator concentration on the electrical behavior of polymer-derived amorphous silicon carbonitrides. *Journal of the American Ceramic Society* **91**, 3971-3975 (2008).

96 Jiang, T., Wang, Y., Wang, Y., Orlovskaya, N. & An, L. Quantitative raman analysis of free carbon in polymer-derived ceramics. *Journal of the American Ceramic Society* **92**, 2455-2458 (2009).

97 Störmer, H., Kleebe, H.-J. & Ziegler, G. Metastable SiCN glass matrices studied by energy-filtered electron diffraction pattern analysis. *Journal of Non-Crystalline Solids* **353**, 2867-2877 (2007).

98 Mera, G., Riedel, R., Poli, F. & Müller, K. Carbon-rich SiCN ceramics derived from phenyl-containing poly (silylcarbodiimides). *Journal of the European Ceramic Society* **29**, 2873-2883 (2009).

99 Gao, Y. *et al.* Processing route dramatically influencing the nanostructure of carbon-rich SiCN and SiBCN polymer-derived ceramics. Part I: Low temperature thermal transformation. *Journal of the European Ceramic Society* **32**, 1857-1866 (2012).

100 Mera, G., Navrotsky, A., Sen, S., Kleebe, H.-J. & Riedel, R. Polymer-derived SiCN and SiOC ceramics–structure and energetics at the nanoscale. *Journal of Materials Chemistry A* **1**, 3826-3836 (2013).

101 Saha, A., Raj, R. & Williamson, D. L. A model for the nanodomains in polymer-derived SiCO. *Journal of the American Ceramic Society* **89**, 2188-2195 (2006).

102 Riedel, R. *et al.* Piezoresistive effect in SiOC ceramics for integrated pressure sensors. *Journal of the American Ceramic Society* **93**, 920-924 (2010).

103 Haluschka, C., Engel, C. & Riedel, R. Silicon carbonitride ceramics derived from polysilazanes Part II. Investigation of electrical properties. *Journal of the European Ceramic Society* **20**, 1365-1374 (2000).

104 Ma, C. *et al.* Temperature dependent AC electric conduction of polymer-derived SiAlCN ceramics. *Ceramics International* **44**, 8461-8466 (2018).

105 Chen, Y., Yang, X., Cao, Y. & An, L. Effect of pyrolysis temperature on the electric conductivity of polymer-derived silicoboron carbonitride. *Journal of the European Ceramic Society* **34**, 2163-2167 (2014).

106 Cao, Y., Yang, X. & An, L. Electric conductivity and microstructure evolution of polymer-derived SiAlCO ceramics. *Ceramics International* **42**, 4033-4038 (2016).

107 Zimmermann, A., Bauer, A., Christ, M., Cai, Y. & Aldinger, F. High-temperature deformation of amorphous Si–C–N and Si–B–C–N ceramics derived from polymers. *Acta materialia* **50**, 1187-1196 (2002).

108 Riedel, R., Ruswisch, L. M., An, L. & Raj, R. Amorphous silicoboron carbonitride ceramic with very high viscosity at temperatures above 1500 C. *Journal of the American Ceramic Society* **81**, 3341-3344 (1998).

109 Wang, Y., Fan, Y., Zhang, L., Zhang, W. & An, L. Polymer-derived SiAlCN ceramics resist oxidation at 1400 C. *Scripta materialia* **55**, 295-297 (2006).

110 Wang, Y. *et al.* Oxidation of Polymer-Derived SiAlCN Ceramics. *Journal of the American Ceramic Society* **88**, 3075-3080 (2005).

111 Wang, Y., Fei, W. & An, L. Oxidation/Corrosion of Polymer-Derived SiAlCN Ceramics in Water Vapor. *Journal of the American Ceramic Society* **89**, 1079-1082 (2006).

112 Walter, S., Soraru, G., Brequel, H. & Enzo, S. Microstructural and mechanical characterization of sol gel-derived Si–O–C glasses. *Journal of the European Ceramic Society* **22**, 2389-2400 (2002).

113 Liu, Y. *et al.* Application of microforging to SiCN MEMS fabrication. *Sensors and Actuators A: Physical* **95**, 143-151 (2002).

114 Ma, B. *et al.* Frequency-dependent conductive behavior of polymer-derived amorphous silicon carbonitride. *Acta Materialia* **89**, 215-224 (2015).

115 Wang, K., Ma, B., Wang, Y. & An, L. Complex Impedance Spectra of Polymer-Derived Silicon Oxycarbides. *Journal of the American Ceramic Society* **96**, 1363-1365 (2013).

116 Cao, Y., Gao, Y. & An, L. Impedance spectroscopy study on polymer-derived amorphous SiAlCO. *Journal of the American Ceramic Society* **100**, 1481-1485 (2017).

117 Dang, Z.-M. *et al.* Fundamentals, processes and applications of high-permittivity polymer–matrix composites. *Progress in Materials Science* **57**, 660-723 (2012).

118 Li, X., Chen, F. & Wang, Y. Colossal dielectric constant and interfacial charge polarization in a polymer-derived amorphous silicon carbonitride. *Ceramics International* **43**, 11623-11626 (2017).

119 Li, X. & Wang, Y. Complex impedance study on polymer-derived amorphous silicon carbonitride. *Ceramics International* **43**, 13560-13564 (2017).

120 Li, X., Cao, Y., Ma, B. & Wang, Y. Interface characteristics of polymer-derived amorphous SiCN ceramics investigated by impedance spectroscopy under direct current bias. *Ceramics International* **44**, 2074-2076 (2018).

121 Colinge, J.-P. & Colinge, C. A. *Physics of semiconductor devices*. (Springer Science & Business Media, 2005).

122 Saha, A., Shah, S. R., Raj, R. & Russek, S. E. Polymer-derived SiCN composites with magnetic properties. *Journal of materials research* **18**, 2549-2551 (2003).

123 Sun, Q. *et al.* Nanocluster-containing mesoporous magnetoceramics from hyperbranched organometallic polymer precursors. *Chemistry of materials* **12**, 2617-2624 (2000).

124 Kolář, F., Machovič, V. & Svitilova, J. Cobalt-containing silicon oxycarbide glasses derived from poly [methyl (phenyl)] siloxane and cobalt phthalate. *Journal of non-crystalline solids* **352**, 2892-2896 (2006).

125 Loner, S. Vetri ossicarburi trasparenti. *Tesi Di Laurea in Ingegneria Dei Materiali* (2001).

126 Zhang, Y., Quaranta, A. & Soraru, G. D. Synthesis and luminescent properties of novel Eu2+-doped silicon oxycarbide glasses. *Optical Materials* **24**, 601-605 (2004).

127 Karakuscu, A., Guider, R., Pavesi, L. & Soraru, G. D. White luminescence from sol–gel-derived SiOC thin films. *Journal of the American Ceramic Society* **92**, 2969-2974 (2009).

128 Menapace, I. *et al.* Luminescence of heat-treated silicon-based polymers: promising materials for LED applications. *Journal of Materials Science* **43**, 5790-5796 (2008).

129 Ferraioli, L., Ahn, D., Saha, A., Pavesi, L. & Raj, R. Intensely Photoluminescent Pseudo-Amorphous SiliconOxyCarboNitride Polymer–Ceramic Hybrids. *Journal of the American Ceramic Society* **91**, 2422-2424 (2008).

130 Soraru, G. D. *et al.* Chemical durability of silicon oxycarbide glasses. *Journal of the American Ceramic Society* **85**, 1529-1536 (2002).

131 Baldus, H., Passing, G., Sporn, D. & Thieraf, A. Si-B-(N, C) a new ceramic material for high performance applications. (American Ceramic Society, Westerville, OH (United States), 1995).

132 Saha, A., Shah, S. R. & Raj, R. Oxidation behavior of SiCN–ZrO2 fiber prepared from alkoxide-modified silazane. *Journal of the American Ceramic Society* **87**, 1556-1558 (2004).

133 Badzian, A., Badzian, T., Drawl, W. & Roy, R. Silicon carbonitride: a rival to cubic boron nitride. *Diamond and related materials* **7**, 1519-1525 (1998).

134 Zeigmeister. *Development of a mechanical and oxidation protection for ceramic substrates*, Darmstadt University of Technology, (2003).

135 Väolger. TU Darmstadt, (2002).

136 Schulz, M. Polymer derived ceramics in MEMS/NEMS–a review on production processes and application. *Advances in applied ceramics* **108**, 454-460 (2009).

137 Feiertag, G. *et al.* Fabrication of photonic crystals by deep x-ray lithography. *Applied Physics Letters* **71**, 1441-1443 (1997).

138 Lee, H.-J., Yoon, T.-H. & Kim, D.-P. Fabrication of microfluidic channels derived from a UV/thermally cured preceramic polymer via a soft lithographic technique. *Microelectronic Engineering* **84**, 2892-2895 (2007).

139 Flores, O., Bordia, R. K., Nestler, D., Krenkel, W. & Motz, G. Ceramic fibers based on SiC and SiCN systems: Current research, development, and commercial status. *Advanced Engineering Materials* **16**, 621-636 (2014).

140 Nagaiah, N., Kapat, J., An, L. & Chow, L. in *Journal of Physics: Conference Series.* 458 (IOP Publishing).

141 Li, Y., Yu, Y., San, H., Wang, Y. & An, L. Wireless passive polymer-derived SiCN ceramic sensor with integrated resonator/antenna. *Applied Physics Letters* **103**, 163505 (2013).

142 Zhao, R., Shao, G., Cao, Y., An, L. & Xu, C. Temperature sensor made of polymer-derived ceramics for high-temperature applications. *Sensors and Actuators A: Physical* **219**, 58-64 (2014).

143 Leo, A., Andronenko, S., Stiharu, I. & Bhat, R. B. Characterization of thick and thin film SiCN for pressure sensing at high temperatures. *Sensors* **10**, 1338-1354 (2010).

144 Hu, L. H. & Raj, R. Semiconductive behavior of polymer-derived SiCN ceramics for hydrogen sensing. *Journal of the American Ceramic Society* **98**, 1052-1055 (2015).

145 Siskens, C. in *Membrane Science and Technology* Vol. 4 619-639 (Elsevier, 1996).

146 Jeong, B.-H. *et al.* Interfacial polymerization of thin film nanocomposites: a new concept for reverse osmosis membranes. *Journal of membrane science* **294**, 1-7 (2007).

147 Mauter, M. S. & Elimelech, M. Environmental applications of carbon-based nanomaterials. *Environmental Science & Technology* **42**, 5843-5859 (2008).

148 Suk, M. E. & Aluru, N. R. Water transport through ultrathin graphene. *The Journal of Physical Chemistry Letters* **1**, 1590-1594 (2010).

149 Xu, G.-R. *et al.* Two-dimensional (2D) nanoporous membranes with sub-nanopores in reverse osmosis desalination: Latest developments and future directions. *Desalination* **451**, 18-34 (2019).

150 Diercks, C. S. & Yaghi, O. M. The atom, the molecule, and the covalent organic framework. *Science* **355**, eaal1585 (2017).

151 Ren, C. E. *et al.* Charge-and size-selective ion sieving through Ti3C2T x MXene membranes. *The journal of physical chemistry letters* **6**, 4026-4031 (2015).

152 Köhler, M. H., Bordin, J. R. & Barbosa, M. C. 2D nanoporous membrane for cation removal from water: Effects of ionic valence, membrane hydrophobicity, and pore size. *The Journal of chemical physics* **148**, 222804 (2018).

153 Wang, Z. & Mi, B. Environmental applications of 2D molybdenum disulfide (MoS2) nanosheets. *Environmental science & technology* **51**, 8229-8244 (2017).

154 Heiranian, M., Farimani, A. B. & Aluru, N. R. Water desalination with a single-layer MoS 2 nanopore. *Nature communications* **6**, 8616 (2015).

155 Li, W., Yang, Y., Weber, J. K., Zhang, G. & Zhou, R. Tunable, strain-controlled nanoporous MoS2 filter for water desalination. *ACS nano* **10**, 1829-1835 (2016).

156 Sun, L., Huang, H. & Peng, X. Laminar MoS 2 membranes for molecule separation. *Chemical communications* **49**, 10718-10720 (2013).

157 Hirunpinyopas, W. *et al.* Desalination and nanofiltration through functionalized laminar MoS2 membranes. *ACS nano* **11**, 11082-11090 (2017).

158 Wang, Y., Jiang, T., Zhang, L. & An, L. Electron transport in polymer-derived amorphous silicon oxycarbonitride ceramics. *Journal of the American Ceramic Society* **92**, 1603-1606 (2009).

159 Terauds, K., Sanchez-Jimenez, P., Raj, R., Vakifahmetoglu, C. & Colombo, P. Giant piezoresistivity of polymer-derived ceramics at high temperatures. *Journal of the European Ceramic Society* **30**, 2203-2207 (2010).

160 Wang, Y., Zhang, L., Fan, Y., Jiang, D. & An, L. Stress-dependent piezoresistivity of tunneling-percolation systems. *Journal of materials science* **44**, 2814-2819 (2009).

161 Wang, K. *et al.* On electronic structure of polymer-derived amorphous silicon carbide ceramics. *Applied Physics Letters* **104**, 221902 (2014).

162 Cao, Y. *et al.* Giant piezoresistivity in polymer-derived amorphous SiAlCO ceramics. *Journal of materials science* **51**, 5646-5650 (2016).

163 Dhamne, A. *et al.* Polymer–ceramic conversion of liquid polyaluminasilazanes for SiAlCN ceramics. *Journal of the American Ceramic Society* **88**, 2415-2419 (2005).

164 Trassl, S., Puchinger, M., Rössler, E. & Ziegler, G. Electrical properties of amorphous SiCxNyHz-ceramics derived from polyvinylsilazane. *Journal of the European Ceramic Society* **23**, 781-789 (2003).

165 Ferrari, A. C. & Robertson, J. Interpretation of Raman spectra of disordered and amorphous carbon. *Physical review B* **61**, 14095 (2000).

166 Ferrari, A. & Robertson, J. Interpretation of Raman spectra of Amorphous and Disordered Carbons. *Phys. Rev. B* **61**, 14095 (2000).

167 Ferrari, A. & Robertson, J. Resonant Raman spectroscopy of disordered, amorphous, and diamondlike carbon. *Physical review B* **64**, 075414 (2001).

168 Trassl, S., Suttor, D., Motz, G., Rössler, E. & Ziegler, G. Structural characterisation of silicon carbonitride ceramics derived from polymeric precursors. *Journal of the European Ceramic Society* **20**, 215-225 (2000).

169 Andronenko, S. I., Stiharu, I. & Misra, S. K. Synthesis and characterization of polyureasilazane derived SiCN ceramics. *Journal of applied physics* **99**, 113907 (2006).

170 Chen, Y., Yang, X., Cao, Y., Gan, Z. & An, L. Quantitative study on structural evolutions and associated energetics in polysilazane-derived amorphous silicon carbonitride ceramics. *Acta Materialia* **72**, 22-31 (2014).

171 Wang, K., Ma, B., Li, X., Wang, Y. & An, L. Structural evolutions in polymer-derived carbon-rich amorphous silicon carbide. *The Journal of Physical Chemistry A* **119**, 552-558 (2015).

172 Adams, T. B., Sinclair, D. C. & West, A. R. Characterization of grain boundary impedances in fine-and coarse-grained Ca Cu 3 Ti 4 O 12 ceramics. *Physical review B* **73**, 094124 (2006).

173 Fernández-Hevia, D., de Frutos, J., Caballero, A. & Fernández, J. Mott–Schottky behavior of strongly pinned double Schottky barriers and characterization of ceramic varistors. *Journal of applied physics* **92**, 2890-2898 (2002).

174 Mukae, K., Tsuda, K. & Nagasawa, I. Capacitance-vs-voltage characteristics of ZnO varistors. *Journal of Applied Physics* **50**, 4475-4476 (1979).

175 Brillson, L. J. & Lu, Y. ZnO Schottky barriers and Ohmic contacts. *Journal of Applied Physics* **109**, 8 (2011).

176 Robertson, J. & O'reilly, E. Electronic and atomic structure of amorphous carbon. *Physical Review B* **35**, 2946 (1987).

177 Sze, S. M. & Ng, K. K. *Physics of semiconductor devices*. (John wiley & sons, 2006).

178 Bludau, W., Onton, A. & Heinke, W. Temperature dependence of the band gap of silicon. *Journal of Applied Physics* **45**, 1846-1848 (1974).

179 Wang, K. *et al.* Evolution in the electronic structure of polymer-derived amorphous silicon carbide. *Journal of the American Ceramic Society* **98**, 2153-2158 (2015).

180 Wang, K., Ma, B., Li, X., Wang, Y. & An, L. Effect of Pyrolysis Temperature on the Structure and Conduction of Polymer-Derived SiC. *Journal of the American Ceramic Society* **97**, 2135-2138 (2014).

181 Gao, Y. *et al.* Effect of demixing and coarsening on the energetics of poly (boro) silazane-derived amorphous Si–(B–) C–N ceramics. *Scripta Materialia* **69**, 347-350 (2013).

182 Widgeon, S. *et al.* Nanostructure and energetics of carbon-rich SiCN ceramics derived from polysilylcarbodiimides: Role of the nanodomain interfaces. *Chemistry of Materials* **24**, 1181-1191 (2012).

183 Trassl, S., Motz, G., Rössler, E. & Ziegler, G. Characterization of the Free-Carbon Phase in Precursor-Derived Si-C-N Ceramics: I, Spectroscopic Methods. *Journal of the American Ceramic Society* **85**, 239-244 (2002).

184 Wang, Y., Wang, K., Zhang, L. & An, L. Structure and Optical Property of Polymer-Derived Amorphous Silicon Oxycarbides Obtained at Different Temperatures. *Journal of the American Ceramic Society* **94**, 3359-3363 (2011).

185 Jung, Y. *et al.* Metal seed layer thickness-induced transition from vertical to horizontal growth of MoS2 and WS2. *Nano letters* **14**, 6842-6849 (2014).

186 Choudhary, N. *et al.* Strain-Driven and Layer-Number-Dependent Crossover of Growth Mode in van der Waals Heterostructures: 2D/2D Layer-By-Layer Horizontal Epitaxy to 2D/3D Vertical Reorientation. *Advanced Materials Interfaces*, 1800382 (2018).

187 Islam, M. A. *et al.* Noble metal-coated MoS 2 nanofilms with vertically-aligned 2D layers for visible light-driven photocatalytic degradation of emerging water contaminants. *Scientific reports* **7**, 14944 (2017).

188 Plimpton, S. Fast Parallel Algorithms for Short-Range Molecular Dynamics. *Journal of Computational Physics* **117**, 1-19, (1995).

189 Humphrey, W., Dalke, A. & Schulten, K. VMD: Visual molecular dynamics. *Journal of Molecular Graphics* **14**, 33-38, (1996).

190 Barati Farimani, A. & Aluru, N. R. Spatial Diffusion of Water in Carbon Nanotubes: From Fickian to Ballistic Motion. *The Journal of Physical Chemistry B* **115**, 12145-12149, (2011).

191 Joung, I. S. & Cheatham, T. E. Determination of Alkali and Halide Monovalent Ion Parameters for Use in Explicitly Solvated Biomolecular Simulations. *The Journal of Physical Chemistry B* **112**, 9020-9041, (2008).

192 Jorgensen, W. L., Chandrasekhar, J., Madura, J. D., Impey, R. W. & Klein, M. L. Comparison of simple potential functions for simulating liquid water. *The Journal of Chemical Physics* **79**, 926-935, (1983).

193 Price, D. J. & III, C. L. B. A modified TIP3P water potential for simulation with Ewald summation. *The Journal of Chemical Physics* **121**, 10096-10103, (2004).

194 Darden, T., York, D. & Pedersen, L. Particle mesh Ewald: An N·log(N) method for Ewald sums in large systems. *The Journal of Chemical Physics* **98**, 10089-10092, (1993).

195 Choudhary, N. *et al.* Centimeter scale patterned growth of vertically stacked few layer only 2D MoS 2/WS 2 van der Waals heterostructure. *Scientific reports* **6**, 25456 (2016).

196 Okogbue, E. *et al.* Centimeter-Scale Periodically Corrugated Few-Layer 2D MoS2 with Tensile Stretch-Driven Tunable Multifunctionalities. *ACS applied materials & interfaces* **10**, 30623-30630 (2018).

197 Islam, M. A. *et al.* Three dimensionally-ordered 2D MoS 2 vertical layers integrated on flexible substrates with stretch-tunable functionality and improved sensing capability. *Nanoscale* **10**, 17525-17533 (2018).

198 Sotto, A. *et al.* Improved membrane structures for seawater desalination by studying the influence of sublayers. *Desalination* **287**, 317-325 (2012).

199 Wang, Z. *et al.* Understanding the aqueous stability and filtration capability of mos2 membranes. *Nano letters* **17**, 7289-7298 (2017).

200 Kim, J. H. *et al.* Centimeter-scale Green Integration of Layer-by-Layer 2D TMD vdW Heterostructures on Arbitrary Substrates by Water-Assisted Layer Transfer. *Scientific Reports* **9**, 1641, (2019).

201 Li, H. *et al.* From bulk to monolayer MoS2: evolution of Raman scattering. *Advanced Functional Materials* **22**, 1385-1390 (2012).

202 Luo, S. *et al.* Photoresponse properties of large-area MoS2 atomic layer synthesized by vapor phase deposition. *Journal of Applied Physics* **116**, 164304 (2014).

203 Graziano, G. On the size dependence of hydrophobic hydration. *Journal of the Chemical Society, Faraday Transactions* **94**, 3345-3352 (1998).

204 Li, H. *et al.* Fabrication of single-and multilayer MoS2 film-based field-effect transistors for sensing NO at room temperature. *small* **8**, 63-67 (2012).

205 Wieting, T. & Verble, J. Infrared and Raman Studies of Long-Wavelength Optical Phonons in Hexagonal Mo S 2. *Physical Review B* **3**, 4286 (1971).

206 Xie, J. *et al.* Defect-rich MoS2 ultrathin nanosheets with additional active edge sites for enhanced electrocatalytic hydrogen evolution. *Advanced materials* **25**, 5807-5813 (2013).

207 Ai, K., Ruan, C., Shen, M. & Lu, L. MoS2 nanosheets with widened interlayer spacing for high-efficiency removal of mercury in aquatic systems. *Advanced Functional Materials* **26**, 5542-5549 (2016).

208 Zou, H. *et al.* Synthesis and characterization of thin film composite reverse osmosis membranes via novel interfacial polymerization approach. *Separation and Purification Technology* **72**, 256-262 (2010).

209 Veerapaneni, S., Long, B., Freeman, S. & Bond, R. Reducing energy consumption for seawater desalination. *Journal-American Water Works Association* **99**, 95-106 (2007).

210 Riley, J. & Tongudai, M. The major cation/chlorinity ratios in sea water. *Chemical Geology* **2**, 263-269 (1967).

211 Millero, F. J., Feistel, R., Wright, D. G. & McDougall, T. J. The composition of Standard Seawater and the definition of the Reference-Composition Salinity Scale. *Deep Sea Research Part I: Oceanographic Research Papers* **55**, 50-72 (2008).

212 Li, L., Dong, J., Nenoff, T. M. & Lee, R. Desalination by reverse osmosis using MFI zeolite membranes. *Journal of membrane science* **243**, 401-404 (2004).

213 Pendergast, M. M. & Hoek, E. M. A review of water treatment membrane nanotechnologies. *Energy & Environmental Science* **4**, 1946-1971 (2011).

214 Safarpour, M., Vatanpour, V., Khataee, A. & Esmaeili, M. Development of a novel high flux and fouling-resistant thin film composite nanofiltration membrane by embedding reduced graphene oxide/TiO2. *Separation and Purification Technology* **154**, 96-107 (2015).

215 Yin, J., Zhu, G. & Deng, B. Graphene oxide (GO) enhanced polyamide (PA) thin-film nanocomposite (TFN) membrane for water purification. *Desalination* **379**, 93-101 (2016).

216 Zhao, H. *et al.* Improving the performance of polyamide reverse osmosis membrane by incorporation of modified multi-walled carbon nanotubes. *Journal of Membrane Science* **450**, 249-256 (2014).

217 Surwade, S. P. *et al.* Water desalination using nanoporous single-layer graphene. *Nature nanotechnology* **10**, 459 (2015).

218 Kazemi, A. S., Abdi, Y., Eslami, J. & Das, R. Support based novel single layer nanoporous graphene membrane for efficacious water desalination. *Desalination* **451**, 148-159 (2019).

219 Van Der Zande, A. M. *et al.* Grains and grain boundaries in highly crystalline monolayer molybdenum disulphide. *Nature materials* **12**, 554 (2013).

220 Hong, J. *et al.* Exploring atomic defects in molybdenum disulphide monolayers. *Nature communications* **6**, 6293 (2015).

221 Precner, M. *et al.* Evolution of metastable defects and its effect on the electronic properties of MoS2 films. *Scientific reports* **8** (2018).

222 Qiu, H. *et al.* Hopping transport through defect-induced localized states in molybdenum disulphide. *Nature communications* **4**, 2642 (2013).

223 Elibol, K. *et al.* Grain boundary-mediated nanopores in molybdenum disulfide grown by chemical vapor deposition. *Nanoscale* **9**, 1591-1598 (2017).

224 Wang, S. *et al.* Preferential Pt Nanocluster Seeding at Grain Boundary Dislocations in Polycrystalline Monolayer MoS2. *ACS nano* **12**, 5626-5636 (2018).

225 Kang, Y., Xia, Y., Wang, H. & Zhang, X. 2D Laminar Membranes for Selective Water and Ion Transport. *Advanced Functional Materials*, 1902014 (2019).

226 Deng, M., Kwac, K., Li, M., Jung, Y. & Park, H. G. Stability, molecular sieving, and ion diffusion selectivity of a lamellar membrane from two-dimensional molybdenum disulfide. *Nano letters* **17**, 2342-2348 (2017).

227 Liu, Y. *et al.* The preparation of a strawberry-like super-hydrophilic surface on the molybdenum substrate. *Colloids and Surfaces A: Physicochemical and Engineering Aspects* **404**, 52-55 (2012).

228 Trivedi, S. & Alameh, K. Effect of vertically aligned carbon nanotube density on the water flux and salt rejection in desalination membranes. *SpringerPlus* **5**, 1158 (2016).

229 Das, R., Ali, M. E., Hamid, S. B. A., Ramakrishna, S. & Chowdhury, Z. Z. Carbon nanotube membranes for water purification: a bright future in water desalination. *Desalination* **336**, 97-109 (2014).

230 Yang, Y. *et al.* Large-area graphene-nanomesh/carbon-nanotube hybrid membranes for ionic and molecular nanofiltration. *Science* **364**, 1057-1062 (2019).

231 Liu, G. *et al.* Ultrathin two-dimensional MXene membrane for pervaporation desalination. *Journal of membrane science* **548**, 548-558 (2018).

232 Li, X., Zhu, B. & Zhu, J. Graphene oxide based materials for desalination. *Carbon* (2019).

233 Lembke, D., Bertolazzi, S. & Kis, A. Single-layer MoS2 electronics. *Accounts of chemical research* **48**, 100-110 (2015).

234 Lukowski, M. A. *et al.* Enhanced hydrogen evolution catalysis from chemically exfoliated metallic MoS2 nanosheets. *Journal of the American Chemical Society* **135**, 10274-10277 (2013).

235 Kurapati, R., Kostarelos, K., Prato, M. & Bianco, A. Biomedical uses for 2D materials beyond graphene: current advances and challenges ahead. *Advanced Materials* **28**, 6052-6074 (2016).

236 Choudhary, N. *et al.* Two-dimensional transition metal dichalcogenide hybrid materials for energy applications. *Nano Today* **19**, 16-40 (2018).

237 Fang, A., Kroenlein, K. & Smolyanitsky, A. Mechanosensitive Ion Permeation across Subnanoporous MoS2 Monolayers. *The Journal of Physical Chemistry C* **123**, 3588-3593 (2019).

238 Li, H. *et al.* Experimental Realization of Few Layer 2D MoS2 Membranes of Near Atomic Thickness for High Efficiency Water Desalination. *Nano letters* (2019).

239 Baek, Y. *et al.* High performance and antifouling vertically aligned carbon nanotube membrane for water purification. *Journal of membrane Science* **460**, 171-177 (2014).

240 Ahn, C. H. *et al.* Carbon nanotube-based membranes: Fabrication and application to desalination. *Journal of Industrial and Engineering Chemistry* **18**, 1551-1559 (2012).

241 Du, F., Qu, L., Xia, Z., Feng, L. & Dai, L. Membranes of vertically aligned superlong carbon nanotubes. *Langmuir* **27**, 8437-8443 (2011).

242 Shi, Q. *et al.* Bilayer graphene with ripples for reverse osmosis desalination. *Carbon* **136**, 21-27 (2018).

243 Köhler, M. H. & Gavazzoni, C. Water Freezing in MoS2 Nanotubes. *The Journal of Physical Chemistry C* (2019).

244 Li, M. *et al.* Experimental study and modeling of atomic-scale friction in zigzag and armchair lattice orientations of MoS2. *Science and Technology of advanced MaTerialS* **17**, 189-199 (2016).

245 Li, X. & Zhu, H. Two-dimensional MoS2: Properties, preparation, and applications. *Journal of Materiomics* **1**, 33-44 (2015).

246 Holt, J. K. *et al.* Fast mass transport through sub-2-nanometer carbon nanotubes. *Science* **312**, 1034-1037 (2006).

247 Lee, K.-J. & Park, H.-D. The most densified vertically-aligned carbon nanotube membranes and their normalized water permeability and high pressure durability. *Journal of Membrane Science* **501**, 144-151 (2016).

248 Rumble, J. *CRC handbook of chemistry and physics*. (CRC press, 2017).

249 Hinds, B. J. *et al.* Aligned multiwalled carbon nanotube membranes. *Science* **303**, 62-65 (2004).

250 Yu, M., Funke, H. H., Falconer, J. L. & Noble, R. D. High density, vertically-aligned carbon nanotube membranes. *Nano Letters* **9**, 225-229 (2008).

251 Whitby, M. & Quirke, N. Fluid flow in carbon nanotubes and nanopipes. *Nature nanotechnology* **2**, 87 (2007).

252 Hummer, G., Rasaiah, J. C. & Noworyta, J. P. Water conduction through the hydrophobic channel of a carbon nanotube. *Nature* **414**, 188 (2001).

253 Corry, B. Designing carbon nanotube membranes for efficient water desalination. *The Journal of Physical Chemistry B* **112**, 1427-1434 (2008).

254 Corry, B. Water and ion transport through functionalised carbon nanotubes: implications for desalination technology. *Energy & Environmental Science* **4**, 751-759 (2011).

255 Esai Selvan, M., Keffer, D., Cui, S. & Paddison, S. Proton transport in water confined in carbon nanotubes: a reactive molecular dynamics study. *Molecular Simulation* **36**, 568-578 (2010).

256 Ali, S., Rehman, S. A. U., Luan, H.-Y., Farid, M. U. & Huang, H. Challenges and opportunities in functional carbon nanotubes for membrane-based water treatment and desalination. *Science of the Total Environment* **646**, 1126-1139 (2019).

257 Das, R. *et al.* Multifunctional carbon nanotubes in water treatment: the present, past and future. *Desalination* **354**, 160-179 (2014).

258 Fornasiero, F. *et al.* Ion exclusion by sub-2-nm carbon nanotube pores. *Proceedings of the National Academy of Sciences* **105**, 17250-17255 (2008).

259 Srivastava, A., Srivastava, O., Talapatra, S., Vajtai, R. & Ajayan, P. Carbon nanotube filters. *Nature materials* **3**, 610 (2004).

260 Zhang, L., Zhao, B., Jiang, C., Yang, J. & Zheng, G. Preparation and transport performances of high-density, aligned carbon nanotube membranes. *Nanoscale research letters* **10**, 266 (2015).